universität wien

MASTERARBEIT | MASTER'S THESIS

Titel | Title

Ab Initio Calculation of Polaron Properties Using Harmonic and Anharmonic Phonons

verfasst von | submitted by

Markus Schwarz BSc

angestrebter akademischer Grad | in partial fulfilment of the requirements for the degree of

Master of Science (MSc)

Wien | Vienna, 2025

Studienkennzahl lt. Studienblatt | Degree programme code as it appears on the student record sheet:	UA 066 876
Studienrichtung lt. Studienblatt | Degree programme as it appears on the student record sheet:	Masterstudium Physics
Betreut von | Supervisor:	Univ.-Prof. Dr.techn. Cesare Franchini

Kurzfassung

Polaronen sind Quasiteilchen, die bei physikalischen Phänomenen wie Thermoelektrizität und Photoemission sowie bei Materialeigenschaften wie elektrischer Leitfähigkeit und Oberflächenreaktivität eine zentrale Rolle spielen. Bis vor Kurzem erfolgte die dichtefunktionaltheorie-basierte Untersuchung der Polaronenbildung ausschließlich mithilfe von Superzellen. Diese Methode ist jedoch auf die Berechnung kleiner Polaronen beschränkt, da Berechnungen mit größeren Zellen, die die Bildung mittelgroßer oder großer Polaronen ermöglichen, aufgrund des hohen Rechenaufwands nicht praktikabel sind.

Die vorliegende Arbeit behandelt die Polaronenbildung im Rahmen einer kürzlich vorgestellten, dichtefunktionaltheorie-basierten *ab initio*-Theorie, die ausschließlich mit Eingangsparametern arbeitet, die in der Einheitszelle berechenbar sind. Diese Theorie erlaubt die Beschreibung sowohl kleiner als auch großer Polaronen. Im praktischen Teil der Arbeit wurden darauf basierende Berechnungen für Elektronen- und Lochpolaronen in LiF durchgeführt. In einem weiteren Schritt wurde für die Berechnung des Lochpolarons eine anharmonische Phononendispersion verwendet, die mithilfe der *self-consistent harmonic approximation*-Methode berechnet wurde.

Die Berechnungen zur Elektronen- und Lochpolaronenbildung unter Verwendung einer harmonischen Phononendispersion in LiF zeigen eine sehr gute Übereinstimmung mit den in der Literatur angegebenen Werten. Weiterführende Berechnungen mit einer anharmonischen Phononendispersion ergeben jedoch eine vergleichsweise erhöhte Polaronenbildungsenergie. Die Berücksichtigung anharmonischer Beiträge zur Phononendispersion macht die Lochpolaronenbildung in LiF daher energetisch ungünstiger.

Abstract

Polarons are quasiparticles that play a key role in various phenomena, such as charge transport, surface reactivity, thermoelectricity, and photoemission. Until recently, computational investigations of polaron formation based on density functional theory (DFT) were carried out by adding an excess charge to a supercell. This method is limited to small polarons, as medium-sized or large polarons cannot form in computationally tractable supercells.

This thesis investigates polaron formation within the framework of a recently developed *ab initio* theory of polarons, which relies solely on DFT calculations within the unit cell, rigorously describing both small and large polarons. On the basis of this approach, polaron formation calculations are carried out for electron and hole polarons in LiF. Additionally, further hole polaron calculations are performed, incorporating anharmonic phonons, calculated using the stochastic self-consistent harmonic approximation (SSCHA).

The results for electron and hole polarons in LiF, based on a harmonic phonon dispersion, are in very good agreement with values reported in the literature. Hole polaron calculations incorporating anharmonic phonons yield higher formation energies compared to values obtained from calculations with harmonic phonons. This indicates that hole polaron formation becomes energetically less favorable in LiF when anharmonicity is included.

Acknowledgements

I would like to sincerely thank Univ.-Prof. Dr. techn. Cesare Franchini for offering me the opportunity to work on this master's thesis and for suggesting such a challenging and engaging topic. The project demanded a steep learning curve but proved to be a rewarding experience that has significantly enhanced my understanding of both foundational principles and specialized methodologies.

My special thanks go to Luigi Ranalli, MSc, for his unwavering support throughout the project. He introduced me to essential specialized tools and concepts, and his guidance was vital in helping me navigate the complexities of the subject and stay on track.

I would also like to acknowledge the computational resources and tools that were crucial to my work. In particular, I am grateful for access to the Vienna Scientific Cluster and want to thank the developers of Quantum ESPRESSO, EPW, SSCHA, VESTA, Jmol, Blender, Atomic Blender, and Web3D.

Contents

List of Figures

List of Tables

List of Symbols

a_0	Bohr radius
$\mathbf{a}_1, \mathbf{a}_2, \mathbf{a}_3$	Basis vectors of a unit cell in a crystalline lattice
$C_{\kappa\alpha,\kappa'\alpha'}(\mathbf{R}_p)$	Translational invariant equilibrium-position interatomic force constants
$C_{\kappa\alpha,\kappa'\alpha'}(\mathbf{q})$	Interatomic force constants in reciprocal space
$D_{\kappa\alpha,\kappa'\alpha'}(\mathbf{R}_p)$	Translational invariant dynamical matrix
$D_{\kappa\alpha,\kappa'\alpha'}(\mathbf{q})$	Dynamical matrix in reciprocal space
$\mathbf{D}(\mathbf{r})$	Electric displacement field
d	Number of spacial dimensions
$E_0^{\mathrm{BO}}(\{\boldsymbol{\tau}_I\})$	Born-Oppenheimer potential in the electronic ground state
E_{F}	Fermi energy
ΔE_f	Polaron formation energy
$E_{\mathrm{xc}}[n]$	Exchange correlation energy functional
$\mathbf{E}(\mathbf{r})$	Electric field
e_e	Elementary charge
$\mathbf{e}_{\kappa\nu}(\mathbf{q})$	Polarization vector
$f_{n\mathbf{k}}$	Occupation number of Bloch state with band index n and wave-vector $\mathbf{k}$
$\mathbf{G}$	Generic reciprocal lattice vector
$g_{mn\nu}(\mathbf{k}, \mathbf{q})$	Electron-phonon matrix element
$\hat{H}$	Hamiltonian operator

$\hat{H}_{\mathrm{KS}}(\mathbf{r})$	Kohn-Sham Hamiltonian
$\hbar$	Reduced Planck constant
$\mathbf{k}$	Wave vector for electronic plane waves
M_I	I^{th} nucleus' mass
M	Number of nuclei in the whole system
M_{uc}	Number of nuclei in the crystallographic unit cell
m^*	Effective band mass
m_e	Electron mass
N	Number of electrons
N_p	Number of unit cells in the supercell
$n(\mathbf{r})$	Electron density
$\hat{n}_{\mathbf{q}\nu}, n_{\mathbf{q}\nu}$	Phononic number operator and occupation number
$\mathbf{q}$	Wave vector for plane-wave lattice vibrations
$\mathbf{R}$, $\mathbf{R}_p$	Generic lattice vector and lattice vector of unit cell p, respectively
$\mathbf{r}$, $\mathbf{r}_i$	Electron position, i^{th} electron's position
$\hat{T}_e$	Kinetic energy operator for electrons
$\hat{T}_n$	Kinetic energy operator for nuclei
$\mathbf{T}$	Supercell lattice vector
$U(\{\boldsymbol{\tau}_I\})$	Born-Oppenheimer potential in the electronic ground state
$U_{nm\mathbf{k}}$	Unitary Wannier gauge transformation
$u_{n\mathbf{k}}(\mathbf{r})$	Lattice periodic part of a Bloch function
$V_{\text{e-n}}(\mathbf{r}, \{\boldsymbol{\tau}_I\})$	Electrostatic potential exerted by all nuclei on an electron at position $\mathbf{r}$
$V_{\text{e-e}}(\{\mathbf{r}_i\})$	Potential energy from the electrostatic interaction between electrons
$V_{\text{n-n}}(\{\boldsymbol{\tau}_I\})$	Potential energy from the electrostatic interaction between nuclei

$V_{\mathrm{H}}(\mathbf{r})$	Hartree potential
$V_{\mathrm{xc}}(\mathbf{r})$	Exchange correlation potential
$V_{\mathrm{KS}}(\mathbf{r})$	Kohn-Sham potential
$V_{\mathrm{SCF}}(\mathbf{r})$	Self-consistent field potential
$w_{np}(\mathbf{r})$	Wannier function for band n at unit cell p
Z_I	I^{th} nucleus' atomic number
ϵ_0	Vacuum permittivity
ϵ^0	Static permittivity
ϵ^∞	High frequency permittivity
$\varepsilon_{n\mathbf{k}}$, $\varepsilon_n(\mathbf{k})$	Bloch eigenenergies, electronic band structure
$\varepsilon_{\mathrm{CBM}}$	Kohn-Sham eigenvalue of the conduction band minimum
$\rho(E)$	Electronic density of states
$\rho(\mathbf{r})$	Charge density
$\boldsymbol{\tau}_I$, $\boldsymbol{\tau}_{\kappa p}$	I^{th} nucleus position, position of nucleus κ in unit cell p
$\boldsymbol{\tau}^0_{\kappa p}$	Equilibrium position of nucleus κ in unit cell p
$\phi(\mathbf{r})$	Single electron orbital
$\varphi_i(\mathbf{r})$	Single electron Kohn-Sham orbital
$\Psi(\{\mathbf{r}_i\},\{\boldsymbol{\tau}_I\})$	Many-body wave function
$\psi(\{\mathbf{r}_i\})$	Wave function of the electronic system
$\psi(\mathbf{r})$	Polaron wave function
$\psi_{n\mathbf{k}}(\mathbf{r})$	Bloch wave function with band index n and wave-vector $\mathbf{k}$
$\psi^{\mathrm{w}}_{n\mathbf{k}}(\mathbf{r})$	Bloch function in Wannier gauge
Ω	Unit cell volume
$\omega_{\mathbf{q}\nu}$	Angular frequency of vibrational eigenmode $\mathbf{q}\nu$

Chapter 1

Introduction and Outline

In many-body physics, certain phenomena can be described by treating a particle and its interactions with surrounding particles as a single entity. Such entities are called quasiparticles, and they can serve as efficient approximations. They exhibit properties typically attributed to particles, such as a finite lifetime or an effective mass, which can be observed experimentally [1, pp. 1–11].

One phenomenon in solid-state physics that can be understood as a quasiparticle is an excess charge carrier—electron or hole—added to a polarizable material, along with the distortion and polarization it induces in the material's structure. The self-generated polarization cloud surrounds the excess charge, forming a potential well that localizes or traps it. The structural distortion then moves along with the charge carrier as it propagates through the material. The trapped excess charge, together with the structural distortion, constitutes the quasiparticle called a polaron [2].

Polarons have been experimentally confirmed in many different types of materials, including solids, liquids, polymers, and cold gases. Moreover, they have been found to play crucial roles in various phenomena, such as charge transport, surface reactivity, thermoelectricity, and photoemission. Polarons can be experimentally probed using methods like scanning tunneling microscopy (STM), scanning tunneling spectroscopy (STS), and angle-resolved photoemission spectroscopy (ARPES), among others [2].

The concept of a charge carrier self-trapping, or auto-localizing, via self-generated polarization was first introduced by Lev Landau in 1933 [3]. In 1946, Solomon Pekar developed a semi-classical model, now known as the Landau-Pekar model (LP model), describing an electron with an effective band mass, placed in a polarizable continuous dielectric medium [4]. In the 1950s, Herbert Fröhlich and Theodore Holstein established models for large and small polarons, respectively [5, 6, 7, 8]. Their formulations, expressed as Hamiltonians for a quantum field theoretical treatment, laid the foundation for ongoing theoretical and numerical investigations of the polaron problem. These Hamiltonians characteristically include electron-phonon interaction contributions, which has led to the

interpretation of polarons as electrons or holes dressed by virtual phonons. Since the 1990s, various computational approaches were developed to calculate polaron properties, such as polaron formation energy, polaron dispersion, polaron effective mass, polaron mobility, and polaron wave function [2].

However, the Fröhlich Hamiltonian accounts only for effectively dispersionless longitudinal optical (LO) phonon contributions and is defined in the limit of long-range electron-phonon interactions. This means it exclusively describes large polarons, with radii much larger than the lattice parameter. In contrast, the Holstein Hamiltonian exclusively considers short-range electron-phonon interactions, limiting it to small polarons with radii on the order of the lattice parameter [2, 9]. For investigating polaron formation in many materials of practical interest, which often depends on contributions from both long- and short-range electron-phonon interactions, neither description is sufficient on its own. Although the Hamiltonians of these models were modified and extended to account for more diverse electron-phonon interactions, a unified method for incorporating all regimes of the electron-phonon interaction, using parameters obtained solely from *ab initio* calculations, had been missing until recently [9].

In 2019, W. H. Sio and colleagues published Refs. [9] and [10], which introduced a formulation of the polaron problem within density functional theory (DFT). This approach is characterized by the avoidance of expensive and poorly scalable supercell calculations, as all required quantities—electronic band structure, phonon dispersion, and electron-phonon matrix elements—can be obtained from calculations within the unit cell. Furthermore, this model retains a close relationship to the LP model while overcoming its limitations. This *ab initio* theory of polarons is implemented in the EPW code [11, 12]. Together with the well-established Quantum ESPRESSO (QE) [13] and Wannier90 [14] codes, it forms a computational workflow for *ab initio* polaron formation calculations in the crystal unit cell [2, 9, 10].

The objectives of this thesis are to introduce the concept of self-trapping of an excess charge carrier in the historical LP model, to explain the derivation of the *ab initio* theory of polarons, and to present results from various polaron formation calculations for lithium fluoride (LiF), performed during this thesis project. To achieve this, the thesis covers essential concepts from solid-state physics and corresponding computational methods, both of which are crucial for understanding the *ab initio* polaron theory and the associated computational workflow. The EPW calculations will aim to reproduce the electron and hole polaron formation results for LiF, presented in Refs. [9, 10]. Additionally, this thesis introduces an enhancement of the hole polaron calculation by incorporating anharmonic phonons, obtained from the self-consistent harmonic approximation (SSCHA) method,

implemented in the SSCHA code [15]. The goal of this addition will be to investigate the impact of anharmonic contributions in the phonon dispersion on hole polaron formation. To support this, the basic theory behind SSCHA is also discussed.

1.1. Outline

- Chapter 2 presents the semi-classical LP model and highlights its shortcomings, thereby motivating alternative theoretical approaches. The LP model introduces the key aspect of the polaron quasiparticle by describing the self-trapping of an excess charge carrier in a continuous, polarizable medium.
- Chapter 3 introduces fundamental concepts of solid-state physics within the Born-Oppenheimer (BO) approximation. It focuses on well-established theoretical frameworks for electronic structure and lattice vibrations in crystalline materials. Specifically, this chapter provides an understanding of Bloch's theorem, Wannier functions, and phonons. It concludes with the derivation of electron-phonon interactions, culminating to a Hamiltonian for an electron-phonon system with first-order electron-phonon couplings.
- Chapter 4 builds upon the electronic structure concepts presented in Chapter 3 and introduces density functional theory. It begins with the Hohenberg-Kohn theorem and progresses to the Kohn-Sham equations. Based on the solutions to these equations, this chapter proceeds with an explanation of the Hellmann-Feynman theorem for obtaining interatomic forces and density functional perturbation theory (DFPT) for calculating phonon dispersions without the use of supercells.
- Chapter 5 derives the DFT-based *ab initio* polaron model proposed by Sio et al. in Ref. [9].
- Chapter 6 discusses the SSCHA, a method for incorporating anharmonic contributions into the dynamical matrix of lattice vibrations. The SSCHA is based on free energy minimization with respect to a harmonic trial Hamiltonian and relies on the Gibbs-Bogoliubov inequality while performing a free energy gradient descent. The trial Hamiltonian is parameterized by the nuclei's centroid positions and the auxiliary force constants matrix.
- Chapter 7 provides details on methods for solving the Kohn-Sham equations and introduces the concepts of Fourier and Wannier interpolation. Understanding these methods is essential for following the computational workflow used for polaron

formation calculations on fine grids in reciprocal space, as described in the subsequent chapter.

- Chapter 8 offers an in-depth description of the computational setup and workflow used to obtain electron and hole polaron formation energies in LiF. The described steps include preparatory calculations, such as structural relaxation, band structure, and phonon dispersion calculations, as well as more specific calculations like SSCHA minimization, the Wannierization procedure, and finally the polaron formation calculation.

- Chapter 9 presents and discusses interim and final results, along with convergence tests, utilizing various visualization methods. The results are then compared to those from Refs. [9, 10].

Chapter 2

The Landau-Pekar Model

The LP model is a semi-classical model that describes an electron added to a polar insulator. In this model, the electron is described by a wave function $\psi(\mathbf{r})$ and an effective mass m^*, accounting for interactions with the valence manifold, as explained in Subsection 3.2.2. Simultaneously, the dielectric medium, defined by the static and high-frequency permittivities ϵ^0 and ϵ^∞, respectively, is assumed to be continuous and responds to the electron's free charge density according to classical electrostatics. The total energy *Ansatz*

$$E_{\mathrm{LP}} = \frac{\hbar^2}{2m^*} \int d\mathbf{r}\, |\boldsymbol{\nabla}\psi(\mathbf{r})|^2 + \frac{1}{2} \int d\mathbf{r}\, \mathbf{E}(\mathbf{r}) \cdot \mathbf{D}(\mathbf{r}) \tag{2.1}$$

is therefore composed of the electron's kinetic energy, and the classical electrostatic energy in a dielectric medium [9].

The displacement field $\mathbf{D}(\mathbf{r})$ must satisfy Gauss's law:

$$\boldsymbol{\nabla} \cdot \mathbf{D}(\mathbf{r}) = \underbrace{-e_e\, |\psi(\mathbf{r})|^2}_{\rho(\mathbf{r})}, \tag{2.2}$$

where the free charge density $\rho(\mathbf{r})$ is derived from the probability density $|\psi(\mathbf{r})|^2$ [9]. Using the relation

$$\mathbf{D}(\mathbf{r}) = -\boldsymbol{\nabla}\Phi(\mathbf{r}), \tag{2.3}$$

Eq. (2.2) can be rewritten as Poisson's equation and can be solved for the electrostatic potential:

$$\Phi(\mathbf{r}) = -\frac{e_e}{4\pi} \int d\mathbf{r}'\, \frac{|\psi(\mathbf{r}')|^2}{|\mathbf{r} - \mathbf{r}'|}. \tag{2.4}$$

The displacement field then follows from Eqs. (2.4) and (2.3). It can be substituted into the electrostatic term of Eq. (2.1) for $\mathbf{D}(\mathbf{r})$ and $\mathbf{E}(\mathbf{r})$, using $\mathbf{E}(\mathbf{r}) = \mathbf{D}(\mathbf{r})/(\epsilon_0\epsilon^0)$ [9]. Finally, after applying integration by parts and using the identity $\boldsymbol{\nabla}^2|\mathbf{r}|^{-1} = -4\pi\delta^3(\mathbf{r})$, one arrives at

$$\frac{1}{2} \int d\mathbf{r}\, \mathbf{E}(\mathbf{r}) \cdot \mathbf{D}(\mathbf{r}) = \frac{1}{2} \frac{e_e^2}{4\pi\epsilon_0\epsilon^0} \iint d\mathbf{r} d\mathbf{r}'\, \frac{|\psi(\mathbf{r})|^2 |\psi(\mathbf{r}')|^2}{|\mathbf{r} - \mathbf{r}'|}, \tag{2.5}$$

expressing the electrostatic energy in terms of the electron's wave function [16, pp. 12–15] [9]. Since the electronic screening is already incorporated into the effective mass m^*, the contribution from the high-frequency permittivity, obtained by substituting ϵ^∞ for ϵ^0 in (2.5), must be subtracted from the electrostatic energy contribution [9]. The energy functional for the LP model is then given by

$$E_{\mathrm{LP}}\left[\psi(\mathbf{r})\right] = \frac{\hbar^2}{2m^*}\int d\mathbf{r}\,|\boldsymbol{\nabla}\psi(\mathbf{r})|^2 - \frac{1}{2}\frac{e_e^2}{4\pi\epsilon_0}\underbrace{\left(\frac{1}{\epsilon^\infty}-\frac{1}{\epsilon^0}\right)}_{\kappa^{-1}}\iint d\mathbf{r}d\mathbf{r}'\,\frac{|\psi(\mathbf{r})|^2|\psi(\mathbf{r}')|^2}{|\mathbf{r}-\mathbf{r}'|}, \quad (2.6)$$

as stated in Ref. [9]. The normalization condition for the wave function enters via the Lagrange multiplier ε, yielding the modified functional

$$\begin{aligned} E'_{\mathrm{LP}}\left[\psi(\mathbf{r})\right] = \frac{\hbar^2}{2m^*}&\int d\mathbf{r}\,|\boldsymbol{\nabla}\psi(\mathbf{r})|^2 \\ &- \frac{1}{2}\frac{e_e^2}{4\pi\epsilon_0}\frac{1}{\kappa}\iint d\mathbf{r}d\mathbf{r}'\,\frac{|\psi(\mathbf{r})|^2|\psi(\mathbf{r}')|^2}{|\mathbf{r}-\mathbf{r}'|} \\ &- \varepsilon\left(\int d\mathbf{r}\,|\psi(\mathbf{r})|^2 - 1\right). \end{aligned} \quad (2.7)$$

To find the ground-state wave function and the corresponding ground-state energy, $E'_{\mathrm{LP}}\left[\psi(\mathbf{r})\right]$ is minimized with respect to $\psi^*(\mathbf{r})$ and ε, by imposing the conditions

$$\frac{\delta E'_{\mathrm{LP}}\left[\psi(\mathbf{r})\right]}{\delta\psi^*(\mathbf{r})} = 0 \quad (2.8)$$

and

$$\frac{\partial E'_{\mathrm{LP}}\left[\psi(\mathbf{r})\right]}{\partial\varepsilon} = 0. \quad (2.9)$$

This yields the eigenvalue problem

$$\left[-\frac{\hbar^2}{2m^*}\boldsymbol{\nabla}^2 - \frac{e_e^2}{4\pi\epsilon_0}\frac{1}{\kappa}\int d\mathbf{r}'\,\frac{|\psi(\mathbf{r}')|^2}{|\mathbf{r}-\mathbf{r}'|}\right]\psi(\mathbf{r}) = \varepsilon\,\psi(\mathbf{r}) \quad (2.10)$$

for a normalized wave function $\psi(\mathbf{r})$ with eigenvalue ε [9]. The ground-state energy can also be expressed as

$$E_{\mathrm{LP}} = \varepsilon + \frac{1}{2}\frac{e_e^2}{4\pi\epsilon_0}\frac{1}{\kappa}\iint d\mathbf{r}d\mathbf{r}'\,\frac{|\psi(\mathbf{r})|^2|\psi(\mathbf{r}')|^2}{|\mathbf{r}-\mathbf{r}'|}, \quad (2.11)$$

explicitly involving the eigenvalue ε [9].

2.1. The Formation of a Polaron

In Ref. [9], the self-trapping mechanism in the LP model is demonstrated by choosing a normalized trial wave function of the form

$$\psi(\mathbf{r}) = \left(\pi r_p^3\right)^{-1/2} e^{-|\mathbf{r}|/r_p}. \tag{2.12}$$

Substituting this *Ansatz* into the energy functional of Eq. (2.6) yields the energy expression

$$E_{\mathrm{LP}}(r_p) = \underbrace{\frac{\hbar^2}{2m^* r_p^2}}_{P(r_p)} - \underbrace{\frac{5}{16}\frac{1}{\kappa}\frac{e_e^2}{4\pi\epsilon_0 r_p}}_{Q(r_p)}, \tag{2.13}$$

which depends only on the polaron size r_p. The form of Eq. (2.13) reveals two competing energy contributions, schematically visualized in Fig. 2.1. The first term, representing the kinetic energy, yields lower energies for larger polaron sizes r_p, thus promoting a delocalized wave function. In contrast, the second term in $E_{\mathrm{LP}}(r_p)$, which represents the electrostatic contribution, is negative—for a positive κ—and lowers the energy for smaller r_p, thereby allowing localized polarons in LP model [9]. Determining the actual polaron size for this particular trial function then requires the minimization of $E_{\mathrm{LP}}(r_p)$ with respect to r_p, yielding

$$r_{p,\min} = \frac{16}{5}\frac{\kappa}{m^*/m_e}\, a_0, \tag{2.14}$$

according to Ref. [9].

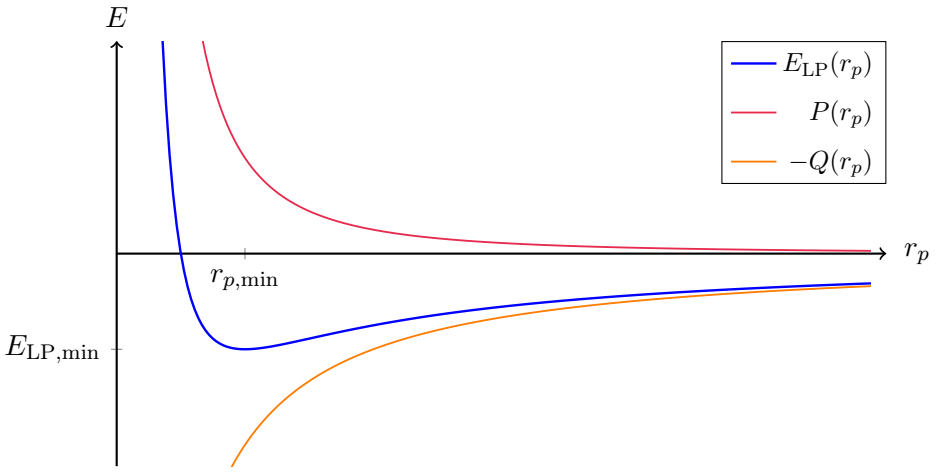

Fig. 2.1.: Schematic illustration of the competing positive and negative contributions $P(r_p)$ and $-Q(r_p)$ in red and amber, respectively, which sum to $E_{\mathrm{LP}}(r_p)$ in blue.

2.2. Limitations of the Landau-Pekar Model

According to Eq. (2.13), the formation of a polaron is only possible for positive κ. This occurs exclusively in polar crystals, where $\epsilon^0 > \epsilon^\infty$. Therefore, the LP model is not suitable for describing polarons in other types of materials, such as nonpolar semiconductors [9]. However, the most significant problem of the LP model is a discrepancy between its initial assumption of a continuous medium and its prediction: Modeling materials as continua assumes polaron sizes on a scale where the atomistic nature of materials can be disregarded. However, the LP model predicts small polarons, which contradicts this initial assumption [9].

Chapter 3

Many-Body Problem in Solid-State Physics

Conceptualizing a solid material as a quantum-mechanical many-body system serves as the starting point for understanding material properties and phenomena from first principles. In many-body theory, a system composed of M atomic nuclei and N electrons is fully described by a wave function $\Psi(\{\mathbf{r}_i\},\{\boldsymbol{\tau}_I\}) = \Psi(\mathbf{r}_1,\cdots,\mathbf{r}_N,\boldsymbol{\tau}_1,\cdots,\boldsymbol{\tau}_M)$. Its parameters represent the positions of electrons, $\mathbf{r}_i$, and atomic nuclei, $\boldsymbol{\tau}_I$, in real space [17, pp. 19–23]. For a time-independent description of such a system, the wave function must satisfy the stationary Schrödinger equation

$$\hat{H}\Psi(\{\mathbf{r}_i\},\{\boldsymbol{\tau}_I\}) = E_{\text{tot}}\,\Psi(\{\mathbf{r}_i\},\{\boldsymbol{\tau}_I\}), \tag{3.1}$$

where E_{tot} is the total energy, and $\hat{H}$ is the Hamiltonian of the system. The probability density for finding the system in a specific configuration $(\{\mathbf{r}_i\},\{\boldsymbol{\tau}_I\})$ is given by $|\Psi(\{\mathbf{r}_i\},\{\boldsymbol{\tau}_I\})|^2$, according to the Born rule. This leads to the normalization condition

$$\int |\Psi(\{\mathbf{r}_i\},\{\boldsymbol{\tau}_I\})|^2\, d\mathbf{r}_1\cdots d\mathbf{r}_N\, d\boldsymbol{\tau}_1\cdots d\boldsymbol{\tau}_M = 1, \tag{3.2}$$

since the system must be found in one of the possible configurations [17, pp. 19–23].

The Hamiltonian operator $\hat{H}$ encodes the system's energy contributions in terms of kinetic and interaction energies. In solid-state physics, the particles' interactions are caused by the electrostatic charges of the electrons and the nuclei. These enter in the form of Coulomb potentials, acting between all possible pairs of particles. Therefore, the full Hamiltonian takes the form

$$\begin{aligned}\hat{H} = &-\sum_i \frac{\hbar^2}{2m_e}\boldsymbol{\nabla}_i^2 - \sum_I \frac{\hbar^2}{2M_I}\boldsymbol{\nabla}_I^2 \\ &+ \frac{e_e^2}{4\pi\epsilon_0}\left[-\sum_{i,I}\frac{Z_I}{|\mathbf{r}_i-\boldsymbol{\tau}_I|} + \sum_{i<j}\frac{1}{|\mathbf{r}_i-\mathbf{r}_j|} + \sum_{I<J}\frac{Z_I Z_J}{|\boldsymbol{\tau}_I-\boldsymbol{\tau}_J|}\right],\end{aligned} \tag{3.3}$$

with M_I being the mass of nucleus I, and Z_I is its atomic number. Summations over the lowercase indices of electronic position operators run from 1 to N, and uppercase indices of the nuclei's position operators run from 1 to M [17, pp. 19–23].

Determining the ground state of $\hat{H}$ is crucial for the calculation of equilibrium properties of materials, such as elastic properties, thermal properties, or phase diagrams. However, using a direct numerical method, e.g., discretizing Eq. (3.1) in real space, becomes computationally intractable even for small systems, as the computational effort scales exponentially with the system size. Therefore, developing and applying approximation methods is crucial to carry out *ab initio* calculations [17, pp. 19–23].

3.1. Born-Oppenheimer Approximation

When using Hartree atomic units, which measure mass, distance, charge, and energy in units of m_e, a_0, e_e, and the Hartree energy,

$$E_{\mathrm{Ha}} = \frac{e_e^2}{4\pi\epsilon_0 a_0}, \tag{3.4}$$

respectively, Eq. (3.3) becomes

$$\hat{H} = \underbrace{-\sum_i \frac{\boldsymbol{\nabla}_i^2}{2}}_{\hat{T}_{\mathrm{e}}} \underbrace{-\sum_I \frac{1}{M_I}\frac{\boldsymbol{\nabla}_I^2}{2}}_{\hat{T}_{\mathrm{n}}} + \sum_i \underbrace{\sum_I -\frac{Z_I}{|\mathbf{r}_i - \boldsymbol{\tau}_I|}}_{V_{\text{e-n}}(\mathbf{r}_i,\{\boldsymbol{\tau}_I\})} + \underbrace{\sum_{i<j} \frac{1}{|\mathbf{r}_i - \mathbf{r}_j|}}_{V_{\text{e-e}}(\{\mathbf{r}_i\})} + \underbrace{\sum_{I<J} \frac{Z_I Z_J}{|\boldsymbol{\tau}_I - \boldsymbol{\tau}_J|}}_{V_{\text{n-n}}(\{\boldsymbol{\tau}_I\})}. \tag{3.5}$$

This form of $\hat{H}$ is more convenient to work with, as it emphasizes that the atomic numbers Z_I and the masses M_I are the defining parameters of the system [17, pp. 23–25] [18, pp. 17–18]. The factors $1/M_I$ in the nuclei's kinetic energy term $\hat{T}_{\mathrm{n}}$ lie between the orders of 10^{-5} and 10^{-4}, suggesting that $\hat{T}_{\mathrm{n}}$ can be treated as a perturbation, such that

$$\hat{H} = \hat{H}_0 + \hat{T}_{\mathrm{n}}. \tag{3.6}$$

Consequently, the Schrödinger equation for $\hat{H}_0$ alone is a differential equation with respect to the electronic position operators $\mathbf{r}_i$ only, and the nuclei's coordinates $\boldsymbol{\tau}_I$ enter solely as external parameters to $V_{\text{e-n}}(\mathbf{r};\{\boldsymbol{\tau}_I\})$ [18, pp. 27–28].

The solutions to the electronic Schrödinger equation,

$$\hat{H}_0\,\psi_\alpha(\{\mathbf{r}_i\};\{\boldsymbol{\tau}_I\}) = E_\alpha^{\mathrm{BO}}(\{\boldsymbol{\tau}_I\})\,\psi_\alpha(\{\mathbf{r}_i\};\{\boldsymbol{\tau}_I\}), \tag{3.7}$$

form a complete set of eigenfunctions $\psi_\alpha(\{\mathbf{r}_i\};\{\boldsymbol{\tau}_I\})$ and corresponding eigenenergies $E_\alpha^{\mathrm{BO}}(\{\boldsymbol{\tau}_I\})$. This implies that, for any clamped nuclear configuration $\boldsymbol{\tau}_I$, the many-body

wave function can be expressed as the linear combination:

$$\Psi(\{\mathbf{r}_i\},\{\boldsymbol{\tau}_I\}) = \sum_{\alpha} \chi_\alpha(\{\boldsymbol{\tau}_I\})\, \psi_\alpha(\{\mathbf{r}_i\};\{\boldsymbol{\tau}_I\}), \tag{3.8}$$

where $\chi_\alpha(\{\boldsymbol{\tau}_I\})$ are expansion coefficients [18, pp. 27–28]. This expression is substituted back into the full many-body Schrödinger equation, Eq. (3.1). Calculating the overlap integral with $\psi^*_\beta(\{\mathbf{r}_i\};\{\boldsymbol{\tau}_I\})$ shows that the transition matrix elements between electronic quantum numbers α and β can be neglected, as they are estimated to be a factor of $(1/M_I)^{\frac{1}{4}} \sim 10^{-1}$ to 10^{-2} smaller than the characteristic kinetic energies of the nuclei. Thus, one arrives at the nuclear Schrödinger equations

$$\left[\hat{T}_\mathrm{n} + E^\mathrm{BO}_\beta(\{\boldsymbol{\tau}_I\})\right]\, \chi_\beta(\{\boldsymbol{\tau}_I\}) = E_\mathrm{tot}\, \chi_\beta(\{\boldsymbol{\tau}_I\}), \tag{3.9}$$

for the nuclei's wave functions $\chi_\beta(\{\boldsymbol{\tau}_I\})$, which were initially introduced as expansion coefficients in Eq. (3.8). The effective potentials in Eqs. (3.9) are the eigenvalues of $\hat{H}_0$, given by

$$E^\mathrm{BO}_\beta(\{\boldsymbol{\tau}_I\}) = E^\mathrm{el}_\beta(\{\boldsymbol{\tau}_I\}) + V_\mathrm{n\text{-}n}(\{\boldsymbol{\tau}_I\}), \tag{3.10}$$

and consisting of an electronic part, and the electrostatic potential between the nuclei [18, pp. 27–28]. The quantity $E^\mathrm{BO}_\beta(\{\boldsymbol{\tau}_I\})$ is commonly referred to as the BO energy surface or as the BO potential [19]. For convenience, the BO potential associated with the electronic ground state will be denoted as

$$U(\{\boldsymbol{\tau}_I\}) \equiv E^\mathrm{BO}_0(\{\boldsymbol{\tau}_I\}). \tag{3.11}$$

The physical picture justifying the approach of separating the electronic and nuclear wave functions is the notion of the electronic system adiabatically following the nuclei's movements. This idealization assumes that the electrons are always found in an equilibrium state, corresponding to the instantaneous positions of the nuclei. The strategy for solving the whole system is to first obtain the eigenenergies for the electronic system, which then serve as the effective potential for the nuclei. As noted, the full separation of electron and nuclear wave functions neglects transition matrix elements of order 10^{-1} to 10^{-2}, which can still play a significant role. Nevertheless, a perturbative treatment is justified by the presence of such a small parameter and will be carried out in the context of the electron-phonon interaction in Section 3.4 [18, pp. 25–31].

3.2. Electronic Structure

The adiabatic approximation already simplifies the many-body problem considerably and allows a separate treatment of the electronic and nuclear parts of a system. Still, the

computational effort for solving Eqs. (3.7) and (3.9) scales exponentially with the number of involved particles. This is especially relevant for the electronic Schrödinger equation, Eq. (3.7), since electrons are treated quantum mechanically in *ab initio* calculations. In order to find electronic ground-state properties in an external potential $V_{\text{e-n}}(\mathbf{r};\{\boldsymbol{\tau}_I\})$, additional approximation methods were developed [17, pp. 22–25].

3.2.1. Independent Electron and Mean-Field Approximations

Since the focus will be on finding the electronic ground state of Eq. (3.7), for a clamped nuclear configuration $\boldsymbol{\tau}_I$, the corresponding electronic wave function will be denoted as $\psi(\{\mathbf{r}_i\}) \equiv \psi(\{\mathbf{r}_i\};\{\boldsymbol{\tau}_I\})$ for convenience. Furthermore, the fixed configuration $\boldsymbol{\tau}_I$ renders $V_{\text{n-n}}(\{\boldsymbol{\tau}_I\})$ a constant. Therefore, this term can be removed from further considerations by defining $E \equiv E_{\text{tot}} - V_{\text{n-n}}(\{\boldsymbol{\tau}_I\})$ and rewriting the problem as

$$\left[-\sum_i \frac{\boldsymbol{\nabla}_i^2}{2} + \sum_i V_{\text{e-n}}(\mathbf{r}_i;\{\boldsymbol{\tau}_I\}) + V_{\text{e-e}}(\{\mathbf{r}_i\})\right]\psi(\{\mathbf{r}_i\}) = E\,\psi(\{\mathbf{r}_i\}). \tag{3.12}$$

In this electronic Schrödinger equation, the term $V_{\text{e-n}}(\mathbf{r};\{\boldsymbol{\tau}_I\})$ is often referred to as the external potential, since the nuclei's positions enter as external parameters [17, pp. 25–28]. Eq. (3.12) can be compacted to

$$\left[\hat{H}_0 + V_{\text{e-e}}(\{\mathbf{r}_i\})\right]\psi(\{\mathbf{r}_i\}) = E\,\psi(\{\mathbf{r}_i\}), \tag{3.13}$$

with

$$\hat{H}_0 = \sum_i \hat{h}(\mathbf{r}_i), \tag{3.14}$$

and

$$\hat{h}(\mathbf{r}_i) \equiv \frac{\boldsymbol{\nabla}_i^2}{2} + V_{\text{e-n}}(\mathbf{r}_i;\{\boldsymbol{\tau}_I\}). \tag{3.15}$$

The strategy to approximate the ground state of Eq. (3.13) starts with the drastically simplified *Ansatz* of a product wave function

$$\psi(\{\mathbf{r}_i\}) = \prod_i \phi_i(\mathbf{r}_i), \tag{3.16}$$

neglecting the electron-electron interaction $V_{\text{e-e}}(\{\mathbf{r}_i\})$ in Eq. (3.13) [17, pp. 25–28]. These considerations simplify Eq. (3.13) to

$$\left[\sum_j \hat{h}(\mathbf{r}_j)\right]\prod_i \phi_i(\mathbf{r}_i) = E\prod_i \phi_i(\mathbf{r}_i), \tag{3.17}$$

which further decouples to

$$\hat{h}(\mathbf{r})\,\phi_i(\mathbf{r}) = \left[-\frac{\boldsymbol{\nabla}^2}{2} + V_{\text{e-n}}(\mathbf{r};\{\boldsymbol{\tau}_I\})\right]\,\phi_i(\mathbf{r}) = \varepsilon_i\,\phi_i(\mathbf{r}), \tag{3.18}$$

and is referred to as the independent electrons approximation [17, pp. 25–28]. The many-body character of the former system can be partially recovered by considering Pauli's exclusion principle, which forbids all electrons from occupying $\phi_0(\mathbf{r})$, the orbital with the lowest eigenenergy ε_0 [18, pp. 136–137]. Instead, each orbital $\phi_i(\mathbf{r})$ can hold a maximum of two electrons which must occupy mutually orthogonal spin states. Any possible ground-state wave function, constructed from the solutions of Eq. (3.18), is therefore characterized by an orbital occupancy $\{f_i\}$, where $f_i \in \{0, 1, 2\}$, that minimizes

$$E(\{f_i\}) = \sum_i f_i\,\varepsilon_i, \tag{3.19}$$

as described in Ref. [17, pp. 27–28].

As a side note, a more thorough way to account for the Pauli exclusion principle is to construct the wave function as a Slater determinant of spin orbitals, instead of the simple product *Ansatz* given in Eq. (3.16). Applying the variational principle by minimizing the expectation value of the Hamiltonian in Eq. (3.13) with respect to electron orbitals yields the Hartree-Fock equations, which introduce the exchange potential $V_{\text{x}}(\mathbf{r}, \mathbf{r}')$ [17, pp. 239–242]. However, the Hartree-Fock method will not be discussed further, as it is not required for discussing density functional theory.

A first step in approximating $V_{\text{e-e}}(\{\mathbf{r}_i\})$ is to introduce the so-called Hartree potential $V_{\text{H}}(\mathbf{r})$. It is a mean-field potential, based on the electron density

$$n(\mathbf{r}) = n^{\uparrow}(\mathbf{r}) + n^{\downarrow}(\mathbf{r}) = 2\sum_i^{N/2} |\phi_i(\mathbf{r})|^2, \tag{3.20}$$

and assumes spin-degeneracy of the occupied orbitals [17, pp. 30–31] [9, p. 4]. Furthermore, $n(\mathbf{r})$ takes the role of the charge density in the Hartree potential's Poisson equation

$$\boldsymbol{\nabla}^2 V_{\text{H}}(\mathbf{r}) = -4\pi n(\mathbf{r}). \tag{3.21}$$

Solving this Poisson equation yields

$$V_{\text{H}}(\mathbf{r}) = \int d\mathbf{r}'\,\frac{n(\mathbf{r}')}{|\mathbf{r} - \mathbf{r}'|}, \tag{3.22}$$

leading to the single-electron equations

$$\left[-\frac{\boldsymbol{\nabla}^2}{2} + \underbrace{V_{\text{e-n}}(\mathbf{r};\{\boldsymbol{\tau}_I\}) + V_{\text{H}}(\mathbf{r})}_{V_{\text{eff}}(\mathbf{r};\{\boldsymbol{\tau}_I\})}\right]\,\phi_i(\mathbf{r}) = \varepsilon_i\,\phi_i(\mathbf{r}). \tag{3.23}$$

This mean-field approximation establishes the concept of self-consistent equations, as $V_{\mathrm{H}}(\mathbf{r})$ is a functional of $n(\mathbf{r})$, which in turn depends on the solutions of Eqs. (3.23) [17, pp. 30–31].

The potentials $V_{\text{e-n}}(\mathbf{r}; \{\boldsymbol{\tau}_I\})$ and $V_{\mathrm{H}}(\mathbf{r})$ combine to form the effective potential $V_{\text{eff}}(\mathbf{r}; \{\boldsymbol{\tau}_I\})$, which acts on the single-electron wave functions. The effective potential obtained from the electronic ground-state density, which thereby satisfies Eq. (3.23) self-consistently, is referred to as the self-consistent-field potential $V_{\mathrm{SCF}}(\mathbf{r}; \{\boldsymbol{\tau}_I\})$ [19].

It should be noted that the concepts presented in the following sections are agnostic to the specific form of the self-consistent equations associated with $V_{\mathrm{SCF}}(\mathbf{r}; \{\boldsymbol{\tau}_I\})$. This is noteworthy because these they will be applied to the self-consistent-field potential obtained from the Kohn-Sham equations, as explained in Chapter 4.

3.2.2. Bloch's Theorem

Previous sections did not assume any specific arrangement of the nuclei's configuration $\boldsymbol{\tau}_I$. Therefore, $V_{\text{e-n}}(\mathbf{r}; \{\boldsymbol{\tau}_I\})$ and, subsequently, $V_{\mathrm{SCF}}(\mathbf{r}; \{\boldsymbol{\tau}_I\})$ were considered to be arbitrary in their spatial structure. However, neglecting crystallographic defects, crystalline solids can be idealized as following a strict periodic structure. This means that a crystallographic basis of nuclei is periodically repeated according to a Bravais lattice, with lattice vectors $\mathbf{R} = n_1\mathbf{a}_1 + n_2\mathbf{a}_2 + n_3\mathbf{a}_3$, where $n_1, n_2, n_3 \in \mathbb{Z}$ [20, pp. 317–321]. The lattice periodicity reflects in a translational invariance of the potential,

$$V_{\mathrm{SCF}}(\mathbf{r}) = V_{\mathrm{SCF}}(\mathbf{r} + \mathbf{R}), \tag{3.24}$$

which can therefore be expanded as a Fourier series:

$$V_{\mathrm{SCF}}(\mathbf{r}) = \sum_{\mathbf{G}} V_{\mathrm{SCF}}(\mathbf{G})\, e^{i\mathbf{G}\cdot\mathbf{r}}. \tag{3.25}$$

Combining Eqs. (3.24) and (3.25) shows that $\mathbf{G} \cdot \mathbf{R} = 2\pi m$ with $m \in \mathbb{Z}$, such that $\mathbf{G}$ can be identified as the set of reciprocal lattice vectors $\mathbf{G} = h\mathbf{b}_1 + k\mathbf{b}_2 + l\mathbf{b}_3$, where $h, k, l \in \mathbb{Z}$ [18, pp. 17–22]. Substituting Eq. (3.25) and the wave function *Ansatz* for a linear combination of plane waves,

$$\psi(\mathbf{r}) = \sum_{\mathbf{k}} C_{\mathbf{k}} e^{i\mathbf{k}\cdot\mathbf{r}}, \tag{3.26}$$

into the single-particle Schrödinger equation, Eq. (3.18), results in a system of equations:

$$\left(\frac{\mathbf{k}^2}{2} - \varepsilon_{\mathbf{k}}\right) C_{\mathbf{k}} + \sum_{\mathbf{G}} V_{\mathrm{SCF}}(\mathbf{G})\, C_{\mathbf{k}-\mathbf{G}} = 0, \tag{3.27}$$

for the plane-wave coefficients $C_{\mathbf{k}}$ and eigenenergies $\varepsilon_{\mathbf{k}}$ [20, pp. 317–321]. As the summation of $V_{\mathrm{SCF}}(\mathbf{G})\, C_{\mathbf{k}-\mathbf{G}}$ over $\mathbf{G}$ indicates, only equations involving plane-wave coefficients for wave vectors $\mathbf{k}$ that are reciprocal lattice vectors $\mathbf{G}$ apart are coupled. This means that each coupled system can be uniquely identified by a $\mathbf{k}$-vector from the 1st Brillouin zone (BZ). The number of coupled systems of equations equals N_p, which is also the number of distinct $\mathbf{k}$-vectors allowed in the 1st BZ. This restriction follows from the finite size of the supercell, consisting of N_p unit cells, and the assumption of periodic boundary conditions. Since each system couples an infinite number of equations due to the sum over $\mathbf{G}$, each system yields an infinite number of solutions—sets of plane-wave coefficients and corresponding eigenenergies—indexed by the so-called band index n [20, pp. 317–321].

For a lattice periodic potential $V_{\mathrm{SCF}}(\mathbf{r})$ and the *Ansatz* of Eq. (3.26), the single-particle Schrödinger equation is therefore solved by wave functions of the form

$$\psi_{n\mathbf{k}}(\mathbf{r}) = \sum_{\mathbf{G}} C_{n,(\mathbf{k}+\mathbf{G})} e^{i(\mathbf{k}+\mathbf{G})\cdot\mathbf{r}} = \underbrace{\sum_{\mathbf{G}} C_{n,(\mathbf{k}+\mathbf{G})} e^{i\mathbf{G}\cdot\mathbf{r}}}_{u_{n\mathbf{k}}(\mathbf{r})} e^{i\mathbf{k}\cdot\mathbf{r}} = u_{n\mathbf{k}}(\mathbf{r}) e^{i\mathbf{k}\cdot\mathbf{r}}. \tag{3.28}$$

These are called Bloch functions, first described in Felix Bloch's seminal doctoral thesis, Ref. [21], in 1928. They are composed of a lattice-periodic function, $u_{n\mathbf{k}}(\mathbf{r}) = u_{n\mathbf{k}}(\mathbf{r}+\mathbf{R})$, modulated by $e^{i\mathbf{k}\cdot\mathbf{r}}$, as indicated in Eq. (3.28) [20, pp. 317–321]. It is noteworthy that Bloch functions have a gauge freedom of a global phase, such that

$$\psi_{n\mathbf{k}}(\mathbf{r}) = e^{i\varphi_n(\mathbf{k})}\, \psi^{(0)}_{n\mathbf{k}}(\mathbf{r}), \tag{3.29}$$

where $\varphi_n(\mathbf{k})$ is real-valued and must satisfy $\varphi_n(\mathbf{k}+\mathbf{G}) = \varphi_n(\mathbf{k}) + \mathbf{G}\cdot\mathbf{R}$ [22].

Band Structure

The band indices are assigned according to the magnitude of the Bloch functions' eigenenergies $\varepsilon_{n\mathbf{k}}$, in ascending order, such that $\varepsilon_{n\mathbf{k}} \leq \varepsilon_{(n+1)\mathbf{k}}$ for each $\mathbf{k}$-vector [20, pp. 317–321]. The set of eigenenergies $\varepsilon_{n\mathbf{k}}$ specific to a material is referred to as its band structure. It is usually visualized by plotting $\varepsilon_{n\mathbf{k}}$ as $\varepsilon_n(\mathbf{k})$ along a $\mathbf{k}$-path across the 1st BZ, connecting the BZ's high-symmetry points [17, pp. 159–160][20, pp. 323–325]. The periodicity property $\psi_{n\mathbf{k}+\mathbf{G}}(\mathbf{r}) = \psi_{n\mathbf{k}}(\mathbf{r})$ restricts $\varepsilon_n(\mathbf{k})$ to span a finite energy range, defining the bandwidth of the n^{th} energy band [20, pp. 323–325]. As indicated above, energy bands are not strictly separated from one another. They can be degenerate or intersect when occupying overlapping energy regions. Furthermore, individual bands or groups of mutually degenerate bands can be separated by forbidden energy ranges, called band gaps [20, pp. 323–325].

At zero temperature, the Bloch states are filled in ascending order with respect to their corresponding eigenenergies and are doubly occupied due to spin degeneracy. The highest eigenenergy corresponding to an occupied Bloch function is the so-called Fermi energy

$$E_\mathrm{F} = \max_{n\mathbf{k}} \{\varepsilon_{n\mathbf{k}} | f_{n\mathbf{k}} \neq 0\}, \tag{3.30}$$

where $f_{n\mathbf{k}}$ is the occupation number of $\psi_{n\mathbf{k}}(\mathbf{r})$, ranging from 0 to 2 [20, pp. 265–267] [17, p. 158]. Bands with all eigenvalues entirely below E_F are called valence bands, while bands with eigenvalues greater than E_F are called conduction bands [17, p. 170]. In principle, one can distinguish two cases regarding the occupation of the conduction band to classify materials:

1. The conduction bands are completely empty: This means that E_F lies within the band gap, separating the highest energy state in the top valence band from the lowest energy state at the conduction band bottom. The magnitude of the band gap, which is usually between 1 eV and 7 eV, allows further distinction between semiconductors on the lower end and insulators on the upper end of this interval. The thermal energy at room temperature can be enough to excite electrons into the conduction-band bottom in semiconductors, while in insulators, this process is much less probable [17, pp. 169–171] [20, pp. 345–346] [18, pp. 136–142].

2. The first conduction band is partially filled: Consequently, there is no band gap between E_F and the next higher possible eigenenergies in the conduction band. The energy difference to the next higher allowed state is practically zero, and materials exhibiting this band structure are metals [17, pp. 169–171] [20, pp. 345–346] [18, pp. 136–142].

The electronic density of states (DOS), given by

$$\rho(E) = \sum_n \int_\mathrm{BZ} \frac{d\mathbf{k}}{\Omega_\mathrm{BZ}} \delta(E - \varepsilon_{n\mathbf{k}}), \tag{3.31}$$

is a useful quantity for identifying energy ranges in terms of occupancy and band gaps, rather than examining the full dispersion relation $\varepsilon_n(\mathbf{k})$. It allows for the calculation of the number of states in a given energy interval $[E, E + dE]$ as $dN = \rho(E)\, dE$, and is normalized such that

$$\int_{-\infty}^{E_\mathrm{F}} dE\, \rho(E) = N, \tag{3.32}$$

where N is the total number of electrons in the system [17, pp. 160–161].

Effective Mass of Bloch Electrons

To describe electron transport in solids, it is necessary to incorporate external forces acting on the electrons through electric and magnetic fields. This can be done semi-classically by considering classical external forces acting on Bloch electrons, which are derived from quantum mechanical principles. Additionally, it will be assumed that electrons do not jump between bands and that the eigenvalues $\varepsilon_{n\mathbf{k}}$ can be approximated as a differentiable function $\varepsilon_n(\mathbf{k})$, since derivatives of $\varepsilon_n(\mathbf{k})$ will play a key role in the following considerations [20, pp. 371–378].

The change in an electron's energy $\delta\varepsilon$, when traveling with velocity $\mathbf{v}$ and being exposed to an instantaneous external force $\mathbf{F}$, over a short time period δt, is

$$\delta\varepsilon = \mathbf{F} \cdot \mathbf{v}\, \delta t. \tag{3.33}$$

To get an expression for the classical velocity of a localized electron, as used in Eq. (3.33), one uses the group velocity of wave packets:

$$\mathbf{v}_n(\mathbf{k}) = \frac{\partial \omega_n(\mathbf{k})}{\partial \mathbf{k}} = \frac{1}{\hbar}\frac{\partial \varepsilon_n(\mathbf{k})}{\partial \mathbf{k}}, \tag{3.34}$$

constructed from Bloch wave functions within a small $\mathbf{k}$-range around $\mathbf{k}$ [20, pp. 371–378]. As shown in Ref. [20], the energy change of $\varepsilon_n(\mathbf{k})$ can also be expressed through a change $\delta\mathbf{k}$, given by

$$\delta\varepsilon_n(\mathbf{k}) = \delta\mathbf{k} \cdot \frac{\partial \varepsilon_n(\mathbf{k})}{\partial \mathbf{k}} = \hbar\, \delta\mathbf{k} \cdot \mathbf{v}_n(\mathbf{k}), \tag{3.35}$$

already incorporating Eq. (3.34). Equating Eqs. (3.33) and (3.35) then yields

$$\mathbf{F} = \hbar \frac{d\mathbf{k}}{dt}. \tag{3.36}$$

Taking the time derivative of the i^{th} component of the group velocity defined in Eq. (3.34) results in

$$\frac{dv_{n,i}(\mathbf{k})}{dt} = \frac{1}{\hbar}\frac{d}{dt}\left(\frac{\partial \varepsilon_n(\mathbf{k})}{\partial k_i}\right) = \frac{1}{\hbar^2}\sum_j^3 \frac{\partial^2 \varepsilon_n(\mathbf{k})}{\partial k_i \partial k_j} \underbrace{\hbar \frac{dk_j}{dt}}_{F_j}, \tag{3.37}$$

allowing the identification of a relation between the curvature of the band structure $\varepsilon_n(\mathbf{k})$ and the inverse of the effective mass [20, pp. 371–378]. This can be seen by using Eq. (3.36) and Newton's second law, $\dot{\mathbf{v}} = m^{-1}\,\mathbf{F}$, resulting in

$$\left[(m^*)^{-1}(\mathbf{k})\right]_{ij} = \frac{1}{\hbar^2}\frac{\partial^2 \varepsilon_n(\mathbf{k})}{\partial k_i \partial k_j}, \tag{3.38}$$

which is the inverse effective mass tensor [20, pp. 371–378]. In the case of an isotropic curvature of $\varepsilon_n(\mathbf{k})$, this symmetric tensor can be diagonalized, and the expression for the effective mass simplifies to

$$m^*(\mathbf{k}) = \hbar^2 \left(\frac{d^2 \varepsilon_n(\mathbf{k})}{dk^2} \right)^{-1}. \tag{3.39}$$

This is especially useful at the very top and bottom of bands, where the band structure can be approximated by an isotropic, parabolic dispersion [20, pp. 371–378].

3.2.3. Wannier Functions

A Bloch function $\psi_{n\mathbf{k}}(\mathbf{r})$ can be interpreted as having a discrete $\mathbf{k}$-dependence within the 1st BZ, in addition to its continuous $\mathbf{r}$-dependence. Considering only one band, it can therefore be expanded in an inverse Fourier series with respect to $\mathbf{k}$, given by

$$\psi_{n\mathbf{k}}(\mathbf{r}) = \sum_p w_{np}(\mathbf{r}) e^{i\mathbf{k}\cdot\mathbf{R}_p}, \tag{3.40}$$

where each Fourier coefficient $w_{np}(\mathbf{r})$ is associated with a unit cell p. These coefficients are known as Wannier functions, obtained through a discrete Fourier transform

$$w_{np}(\mathbf{r}) = \frac{1}{N_p} \sum_{\mathbf{k}} \underbrace{\psi_{n\mathbf{k}}(\mathbf{r}) e^{-i\mathbf{k}\cdot\mathbf{R}_p}}_{u_{n\mathbf{k}}(\mathbf{r}) e^{i\mathbf{k}\cdot(\mathbf{r}-\mathbf{R}_p)}}, \tag{3.41}$$

over the 1st BZ [23]. Eq. (3.41) naturally defines Wannier functions for so-called isolated bands, which are non-degenerate and separated to other bands. Due to the lattice periodicity of $u_{n\mathbf{k}}(\mathbf{r})$, Wannier functions can be written with a dependence on the relative position to their associated lattice point $\mathbf{R}_p$, such that $w_{np}(\mathbf{r}) = w_{n0}(\mathbf{r} - \mathbf{R}_p)$, as indicated in Eq. (3.41) [20, pp. 321–322][23, 24]. Another view on Wannier functions is to recognize them as a superposition of plane waves $e^{i\mathbf{k}\cdot\mathbf{r}}$ with amplitudes $u_{n\mathbf{k}}(\mathbf{r})$, forming a localized wave packet around lattice point $\mathbf{R}_p$, with modulation $e^{-i\mathbf{R}_p}$. This becomes even more evident when setting $\mathbf{R}_p = 0$ [22].

The definition of a Wannier function in Eq. (3.41) can be generalized to apply to so-called composite groups of bands or any group of bands in general. A composite group of J bands consists of degenerate bands which, as a whole, are separated from other bands by a finite energy gap [23]. For a given $\mathbf{k}$-vector, the trace within the manifold of J bands is invariant to a unitary gauge transformation $U_{nm\mathbf{k}}$, such that

$$\psi^{\mathrm{w}}_{m\mathbf{k}}(\mathbf{r}) = \sum_{n=1}^{J} U_{nm\mathbf{k}}\, \psi_{n\mathbf{k}}(\mathbf{r}). \tag{3.42}$$

The multi-band Wannier functions are therefore defined as

$$w_{mp}(\mathbf{r}) = \frac{1}{N_p} \sum_{\mathbf{k}} e^{-i\mathbf{k}\cdot\mathbf{R}_p}\, \psi^{\mathrm{w}}_{m\mathbf{k}}(\mathbf{r}), \tag{3.43}$$

whereas, the Bloch functions can be retrieved by

$$\psi_{n\mathbf{k}}(\mathbf{r}) = \sum_{p} \sum_{m=1}^{J} e^{i\mathbf{k}\cdot\mathbf{R}_p}\, U^{\dagger}_{mn\mathbf{k}}\, w_{mp}(\mathbf{r}), \tag{3.44}$$

as shown in Ref. [23]. The gauge freedom $e^{i\varphi_n(\mathbf{k})}$ of $\psi_{n\mathbf{k}}(\mathbf{r})$ and the Wannier gauge transformation $U_{nm\mathbf{k}}$ make it clear that Wannier functions are highly non-unique. However, these gauges can be utilized to impose certain properties onto $w_{mp}(\mathbf{r})$ [23]. For example, $U_{nm\mathbf{k}}$ can be chosen to obtain maximally localized Wannier functions (MLWF). This is achieved by minimizing the Wannier function's spread,

$$\sigma^2 = \sum_{n} \left[\langle w_{m0} |\, \mathbf{r}^2 \,| w_{m0} \rangle - \langle w_{m0} |\, \mathbf{r} \,| w_{m0} \rangle^2 \right], \tag{3.45}$$

with respect to $U_{nm\mathbf{k}}$. It has been proven that MLWFs exhibit an exponential decay in $\mathbf{r}$, which is also referred to as exponential localization [23] [22] [24].

3.3. Lattice Vibrations and Phonons

3.3.1. Lattice Vibrations

In a crystalline structure, nuclei can be indexed with κ, denoting their role within the atomic basis, and p, identifying their associated unit cell, such that $(\kappa,\, p) \equiv I$. Thus, the expression $\tau_{\kappa\alpha p}$ refers to the α component of the κ^{th} nucleus in the p^{th} unit cell. Furthermore, the number of unit cells is N_p, the number of nuclei in one unit cell is M_{uc}, and the dimension of the lattice is denoted as d.

Following this notation and considering the nuclei as classical particles in the electronic ground-state BO potential $U(\{\boldsymbol{\tau}_{\kappa p}\})$, the set of nuclear positions that minimize $U(\{\boldsymbol{\tau}_{\kappa p}\})$ are the nuclei's equilibrium positions $\boldsymbol{\tau}^0_{\kappa p}$, where $\boldsymbol{\tau}^0_{\kappa p} = \mathbf{R}_p + \boldsymbol{\tau}_{\kappa}$. Then, each atom's position can be written in terms of its displacement from its equilibrium position as $\boldsymbol{\tau}_{\kappa p} = \boldsymbol{\tau}^0_{\kappa p} + \Delta\boldsymbol{\tau}_{\kappa p}$ [9, 24]. For sufficiently small displacements $\Delta\boldsymbol{\tau}_{\kappa p}$, the effective potential

can be approximated around the nuclei's equilibrium positions as

$$U(\{\boldsymbol{\tau}_{\kappa p}\}) = \underbrace{U(\{\boldsymbol{\tau}^0_{\kappa p}\})}_{U_0} + \sum_{\kappa\alpha p} \underbrace{\left.\frac{\partial U}{\partial \tau_{\kappa\alpha p}}\right|_{\{\boldsymbol{\tau}^0_{\kappa p}\}}}_{=0} \Delta\tau_{\kappa\alpha p} + \frac{1}{2} \sum_{\substack{\kappa\alpha p \\ \kappa'\alpha' p'}} \underbrace{\left.\frac{\partial^2 U}{\partial \tau_{\kappa\alpha p} \partial \tau_{\kappa'\alpha' p'}}\right|_{\{\boldsymbol{\tau}^0_{\kappa p}\}}}_{C_{\kappa\alpha p,\kappa'\alpha' p'}} \Delta\tau_{\kappa\alpha p}\Delta\tau_{\kappa'\alpha' p'} + \mathcal{O}(\Delta\boldsymbol{\tau}^3). \tag{3.46}$$

This expansion of $U(\{\boldsymbol{\tau}_{\kappa p}\})$ up to the second order, is called the harmonic approximation, whereas the first-order term vanishes because the first derivative of $U(\{\boldsymbol{\tau}_{\kappa p}\})$ is evaluated at the equilibrium positions $\boldsymbol{\tau}^0_{\kappa p}$ [24, 19] [18, pp. 41–47]. The second-order term defines the interatomic force constants $C_{p\alpha\kappa,p'\alpha'\kappa'}$ at the equilibrium positions. This symmetric $N_p \cdot d \cdot M_{\text{uc}} \times N_p \cdot d \cdot M_{\text{uc}}$ matrix encodes the force acting on nucleus κp in direction α resulting from the displacement of nucleus $\kappa' p'$ by $\Delta\tau_{\kappa'\alpha' p'}$ in direction α' [18, pp. 41–47].

Using the *Ansatz*

$$\Delta\tau_{\kappa\alpha p}(t) = \frac{1}{\sqrt{M_\kappa}} v_{\kappa\alpha p} e^{-i\omega t} \tag{3.47}$$

for the time dependence of the displacements and plugging it into the equations of motion,

$$M_\kappa \Delta\ddot{\tau}_{\kappa\alpha p} = -\frac{\partial V}{\partial \Delta\tau_{\kappa\alpha p}} = -\sum_{\kappa'\alpha' p'} C_{\kappa\alpha p,\kappa'\alpha' p'} \Delta\tau_{\kappa'\alpha' p'}, \tag{3.48}$$

results in the eigenvalue problem

$$\omega^2 v_{\kappa\alpha p} = \sum_{\kappa'\alpha' p'} \frac{C_{\kappa\alpha p,\kappa'\alpha' p'}}{\sqrt{M_\kappa M_{\kappa'}}} v_{\kappa'\alpha' p'}. \tag{3.49}$$

Furthermore, the plane-wave *Ansatz* for $\Delta\tau_{\kappa\alpha p}(t)$ is completed with

$$v_{\kappa\alpha p} = w_{\kappa\alpha} e^{i\mathbf{q}\cdot\mathbf{R}_p}, \tag{3.50}$$

as shown in Ref. [18, pp. 41–47].

Utilizing the fact that the force constants matrix is translationally invariant with respect to lattice vectors, such that

$$C_{\kappa\alpha p,\kappa'\alpha' p'} = C_{\kappa\alpha,\kappa'\alpha'}(\mathbf{R}_p - \mathbf{R}_{p'}), \tag{3.51}$$

leads to

$$\omega^2 w_{\kappa\alpha} = \sum_{\kappa'\alpha'} w_{\kappa'\alpha'} \sum_{p'} \frac{C_{\kappa\alpha,\kappa'\alpha'}(\mathbf{R}_p - \mathbf{R}_{p'})}{\sqrt{M_{\kappa'} M_\kappa}} e^{i\mathbf{q}\cdot(\mathbf{R}_{p'} - \mathbf{R}_p)}$$

$$\sum_{\kappa'\alpha'} w_{\kappa'\alpha'} \sum_{\mathbf{R}} \underbrace{\frac{C_{\kappa\alpha,\kappa'\alpha'}(\mathbf{R})}{\sqrt{M_{\kappa'} M_\kappa}}}_{D_{\kappa\alpha,\kappa'\alpha'}(\mathbf{R})} e^{-i\mathbf{q}\cdot\mathbf{R}} = \sum_{\kappa'\alpha'} w_{\kappa'\alpha'} D_{\kappa\alpha,\kappa'\alpha'}(\mathbf{q}). \tag{3.52}$$

The sum over all lattice vectors partially diagonalizes $D_{\kappa\alpha,\kappa'\alpha'}(\mathbf{R})$ via Fourier transformation, thereby decomposing the eigenvalue problem from Eq. (3.49) into N_p separate $\mathbf{q}$-vector dependent $d \cdot M_{\text{uc}} \times d \cdot M_{\text{uc}}$ dimensional eigenvalue problems [18, pp. 41–47].

The $d \cdot M_{\text{uc}}$ dimensional eigenvectors $\mathbf{e}_\nu(\mathbf{q})$, referred to as normal modes of vibration, diagonalize $D_{\kappa\alpha,\kappa'\alpha'}(\mathbf{q})$ with eigenvalues $\omega^2_{\mathbf{q}\nu}$ and are inherently orthogonal due to the Hermiticity of the dynamical matrix. Each of the $d \cdot M_{\text{uc}}$ modes for a wave vector $\mathbf{q}$, labeled by ν, represents an independent harmonic oscillator with eigenfrequency $\omega_{\mathbf{q}\nu}$. A normal mode vector $\mathbf{e}_\nu(\mathbf{q})$ is composed of M_{uc} d-dimensional polarization vectors $\mathbf{e}_{\kappa,\nu}(\mathbf{q})$. These encode the displacement directions, magnitudes, and relative phases for the oscillations of the individual nuclei in the unit cell [24, pp. 7–8][18, pp. 41–47].

The vibrational modes in a crystal can be categorized into longitudinal and transverse branches, corresponding to atomic displacements parallel and perpendicular to $\mathbf{q}$, respectively. These are further divided into acoustic and optical branches:

- There are d acoustic branches, for which the phase of each atom's oscillation is solely determined by its equilibrium position $\boldsymbol{\tau}^0_{\kappa p}$ and the plane wave vector $\mathbf{q}$. Hence, there are no additional relative phases between different nuclei within the unit cell. One of these branches is longitudinal, while $d-1$ are transverse. As $\mathbf{q} \to 0$, they all exhibit a linear dispersion relation of $\omega_{\mathbf{q}\nu} \propto |q|$, with $\omega_{\mathbf{q}\nu} = 0$ at $\mathbf{q} = 0$ [18, pp. 53–54, pp. 73–81][20, pp.180–193].

- For materials with two or more atoms in the unit cell, optical branches arise. Since there are d acoustic branches, the number of optical branches is given by $d \cdot (M_{\text{uc}} - 1)$. Optical modes are characterized by distinct displacement directions, magnitudes, and additional relative phases for the oscillations of different atoms within the unit cell. This means that nuclei from the same the unit cell oscillate out of phase with one another, while sharing the same frequency $\omega_{\mathbf{q}\nu}$ and following the same plane wave pattern, described by $\mathbf{q}$, across the entire crystal. For example, in a material with a diatomic basis, the optical modes at $\mathbf{q} = 0$ exhibit diametrically opposing oscillations of the two atomic species [18, pp. 53–54, pp. 73–81][20, pp.180–193].

To ensure translational invariance in a finite supercell measuring M_α unit cells along direction α, periodic boundary conditions are imposed on functions defined on the lattice, such that $f(\mathbf{R}) = f(\mathbf{R} + M_\alpha \mathbf{a}_\alpha)$. As a consequence of these so-called Born-von-Kármán boundary conditions, only a discrete set of $\mathbf{q}$-vectors satisfying

$$q_\alpha = \frac{l_\alpha}{M_\alpha}, \tag{3.53}$$

with $l_\alpha \in \mathbb{Z}$, is allowed. Additionally, it is sufficient to consider $\mathbf{q}$-vectors from the 1st BZ since any function $f(\mathbf{R}_p)$ or $f(\mathbf{q})$, defined on the periodic lattice, can be expressed as a Fourier series containing the factor $e^{-i\mathbf{q}\cdot\mathbf{R}}$, which is invariant with respect to the addition of reciprocal lattice vectors $\mathbf{G}$ to $\mathbf{q}$ [18, pp. 47–50].

Combining all of the above, the general solution to Eq. (3.48) is a linear combination of the displacements of independent harmonic oscillators, written as

$$\Delta\boldsymbol{\tau}_{\kappa p}(t) = \sum_{\mathbf{q}\nu} \frac{1}{\sqrt{M_\kappa}} \mathbf{e}_{\kappa,\nu}(\mathbf{q})\, e^{i\mathbf{q}\cdot\mathbf{R}_p} \underbrace{\left[A_\nu(\mathbf{q}) e^{-i\omega_{\mathbf{q}\nu}t} + B_\nu(\mathbf{q}) e^{i\omega_{\mathbf{q}\nu}t}\right]}_{u_{\mathbf{q}\nu}(t)}, \tag{3.54}$$

where the amplitudes $A_\nu(\mathbf{q})$ and $B_\nu(\mathbf{q})$ are determined from the initial conditions of the system [18, pp. 41–47][17, pp. 115–122].

3.3.2. Phonons

In the previous section, harmonic lattice vibrations were separated into independent normal mode vibrations. Using Eq. (3.54), the nuclear Schrödinger equation in the BO and harmonic approximations,

$$\left[-\sum_{\kappa\alpha p} \frac{m_e}{2M_I} \frac{\partial^2}{\partial \Delta\tau_{\kappa\alpha p}^2} + \frac{1}{2} \sum_{\substack{\kappa\alpha p \\ \kappa'\alpha' p'}} C_{p\alpha\kappa,p'\alpha'\kappa'} \Delta\tau_{\kappa\alpha p} \Delta\tau_{\kappa'\alpha' p'}\right] \chi = (E_{\text{tot}} - U_0)\, \chi, \tag{3.55}$$

can be rewritten in terms of time-independent normal mode coordinates $u_{\mathbf{q}\nu}$. Subsequently, the nuclear wave function $\Xi(\{u_{\mathbf{q}\nu}(\{\Delta\boldsymbol{\tau}_{\kappa p}\})\}) \equiv \chi(\{\Delta\boldsymbol{\tau}_{\kappa p}\})$ can be written as a product of $N_p \cdot d \cdot M_{\text{uc}}$ independent quantum mechanical harmonic oscillator wave functions $\Phi_{\mathbf{q}\nu}(u_{\mathbf{q}\nu})$. Each of them satisfies the single-particle Schrödinger equation

$$\left[-\frac{1}{2}\frac{\partial^2}{\partial u_{\mathbf{q}\nu}^2} + \frac{1}{2}\omega_{\mathbf{q}\nu} u_{\mathbf{q}\nu}^2\right] \Phi_{\mathbf{q}\nu}(u_{\mathbf{q}\nu}) = E_{\mathbf{q}\nu}\, \Phi_{\mathbf{q}\nu}(u_{\mathbf{q}\nu}), \tag{3.56}$$

as shown in Ref. [17, pp. 137–140].

The solutions to this equation are the Hermite functions $f_{n_{\mathbf{q}\nu}}(u_{\mathbf{q}\nu})$ and their corresponding eigenenergies

$$E_{\mathbf{q}\nu} = \left(n_{\mathbf{q}\nu} + \frac{1}{2}\right) \omega_{\mathbf{q}\nu}, \tag{3.57}$$

with $n_{\mathbf{q}\nu} \in \mathbb{N}_0$. The total energy is therefore composed of the minimum of the potential energy surface U_0 and the eigenenergies $E_{\mathbf{q}\nu}$ from all independent oscillators, yielding

$$E_{\text{tot}} = U_0 + \sum_{\mathbf{q}\nu} \left(n_{\mathbf{q}\nu} + \frac{1}{2}\right) \hbar\omega_{\mathbf{q}\nu}. \tag{3.58}$$

The phonon energy in Eq. (3.58) inherits well-known properties from the quantum mechanical harmonic oscillator: the energy in each vibrational mode is quantized in steps of $\hbar\omega_{\mathbf{q}\nu}$, and $n_{\mathbf{q}\nu}$ is the number of phonons occupying mode $\mathbf{q}\nu$. The ground-state energy is $\hbar\omega_{\mathbf{q}\nu}/2$, and the total energy is defined by the number of phonons $n_{\mathbf{q}\nu}$ in each mode [17, pp. 137–140].

Ref. [24] states two more relations which will referenced in the next section: Using the language of second quantization, the phonon Hamiltonian has the form

$$\hat{H}_{\text{ph}} = \sum_{\mathbf{q}\nu} \hbar\omega_{\mathbf{q}\nu} \left(\hat{n}_{\mathbf{q}\nu} + \frac{1}{2}\right) = \sum_{\mathbf{q}\nu} \hbar\omega_{\mathbf{q}\nu} \left(\hat{a}^\dagger_{\mathbf{q}\nu}\hat{a}_{\mathbf{q}\nu} + \frac{1}{2}\right). \tag{3.59}$$

Another useful relation in terms of $\hat{a}^\dagger_{\mathbf{q}\nu}$ and $\hat{a}_{\mathbf{q}\nu}$, the phonon creation and annihilation operators, respectively, is the total displacement of the κ^{th} nucleus in unit cell p, calculated as

$$\Delta\boldsymbol{\tau}_{\kappa p} = \sum_{\mathbf{q}\nu} \sqrt{\frac{\hbar}{2N_p M_\kappa \omega_{\mathbf{q}\nu}}} e^{i\mathbf{q}\cdot\mathbf{R}_p} \, \mathbf{e}_{\kappa,\nu}(\mathbf{q}) \, \left(\hat{a}_{\mathbf{q}\nu} + \hat{a}^\dagger_{-\mathbf{q}\nu}\right), \tag{3.60}$$

superimposing the displacements of all phonon modes [24].

3.4. Electron-Phonon Interaction

In previous sections, the electronic behavior has been discussed based on the assumption that the nuclei are clamped at their equilibrium positions. The phonon dispersion has then been derived based on the interatomic force constants, which are the second-order derivatives of the BO potential. In this section, the previously obtained phonon dispersion will be fed back into the Hamiltonian of the single-electron Schrödinger equation, allowing interactions between electrons and phonons.

In a first step, the self-consistent-field potential will be expanded around the nuclei's equilibrium positions, resulting in

$$V_{\mathrm{SCF}}(\mathbf{r};\{\boldsymbol{\tau}_{\kappa p}\}) = V_{\mathrm{SCF}}(\mathbf{r};\{\boldsymbol{\tau}^0_{\kappa p}\}) + \sum_{\kappa\alpha p} \Delta\tau_{\kappa\alpha p} \underbrace{\left.\frac{\partial V_{\mathrm{SCF}}(\mathbf{r};\{\boldsymbol{\tau}_{\kappa p}\})}{\partial \boldsymbol{\tau}_{\kappa\alpha p}}\right|_{\{\boldsymbol{\tau}^0_{\kappa p}\}}}_{\equiv \partial_{\kappa\alpha p} V_{\mathrm{SCF}}(\mathbf{r})} + \mathcal{O}(\Delta\boldsymbol{\tau}^2), \quad (3.61)$$

as shown in Ref. [18, pp. 253–258]. Plugging the first-order expression into the single-particle Hamiltonian from Eq. (3.15) yields:

$$\hat{h}(\mathbf{r}) = \underbrace{\frac{\boldsymbol{\nabla}_i^2}{2} + V_{\mathrm{SCF}}(\mathbf{r};\{\boldsymbol{\tau}^0_{\kappa p}\})}_{\text{Diagonal in the Bloch basis.}} + \underbrace{\sum_{\kappa\alpha p} \Delta\tau_{\kappa\alpha p}\, \partial_{\kappa\alpha p} V_{\mathrm{SCF}}(\mathbf{r})}_{V_{\text{e-ph}}(\mathbf{r})}. \quad (3.62)$$

Considering $\hat{h}(\mathbf{r})$ in the Bloch basis, the first two terms—which were already treated in Bloch's theorem—contribute diagonal matrix elements. Moreover, the third term contributes off-diagonal matrix elements and represents the electron-phonon interaction up to first order, as derived in Ref. [18, pp. 253–258]. Summing over all single-electron Hamiltonians, as defined in Eq. (3.62), and using the language of second quantization, yields:

$$\hat{H}_0 = \underbrace{\sum_{n\mathbf{k}} \varepsilon_{n\mathbf{k}}\, \hat{c}^\dagger_{n\mathbf{k}} \hat{c}_{n\mathbf{k}}}_{\hat{H}_{\mathrm{e}}} + \underbrace{\sum_{n\mathbf{k},m\mathbf{k}'} \langle \psi_{n\mathbf{k}} |\, V_{\text{e-ph}}(\mathbf{r})\, |\psi_{m\mathbf{k}'}\rangle\, \hat{c}^\dagger_{m\mathbf{k}'} \hat{c}_{n\mathbf{k}}}_{\hat{H}_{\text{e-ph}}}, \quad (3.63)$$

with electronic creation and annihilation operators $\hat{c}^\dagger_{n\mathbf{k}}$ and $\hat{c}_{n\mathbf{k}}$, respectively, as explained in Ref. [18, pp. 253–258]. Furthermore, expressing $\Delta\tau_{\kappa\alpha p}$ in terms of phonon modes, as given by Eq. (3.60), and evaluating the integral $\langle \psi_{n\mathbf{k}} |\, V_{\text{e-ph}}(\mathbf{r})\, |\psi_{m\mathbf{k}'}\rangle$ over the supercell, finally leads to

$$\hat{H}_{\text{e-ph}} = \frac{1}{\sqrt{N_p}} \sum_{\substack{\mathbf{k}\,\mathbf{q} \\ mn\nu}} g_{mn\nu}(\mathbf{k},\mathbf{q})\, \hat{c}^\dagger_{m\mathbf{k}+\mathbf{q}} \hat{c}_{n\mathbf{k}} \left(\hat{a}_{\mathbf{q}\nu} + \hat{a}^\dagger_{-\mathbf{q}\nu}\right), \quad (3.64)$$

with the electron-phonon coupling strengths

$$g_{mn\nu}(\mathbf{k},\mathbf{q}) = \langle u_{m\mathbf{k}+\mathbf{q}} |\, \Delta_{\mathbf{q}\nu} v_{\mathrm{SCF}}\, |u_{n\mathbf{k}}\rangle \quad (3.65)$$

and

$$\Delta_{\mathbf{q}\nu} v_{\mathrm{SCF}}(\mathbf{r}) = \sum_{\kappa} \sqrt{\frac{\hbar}{2M_\kappa \omega_{\mathbf{q}\nu}}} \sum_{\alpha} e_{\kappa\alpha,\nu}(\mathbf{q}) \underbrace{\sum_{p} e^{-i\mathbf{q}\cdot(\mathbf{r}-\mathbf{R}_p)}\, \partial_{\kappa\alpha 0} V_{\mathrm{SCF}}(\mathbf{r}-\mathbf{R}_p)}_{\equiv \partial_{\kappa\alpha,\mathbf{q}} v_{\mathrm{SCF}}(\mathbf{r})}$$

$$= \sum_{\kappa} \sqrt{\frac{\hbar}{2M_\kappa \omega_{\mathbf{q}\nu}}} \sum_{\alpha} e_{\kappa\alpha,\nu}(\mathbf{q})\, \partial_{\kappa\alpha,\mathbf{q}} v_{\mathrm{SCF}}(\mathbf{r}), \tag{3.66}$$

as stated in Refs. [24][18, pp. 253–258]. The quantity $\Delta_{\mathbf{q}\nu} v_{\mathrm{SCF}}(\mathbf{r})$ represents the linear response of the self-consistent-field potential with respect to phonon mode $\mathbf{q}\nu$. It incorporates the Cartesian-based derivatives $\partial_{\kappa\alpha,\mathbf{q}} v_{\mathrm{SCF}}(\mathbf{r})$ for all nuclei within the unit cell. These derivatives are projected onto the polarization vectors $e_{\kappa\alpha,\nu}(\mathbf{q})$, which correspond to phonon mode $\mathbf{q}\nu$, and are weighted by the zero-point displacement associated with nucleus κ [24][18, pp. 253–258].

The electron-phonon Hamiltonian $\hat{H}_{\text{e-ph}}$, as given in Eq. (3.64), reveals a clear physical picture and accounts for energy contributions of two similar electron-phonon scattering scenarios:

1. The term involving the phonon annihilation operator $\hat{a}_{\mathbf{q}\nu}$ in Eq. (3.64) describes the process of an electron with wave vector $\mathbf{k}$ and band index n absorbing a phonon with wave vector $\mathbf{q}$. The electron is thus scattered to band m and acquires the phonon's momentum $\mathbf{q}$, resulting in a total wave vector of $\mathbf{k}+\mathbf{q}$ [24][18, pp. 253–258].

2. The second term, involving the phonon creation operator $\hat{a}^\dagger_{-\mathbf{q}\nu}$, describes the scattering of an electron from $n\mathbf{k}$ to $m\mathbf{k}+\mathbf{q}$, obeying momentum conservation through the creation of a phonon with wave vector $-\mathbf{q}$ [24][18, pp. 253–258].

Incorporating the pure phonon contribution $\hat{H}_{\mathrm{ph}}$ from Eq. (3.59) yields the full Hamiltonian for the electron-phonon system:

$$\begin{aligned}\hat{H} =& \sum_{n\mathbf{k}} \varepsilon_{n\mathbf{k}}\, \hat{c}^\dagger_{n\mathbf{k}} \hat{c}_{n\mathbf{k}} \\ &+ \sum_{\mathbf{q}\nu} \hbar\omega_{\mathbf{q}\nu} \left(\hat{a}^\dagger_{\mathbf{q}\nu} \hat{a}_{\mathbf{q}\nu} + \frac{1}{2} \right) \\ &+ \frac{1}{\sqrt{N_p}} \sum_{\substack{\mathbf{k}\,\mathbf{q} \\ mn\nu}} g_{mn\nu}(\mathbf{k},\mathbf{q})\, \hat{c}^\dagger_{m\mathbf{k}+\mathbf{q}} \hat{c}_{n\mathbf{k}} \left(\hat{a}_{\mathbf{q}\nu} + \hat{a}^\dagger_{-\mathbf{q}\nu} \right),\end{aligned} \tag{3.67}$$

as stated in Refs. [24][18, pp. 253–258].

Chapter 4

Density Functional Theory

The approximation methods discussed in Section 3.2 for calculating the electronic ground-state wave function either neglect substantial parts of the electron-electron interaction—such as in independent electron or mean-field approximations—or present an exponentially hard problem, e.g. the discretization of real space. Although no known method circumvents the exponential increase in computational cost with increasing system size when solving for the exact ground-state wave function, DFT provides a framework for obtaining good approximations of many ground-state properties of materials while significantly reducing the required computational effort compared to more direct methods [17, p. 36, p. 49].

4.1. Hohenberg-Kohn Theorem

The Hohenberg-Kohn Theorem, presented in Ref. [25] and published in 1964, forms the foundation of DFT. In the first line of argument, the electronic ground-state wave function $\psi_0(\{\mathbf{r}_i\})$ is shown to be a unique functional of the electronic ground-state density

$$n(\mathbf{r}) = N \int |\psi_0(\mathbf{r}, \mathbf{r_2}, \cdots, \mathbf{r_N})|^2 \, d\mathbf{r_2} \cdots d\mathbf{r_N}. \tag{4.1}$$

The proof, using *reductio ad absurdum*, demonstrates that the external potential $V_{\text{e-n}}(\mathbf{r})$ is uniquely determined by $n(\mathbf{r})$, up to a constant. Moreover, the ground-state density uniquely defines a Hamiltonian of the form given in Eq. (3.12), and therefore also defines the associated ground-state wave function as $\psi_0(\{\mathbf{r}_i\}) \equiv \psi_0[n]$ [25, 17].

Based on this argument, the ground-state energy is found to be a functional of $n(\mathbf{r})$, given by

$$\underbrace{E[\psi_0[n]]}_{E[n]} = \int V_{\text{e-n}}(\mathbf{r}) n(\mathbf{r}) \, d\mathbf{r} + \underbrace{\langle \psi_0[n] | \, \hat{T}_{\text{e}} + V_{\text{e-e}} \, | \psi_0[n] \rangle}_{F[n]}. \tag{4.2}$$

The electrons' kinetic energy and the electron-electron interaction energy are expressed by the universal functional $F[n]$, which accounts for an arbitrary number of electrons and

is independent of the form of the external potential [25]. However, it still needs to be shown that $E[n]$ has its minimum at $n[\psi_0]$, such that finding $n[\psi_0]$ can be approached as a variational problem: A charge density n' which differs from $n[\psi_0]$ yields an external potential $V_n' \neq V_{\text{e-n}} + \text{const.}$, thereby altering the original Hamiltonian to $\hat{H}'$ with ground state $\psi_0' \neq \psi_0$. Since ψ_0 minimizes the original energy functional of Eq. (4.2), it must hold that

$$E[\psi_0[n]] < E\big[\psi_0'\big[n'\big]\big]\,, \tag{4.3}$$

such that $n[\psi_0]$ can be found by minimizing $E[n]$ with respect to n [25].

4.2. Kohn-Sham Equations

Hohenberg and Kohn proceeded by rewriting the universal functional $F[n]$ as

$$F[n] = \frac{1}{2}\iint \frac{n(\mathbf{r})n(\mathbf{r}')}{|\mathbf{r}-\mathbf{r}'|}\,d\mathbf{r}d\mathbf{r}' + G[n]\,, \tag{4.4}$$

by separating out the Hartree energy [25]. Kohn and Sham advanced further by splitting $G[n]$ into

$$G[n] = T_{\text{s}}[n] + E_{\text{xc}}[n]\,, \tag{4.5}$$

the single-particle kinetic energy $T_{\text{s}}[n]$ and the exchange-correlation energy $E_{\text{xc}}[n]$ [26].

The exchange-correlation energy can only be approximated, as its exact form is unknown. One approximation approach is to discretize space and separately evaluate the exchange-correlation energy for each cell volume, assuming a homogeneous electron gas with an electron density specific to each cell. This approach is known as the local density approximation (LDA) and is widely used in DFT calculations. The exchange energy $E_{\text{X}}(n)$ for a homogeneous electron gas is known analytically, whereas the correlation energy $E_{\text{C}}(n)$ is calculated using an interpolation formula based on numerical solutions of the many-body Schrödinger equation for the homogeneous electron gas, obtained with stochastic numerical methods [17, pp. 36–50, pp. 243–245].

By substituting Eqs. (4.4) and (4.5) into Eq. (4.2), one arrives at

$$E[n] = -\sum_i \int \varphi_i^*(\mathbf{r})\frac{\boldsymbol{\nabla}^2}{2}\varphi_i(\mathbf{r})\,d\mathbf{r} + \frac{1}{2}\iint \frac{n(\mathbf{r})n(\mathbf{r}')}{|\mathbf{r}-\mathbf{r}'|}\,d\mathbf{r}d\mathbf{r}' + E_{\text{xc}}[n] + \int V_{\text{e-n}}(\mathbf{r})n(\mathbf{r})\,d\mathbf{r} \tag{4.6}$$

with

$$n(\mathbf{r}) = \sum_i |\varphi_i(\mathbf{r})|^2. \tag{4.7}$$

Applying the Hohenberg-Kohn variational principle by imposing the conditions

$$\frac{\delta E[n]}{\delta n} = 0, \tag{4.8}$$

and

$$\langle \varphi_i | \varphi_j \rangle = \delta_{ij}, \tag{4.9}$$

to determine the electronic ground-state density while ensuring orthonormal orbitals, leads to the so-called Kohn-Sham equations:

$$\hat{H}_{\mathrm{KS}}[n(\mathbf{r})]\ \varphi_i(\mathbf{r}) = \left[-\frac{\boldsymbol{\nabla}^2}{2} + \underbrace{V_{\text{e-n}}(\mathbf{r}) + V_{\mathrm{H}}(\mathbf{r}) + V_{\mathrm{xc}}(\mathbf{r})}_{V_{\mathrm{KS}}(\mathbf{r})} \right] \varphi_i(\mathbf{r}) = \varepsilon_i\, \varphi_i(\mathbf{r}), \tag{4.10}$$

as described in Ref. [17, pp. 36–50, pp. 243–245]. These are self-consistent single-particle equations for the Kohn-Sham orbitals $\varphi_i(\mathbf{r})$ and Kohn-Sham eigenvalues ε_i. The exchange-correlation potential $V_{\mathrm{xc}}(\mathbf{r})$ captures all many-body effects, which are ignored in the mean-field approach. It is obtained as the functional derivative of the exchange-correlation energy,

$$V_{\mathrm{xc}}(\mathbf{r}) = \left. \frac{\delta E_{\mathrm{xc}}[n]}{\delta n} \right|_{n(\mathbf{r})}, \tag{4.11}$$

and is therefore also a self-consistently obtained approximation [17, pp. 36–50, pp. 243–245]. The effective potential, obtained from $n(\mathbf{r})$, which acts on the Kohn-Sham orbitals is referred to as the Kohn-Sham potential $V_{\mathrm{KS}}(\mathbf{r})$ [24]. Following the convention introduced for the Hartree approximation in Subsection 3.2.1, the Kohn-Sham potential obtained from the ground-state density, which satisfies Eqs. (4.10) self-consistently, is generally referred to as the self-consistent-field potential $V_{\mathrm{SCF}}(\mathbf{r})$ [19].

The total electronic DFT energy can also be expressed in terms of Kohn-Sham eigenvalues ε_i and their occupation numbers f_i as

$$E = \sum_i f_i\, \varepsilon_i - \frac{1}{2} \int \frac{n(\mathbf{r}) n(\mathbf{r}')}{|\mathbf{r} - \mathbf{r}'|}\, d\mathbf{r} d\mathbf{r}' + E_{\mathrm{xc}}\left[n(\mathbf{r})\right] - \int n(\mathbf{r}) V_{\mathrm{xc}}(\mathbf{r})\, d\mathbf{r}, \tag{4.12}$$

as described in Refs. [26] and [17, pp. 153–154].

4.3. Derivatives in Density Functional Theory

4.3.1. Hellmann-Feynman Theorem

The Hellmann-Feynman theorem, given by

$$\frac{\partial E_n(\{\lambda_k\})}{\partial \lambda_j} = \langle \Psi_n | \frac{\partial \hat{H}(\{\lambda_k\})}{\partial \lambda_j} | \Psi_n \rangle, \tag{4.13}$$

allows the calculation of first-order derivatives of eigenenergies $E_n(\{\lambda_k\})$ with respect to any of the Hamiltonian's external parameters λ_k. In its most general form, it requires knowledge of the eigenstate $|\Psi_n\rangle$ and the derivative of $\hat{H}(\{\lambda_k\})$ with respect to the considered external parameter λ_j [19]. For ground-state properties, the knowledge of the electronic ground-state density $n(\mathbf{r})$ is sufficient. For example, the force acting on the I^{th} nucleus is given by

$$\mathbf{F}_I = -\frac{\partial U(\{\boldsymbol{\tau}_J\})}{\partial \boldsymbol{\tau}_I} = -\underbrace{\int d\mathbf{r}\, n(\mathbf{r}) \frac{\partial V_{\text{e-n}}(\mathbf{r}, \{\boldsymbol{\tau}_J\})}{\partial \boldsymbol{\tau}_I}}_{\text{electronic}} - \underbrace{\frac{\partial V_{\text{n-n}}(\{\boldsymbol{\tau}_J\})}{\partial \boldsymbol{\tau}_I}}_{\text{ionic}}, \tag{4.14}$$

requiring $n(\mathbf{r})$ and the derivatives of the potentials $V_{\text{e-n}}(\mathbf{r}, \{\boldsymbol{\tau}_J\})$ and $V_{\text{n-n}}(\{\boldsymbol{\tau}_J\})$ [19].

The forces calculated from Eq. (4.14) are typically used for obtaining the equilibrium structure of materials. Since the nuclei's positions $\boldsymbol{\tau}_I$ parameterize a $3N$-dimensional energy surface, and the forces $\mathbf{F}_I$ represent the corresponding (negative) gradient, the 'steepest descent' or 'conjugate gradient' methods are well suited for the task of structural relaxation [17, pp. 59–65]. The procedure of finding the nuclei's equilibrium positions consists of two steps, which are repeated until the forces fall below a convergence threshold:

1. A self-consistent calculation using the updated positions $\boldsymbol{\tau}_I$ from previous gradient descent steps to obtain $\mathbf{F}_I$ according to Eq. (4.14).

2. A gradient descent step using $\mathbf{F}_I$ to update the nuclei's positions $\boldsymbol{\tau}_I$ [17, pp. 59–65].

4.3.2. Density Functional Perturbation Theory

For calculating quantities that require second-order derivatives of $E_0(\{\lambda_k\})$, such as the interatomic force constants, the knowledge of $n(\mathbf{r})$ alone is no longer sufficient. This can be seen when calculating a second-order derivative of the electronic part of the BO energy surface from differentiating Eq. (4.14) with respect to $\tau_{I\alpha}$, yielding

$$\frac{\partial^2 E_0^{\text{el}}(\{\boldsymbol{\tau}_K\})}{\partial \tau_{I\alpha} \partial \tau_{J\beta}} = \int d\mathbf{r}\, n(\mathbf{r}) \frac{\partial^2 V_{\text{e-n}}(\mathbf{r}, \{\boldsymbol{\tau}_K\})}{\partial \tau_{I\alpha} \partial \tau_{J\beta}} + \int d\mathbf{r}\, \frac{\partial n(\mathbf{r})}{\partial \tau_{I\alpha}} \frac{\partial V_{\text{e-n}}(\mathbf{r}, \{\boldsymbol{\tau}_K\})}{\partial \tau_{J\beta}}. \tag{4.15}$$

The expression $\partial n(\mathbf{r})/\partial \tau_{I\alpha}$, appearing in Eq. (4.15), is the linear response of $n(\mathbf{r})$ to a change in $\tau_{I\alpha}$ [19, 27]. This quantity can be obtained by linearizing the problem and using perturbation theory:

The variation Δf of a quantity f, with respect to the set of variations $\Delta\lambda_k$ of parameters λ_k is defined as:

$$\Delta f = \sum_k \frac{\partial f}{\partial \lambda_k} \Delta\lambda_k. \tag{4.16}$$

Following this prescription, the variation of the ground-state density due to the variations $\Delta\psi_n(\mathbf{r})$ of the Kohn-Sham orbitals is

$$\Delta n(\mathbf{r}) = 4\sum_{n}^{N/2} \psi_n^*(\mathbf{r})\Delta\psi_n(\mathbf{r}), \tag{4.17}$$

where the $\Delta\psi_n(\mathbf{r})$, with $n \equiv (v, \mathbf{k})$ for valence bands v, are obtained from first-order standard perturbation theory [19]:

$$(\hat{H}_{\mathrm{SCF}} - \varepsilon_n)\,|\Delta\psi_n\rangle = -(\Delta V_{\mathrm{SCF}} - \Delta\varepsilon_n)\,|\psi_n\rangle\,. \tag{4.18}$$

The standard expressions,

$$\Delta\varepsilon_n = \langle\psi_n|\,\Delta V_{\mathrm{SCF}}\,|\psi_n\rangle\,, \tag{4.19}$$

$$\Delta\psi_n(\mathbf{r}) = \sum_{m\neq n} \psi_m(\mathbf{r})\frac{\langle\psi_m|\,\Delta V_{\mathrm{SCF}}\,|\psi_n\rangle}{\varepsilon_n - \varepsilon_m}, \tag{4.20}$$

are obtained by projecting both sides of Eq. (4.18) onto $\langle\psi_m|$ [19]. Furthermore, the first-order correction to the self-consistent Kohn-Sham potential can be written as

$$\Delta V_{\mathrm{SCF}}(\mathbf{r}) = \Delta V_{\text{e-n}}(\mathbf{r}) + \int \frac{\Delta n(\mathbf{r}')}{|\mathbf{r}-\mathbf{r}'|}\,d\mathbf{r}' + \left.\frac{dV_{\mathrm{xc}}(n)}{dn}\right|_{n=n(\mathbf{r})} \Delta n(\mathbf{r}). \tag{4.21}$$

Eqs. (4.17) to (4.21) form a set of self-consistent equations which can be solved iteratively. This is because $\Delta V_{\mathrm{SCF}}(\mathbf{r})$ is a functional of $\Delta n(\mathbf{r})$, which depends linearly on the first-order corrections $\Delta\psi_n(\mathbf{r})$ to the Kohn-Sham orbitals. These, in turn, are calculated from $\Delta V_{\mathrm{SCF}}(\mathbf{r})$, thereby closing the self-consistent cycle [19, 27].

A key insight for calculating the responses $\Delta\psi_n(\mathbf{r})$ can be gained from plugging Eq. (4.19) into Eq. (4.17) resulting in

$$\Delta n(\mathbf{r}) = 4\sum_{n}^{N/2}\sum_{m\neq n} \psi_n^*(\mathbf{r})\psi_m(\mathbf{r})\frac{\langle\psi_m|\,\Delta V_{\mathrm{SCF}}\,|\psi_n\rangle}{\varepsilon_n - \varepsilon_m}. \tag{4.22}$$

For each term with $m \leq N/2$, meaning m lies within the valence bands, the sum contains a corresponding term with the indices m and n swapped. Since Kohn-Sham orbitals are real-valued and ΔV_{SCF} is Hermitian, the elements of such pairs have the same modulus but opposite signs and therefore cancel. Thus, the index m can start from the unoccupied orbitals and $n(\mathbf{r})$ only responds to those parts of the perturbation that couple the occupied-state manifold to the unoccupied-state manifold. Consequently, $|\Delta\psi_n\rangle$ are only composed of states from the conduction bands, indexed by c, such that the

unoccupied-state manifold's projector $\hat{P}_{\{c\}}$ can be applied to both sides of Eq. (4.18), yielding

$$(\hat{H}_{\mathrm{SCF}} - \varepsilon_n)\,|\Delta\psi_n\rangle = -\hat{P}_{\{c\}}\,\Delta V_{\mathrm{SCF}}\,|\psi_n\rangle\,, \tag{4.23}$$

as explained in Ref. [19]. This step makes the operator on the left-hand side non-singular. Eq. (4.23) requires only the knowledge of the occupied states and allows an iterative calculation of $|\Delta\psi_n\rangle$, avoiding the extensive summation over the full spectrum of $\hat{H}_{\mathrm{SCF}}$ as done in Eqs. (4.19) and (4.22). The responses $|\Delta\psi_n\rangle$ can then be found using numerical methods like the conjugate-gradient method to solve Eqs. (4.23). In case an initial trial solution $|\Delta\psi_n\rangle$ contains components from the occupied-state manifold, the term $\gamma\hat{P}_{\{v\}}$, with scaling factor γ and projector $\hat{P}_{\{v\}} = 1 - \hat{P}_{\{c\}}$, has to be added to the left-hand side's operator in order to keep it non-singular and enhance numerical stability [19, pp. 5–6].

4.3.3. Interatomic Force Constants

The calculation of interatomic force constants $C_{\kappa\alpha,\kappa'\alpha'}(\mathbf{q})$ is a prototypical application of the DFPT self-consistent procedure. The perturbations can be chosen such that DFPT can be applied without relying on supercells, such that smaller $\mathbf{q}$-vectors do not cause an increasing computational effort. This can be achieved by using monochromatic displacement patterns of the form

$$\Delta\tau_{\kappa\alpha p}(\mathbf{q}) = u_{\kappa\alpha}(\mathbf{q})\, e^{i\mathbf{q}\cdot\mathbf{R}_p}, \tag{4.24}$$

each introducing a modulated displacement of nucleus κ in Cartesian direction α across all unit cells [19, p. 13]. The interatomic force constants in Fourier space can then be expressed in terms of derivatives with respect to the monochromatic displacement patterns as

$$C_{\kappa\alpha,\kappa'\alpha'}(\mathbf{q}) = \sum_{\mathbf{R_n}} e^{i\mathbf{q}\cdot\mathbf{R_n}} C_{\kappa\alpha,\kappa'\alpha'}(\mathbf{R_n}) = \frac{1}{N_p}\frac{\partial^2 U}{\partial u^*_{\kappa\alpha}(\mathbf{q})\partial u_{\kappa'\alpha'}(\mathbf{q})}. \tag{4.25}$$

Due to the linearity of the Fourier transform, $C_{\kappa\alpha,\kappa'\alpha'}(\mathbf{q})$ inherits the structure of an electronic and an ionic contribution from the BO potential, such that

$$C_{\kappa\alpha,\kappa'\alpha'}(\mathbf{q}) = C^{\mathrm{el}}_{\kappa\alpha,\kappa'\alpha'}(\mathbf{q}) + C^{\mathrm{ion}}_{\kappa\alpha,\kappa'\alpha'}(\mathbf{q}). \tag{4.26}$$

After calculating $C_{\kappa\alpha,\kappa'\alpha'}(\mathbf{q})$, the real-space force constants $C_{\kappa\alpha,\kappa'\alpha'}(\mathbf{R}_p)$ can be readily obtained via inverse Fourier transform [19, p. 13].

Electronic Part

The calculation of the electronic part, as explained in Ref. [19, p. 7, p. 13], can be performed by applying the concept of monochromatic displacement patterns to Eq. (4.15), yielding

$$C^{\mathrm{el}}_{\kappa\alpha,\kappa'\alpha'}(\mathbf{q}) = \frac{1}{N_p}\left[\int d\mathbf{r}\, n(\mathbf{r}) \frac{\partial^2 V^{\mathrm{ps}}_{\text{e-n}}(\mathbf{r})}{\partial u^*_{\kappa\alpha}(\mathbf{q}) \partial u_{\kappa'\alpha'}(\mathbf{q})} + \int d\mathbf{r} \left(\frac{\partial n(\mathbf{r})}{\partial u_{\kappa\alpha}(\mathbf{q})}\right)^* \frac{\partial V^{\mathrm{ps}}_{\text{e-n}}(\mathbf{r})}{\partial u_{\kappa'\alpha'}(\mathbf{q})}\right], \quad (4.27)$$

where

$$\frac{\partial V^{\mathrm{ps}}_{\text{e-n}}(\mathbf{r})}{\partial u_{\kappa\alpha}(\mathbf{q})} = -\sum_p \frac{\partial v^{\mathrm{ps}}_{\kappa}(\mathbf{r} - \boldsymbol{\tau}^0_{\kappa p})}{\partial r_\alpha} e^{i\mathbf{q}\cdot\mathbf{R}_p}. \quad (4.28)$$

For calculating the response $\partial n(\mathbf{r})/\partial u_{\kappa\alpha}(\mathbf{q})$, monochromatic displacements of the form $u_{\kappa\alpha}(\mathbf{q})\, e^{i\mathbf{q}\cdot\mathbf{R}_p}$ can be employed. These lead to a perturbative potential of the form

$$\Delta V^{\kappa\alpha,\mathbf{q}}_{\mathrm{SCF}}(\mathbf{r}) = \Delta v^{\kappa\alpha,\mathbf{q}}_{\mathrm{SCF}}(\mathbf{r})\, e^{i\mathbf{q}\cdot\mathbf{r}}, \quad (4.29)$$

consisting of only one Fourier component, which is a lattice periodic function $\Delta v^{\kappa\alpha,\mathbf{q}}_{\mathrm{SCF}}(\mathbf{r})$. Furthermore, the matrix elements

$$\langle \psi_{c\mathbf{k}'} |\, \Delta v^{\kappa\alpha,\mathbf{q}}_{\mathrm{SCF}}(\mathbf{r})\, e^{i\mathbf{q}\cdot\mathbf{r}}\, | \psi_{v\mathbf{k}} \rangle = \langle u_{c\mathbf{k}'} |\, \Delta v^{\kappa\alpha,\mathbf{q}}_{\mathrm{SCF}}(\mathbf{r})\, e^{i(\mathbf{q}+\mathbf{k}-\mathbf{k}')\cdot\mathbf{r}}\, | u_{v\mathbf{k}} \rangle \quad (4.30)$$

appearing in Eqs. (4.19) and (4.22) are non-zero only if

$$\mathbf{k}' = \mathbf{q} + \mathbf{k} - \mathbf{G}. \quad (4.31)$$

This implies that the response in $|\psi_{v\mathbf{k}}\rangle$ has contributions exclusively from the conduction-band states $|\psi_{c\mathbf{k}+\mathbf{q}}\rangle$. Consequently, the projector $\hat{P}_{\mathbf{k}+\mathbf{q}}$ can be applied to Eq. (4.23), leading to

$$(\hat{H}^{\mathbf{k}+\mathbf{q}}_{\mathrm{SCF}} + \gamma \hat{P}_{\{v\}\mathbf{k}+\mathbf{q}} - \varepsilon^{\mathbf{k}}_v)\, |\Delta u_{v\mathbf{k}+\mathbf{q}}\rangle = -\hat{P}_{\{c\}\mathbf{k}+\mathbf{q}}\, \Delta v^{\kappa\alpha,\mathbf{q}}_{\mathrm{SCF}}\, |u_{v\mathbf{k}}\rangle\,, \quad (4.32)$$

as explained in Ref. [19, p. 7, p. 13]. Eqs. (4.17) and (4.21), which are involved in the self-consistent cycle for calculating the responses $\Delta n(\mathbf{r})$ and $\Delta V_{\mathrm{SCF}}(\mathbf{r})$, respectively, can be adjusted analogously, yielding

$$\Delta n^{\kappa\alpha,\mathbf{q}}(\mathbf{r}) = 4 \sum_{v\mathbf{k}}^{N/2} u^*_{v\mathbf{k}}(\mathbf{r})\, \Delta u_{v\mathbf{k}+\mathbf{q}}(\mathbf{r}) \quad (4.33)$$

and

$$\Delta v^{\kappa\alpha,\mathbf{q}}_{\mathrm{SCF}}(\mathbf{r}) = \Delta v^{\kappa\alpha,\mathbf{q}}_{\text{e-n}}(\mathbf{r}) + \int \frac{\Delta n^{\kappa\alpha,\mathbf{q}}(\mathbf{r}')}{|\mathbf{r}-\mathbf{r}'|} e^{-i\mathbf{q}\cdot(\mathbf{r}-\mathbf{r}')}\, d\mathbf{r}' + \left.\frac{dV_{\mathrm{xc}}(n)}{dn}\right|_{n=n(\mathbf{r})} \Delta n^{\kappa\alpha,\mathbf{q}}(\mathbf{r}). \quad (4.34)$$

Eqs. (4.32) to (4.34) form a self-consistent set of equations, parameterized by a $\mathbf{q}$-vector from the 1st BZ, a nucleus κ, and a Cartesian direction α. Sets of self-consistent DFPT equations for different parameterizations are independent of each other [19, p. 7, p. 13].

Besides the response of the electron density $\Delta n^{\kappa\alpha,\mathbf{q}}(\mathbf{r})$, required in Eq. (4.27), the DFPT self-consistent procedure also yields the corresponding derivative of the self-consistent-field potential to the applied monochromatic perturbation:

$$\partial_{\kappa\alpha,\mathbf{q}} v_{\mathrm{SCF}}(\mathbf{r}) \approx \frac{\Delta v_{\mathrm{SCF}}^{\kappa\alpha,\mathbf{q}}(\mathbf{r})}{u_{\kappa\alpha}(\mathbf{q})}. \tag{4.35}$$

These derivatives are essential quantities for calculating the total response of the self-consistent-field potential due to phonon mode $\mathbf{q}\nu$, defined in Eq. (3.66) [19, p. 7, p. 13].

Ionic Part

The ionic part $C^{\mathrm{ion}}_{\kappa\alpha,\kappa'\alpha'}(\mathbf{q})$ is the second-order derivative of the electrostatic interaction energy $V_{\text{n-n}}(\{\boldsymbol{\tau}_J\})$ between the ionic effective charges. The pair-interaction terms of $V_{\text{n-n}}(\{\boldsymbol{\tau}_J\})$ decay with $|\boldsymbol{\tau}_I - \boldsymbol{\tau}_J|^{-1}$, causing the second-order derivatives to fall off like $|\boldsymbol{\tau}_I - \boldsymbol{\tau}_J|^{-3}$. Despite the rapid decay, the energy contribution from a single unit cell diverges within the supercell as $N_p \to \infty$ or under periodic boundary conditions. To properly handle this long-range interaction, the technique of Ewald summation is applied [19, pp. 13, 48].

In polar materials, the long-range character of Coulomb forces leads to macroscopic electric fields due to dipoles generated by nuclear displacements. These electric fields couple to LO phonons in the long-wavelength limit and are breaking lattice periodicity. They have to be considered in the calculation of $C^{\mathrm{ion}}_{\kappa\alpha,\kappa'\alpha'}(\mathbf{q})$, using the concept of Born-effective-charges [19, pp. 13, 48].

Chapter 5

Ab initio Theory of Polarons

Chapters 3 and 4 introduced all necessary concepts for tackling the polaron problem with DFT-based methods, as presented in Ref. [9]. The following derivation assumes an insulating material with completely filled valence bands v, using a Born-von-Kármán supercell with lattice vector $\mathbf{T}$, a volume Ω, and N_p unit cells. The BO energy surface, consisting of the total DFT energy and the nuclear potential energy $V_{\text{n-n}}(\{\boldsymbol{\tau}_I\})$, is then given by

$$\begin{aligned} E[\{\psi_{v\mathbf{k}}\},\{\boldsymbol{\tau}_{\kappa p}\}] = &-2\sum_{v\mathbf{k}}\int d\mathbf{r}\,\psi^*_{v\mathbf{k}}(\mathbf{r})\frac{\boldsymbol{\nabla}^2}{2}\psi_{v\mathbf{k}}(\mathbf{r}) \\ &+\frac{1}{2}\sum_{\mathbf{T}}\iint d\mathbf{r}d\mathbf{r}'\,\frac{n(\mathbf{r})n(\mathbf{r}')}{|\mathbf{r}-\mathbf{r}'-\mathbf{T}|} \\ &+E_{\text{xc}}\left[n^{\uparrow},n^{\downarrow}\right] \\ &-\sum_{\kappa p}\sum_{\mathbf{T}}\int d\mathbf{r}\,\frac{Z_\kappa n(\mathbf{r})}{|\mathbf{r}-\boldsymbol{\tau}_{\kappa p}-\mathbf{T}|} \\ &+\frac{1}{2}\sum_{\substack{\kappa p\\ \kappa' p'}}\sum_{\mathbf{T}}\frac{Z_\kappa Z_{\kappa'}}{|\boldsymbol{\tau}_{\kappa p}-\boldsymbol{\tau}_{\kappa' p'}-\mathbf{T}|}. \end{aligned} \tag{5.1}$$

The integrals in Eq. (5.1) are evaluated, and the Kohn-Sham orbitals $\psi_{v\mathbf{k}}(\mathbf{r})$ are normalized within the Born-von-Kármán supercell. The summation in the last term implicitly skips contributions having $\kappa p = \kappa' p'$ for $\mathbf{T} = 0$, to avoid zero denominators [9].

Adding one electron on top of the ground-state makes the system spin-polarized, and describing the excess charge carrier as $\psi(\mathbf{r})$ changes the electron density by $\Delta n(\mathbf{r}) = |\psi(\mathbf{r})|^2$. Defining that the spin polarization is spin-up and adding a constant jellium background

$(N_p\Omega)^{-1}$ to avoid Coulomb divergence leads to the total energy expression

$$
\begin{aligned}
E[\psi,\{\psi_{v\mathbf{k}}\},\{\boldsymbol{\tau}_{\kappa p}\}] &= -2\sum_{v\mathbf{k}}\int d\mathbf{r}\,\psi^*_{v\mathbf{k}}(\mathbf{r})\frac{\boldsymbol{\nabla}^2}{2}\psi_{v\mathbf{k}}(\mathbf{r}) - \int d\mathbf{r}\,\psi^*(\mathbf{r})\frac{\boldsymbol{\nabla}^2}{2}\psi(\mathbf{r}) \\
&+ \frac{1}{2}\sum_{\mathbf{T}}\iint d\mathbf{r}d\mathbf{r}'\,\frac{\left[n(\mathbf{r})+\Delta n(\mathbf{r})-(N_p\Omega)^{-1}\right]\left[n(\mathbf{r}')+\Delta n(\mathbf{r}')-(N_p\Omega)^{-1}\right]}{|\mathbf{r}-\mathbf{r}'-\mathbf{T}|} \\
&+ E_{\mathrm{xc}}\left[n^{\uparrow}+\Delta n, n^{\downarrow}\right] \\
&- \sum_{\kappa p}\sum_{\mathbf{T}}\int d\mathbf{r}\,\frac{Z_\kappa\left[n(\mathbf{r})+\Delta n(\mathbf{r})-(N_p\Omega)^{-1}\right]}{|\mathbf{r}-\boldsymbol{\tau}_{\kappa p}-\mathbf{T}|} \\
&+ \frac{1}{2}\sum_{\substack{\kappa p\\ \kappa' p'}}\sum_{\mathbf{T}}\frac{Z_\kappa Z_{\kappa'}}{\left|\boldsymbol{\tau}_{\kappa p}-\boldsymbol{\tau}_{\kappa' p'}-\mathbf{T}\right|},
\end{aligned}
\tag{5.2}
$$

as explained in Ref. [9]. For a small polaron, the change in electron density is at most of order Ω^{-1} in the hosting unit cell and almost zero everywhere else. For a large polaron, the density change is more spread out and of order $(N_p\Omega)^{-1}$. Therefore, the change in $\Delta n(\mathbf{r})$ can be considered much smaller than $n(\mathbf{r})$ almost everywhere, justifying the expansion of the exchange-correlation energy around $\Delta n(\mathbf{r})=0$ as

$$
\begin{aligned}
E_{\mathrm{xc}}\left[n^{\uparrow}+\Delta n, n^{\downarrow}\right] &= E_{\mathrm{xc}}\left[n^{\uparrow}, n^{\downarrow}\right] \\
&+ \int d\mathbf{r}\,\frac{\delta E_{\mathrm{xc}}}{\delta n^{\uparrow}}\Delta n(\mathbf{r}) \\
&+ \frac{1}{2}\iint d\mathbf{r}d\mathbf{r}'\,\frac{\delta E_{\mathrm{xc}}}{\delta n^{\uparrow}\delta n^{\uparrow}}\Delta n(\mathbf{r})\Delta n(\mathbf{r}') + \mathcal{O}(\Delta n^3),
\end{aligned}
\tag{5.3}
$$

while keeping the valence states $\psi_{v\mathbf{k}}(\mathbf{r})$ unchanged [9].

Expanding the integrands of Eq. (5.2) and using the second-order approximation of $E_{\mathrm{xc}}\left[n^{\uparrow}+\Delta n, n^{\downarrow}\right]$ from Eq. (5.3) allows a regrouping of expressions in order to recover

$E[\{\psi_{v\mathbf{k}}\},\{\boldsymbol{\tau}_{\kappa p}\}]$ and $\hat{H}_{\mathrm{KS}}[n(\mathbf{r}),\{\boldsymbol{\tau}_{\kappa p}\}]$, such that

$$
\begin{aligned}
&E[\psi,\{\psi_{v\mathbf{k}}\},\{\boldsymbol{\tau}_{\kappa p}\}] = E[\{\psi_{v\mathbf{k}}\},\{\boldsymbol{\tau}_{\kappa p}\}] \\
&+ \int d\mathbf{r}\,\psi^*(\mathbf{r}) \underbrace{\left[-\frac{\boldsymbol{\nabla}^2}{2} + \sum_{\mathbf{T}}\int d\mathbf{r}'\,\frac{n(\mathbf{r}')}{|\mathbf{r}-\mathbf{r}'-\mathbf{T}|} - \sum_{\kappa p,\mathbf{T}}\frac{Z_\kappa}{|\mathbf{r}-\boldsymbol{\tau}_{\kappa p}-\mathbf{T}|} + \frac{\delta E_{\mathrm{xc}}}{\delta n^\uparrow}\right]}_{\hat{H}_{\mathrm{KS}}[n(\mathbf{r}),\{\boldsymbol{\tau}_{\kappa p}\}]}\psi(\mathbf{r}) \\
&+ \frac{1}{2}\iint d\mathbf{r}d\mathbf{r}'\,\frac{\delta^2 E_{\mathrm{xc}}}{\delta n^\uparrow \delta n^\uparrow}\Delta n(\mathbf{r})\Delta n(\mathbf{r}') + \mathcal{O}(\Delta n^3) \\
&+ \frac{1}{2}\sum_{\mathbf{T}}\iint d\mathbf{r}d\mathbf{r}'\,\frac{\left[\Delta n(\mathbf{r}) - (N_p\Omega)^{-1}\right]\left[\Delta n(\mathbf{r}') - (N_p\Omega)^{-1}\right]}{|\mathbf{r}-\mathbf{r}'-\mathbf{T}|} \\
&+ \underbrace{\sum_{\mathbf{T}}\iint d\mathbf{r}d\mathbf{r}'\,\frac{1}{N_p\Omega}\frac{-n(\mathbf{r})}{|\mathbf{r}-\mathbf{r}'-\mathbf{T}|}}_{E_{\mathrm{B}}}\,.
\end{aligned}
\tag{5.4}
$$

Similarly, the BO energy surface can be expanded around equilibrium positions $\boldsymbol{\tau}^0_{\kappa p}$ in terms of displacements $\Delta\boldsymbol{\tau}_{\kappa p}$. This yields the harmonic approximation

$$
E[\{\psi_{v\mathbf{k}}\},\{\boldsymbol{\tau}_{\kappa p}\}] = E\left[\{\psi^0_{v\mathbf{k}}\},\{\boldsymbol{\tau}^0_{\kappa p}\}\right] + \frac{1}{2}\sum_{\substack{\kappa\alpha p\\ \kappa'\alpha' p'}} C^0_{p\alpha\kappa,p'\alpha'\kappa'}\Delta\tau_{\kappa\alpha p}\Delta\tau_{\kappa'\alpha' p'} + \mathcal{O}(\Delta\boldsymbol{\tau}^3), \tag{5.5}
$$

with Kohn-Sham orbitals $\psi^0_{v\mathbf{k}}$ and interatomic force constants $C^0_{p\alpha\kappa,p'\alpha'\kappa'}$ obtained at the nuclei's equilibrium positions $\boldsymbol{\tau}^0_{\kappa p}$ [9].

Altogether, approximating the total energy up to second order in $\Delta\boldsymbol{\tau}_{\kappa p}$ and $\Delta n(\mathbf{r})$ gives

$$
\begin{aligned}
E[\psi,\{\psi_{v\mathbf{k}}\},\{\boldsymbol{\tau}_{\kappa p}\}] &= E\left[\{\psi^0_{v\mathbf{k}}\},\{\boldsymbol{\tau}^0_{\kappa p}\}\right] + \frac{1}{2}\sum_{\substack{\kappa\alpha p\\ \kappa'\alpha' p'}} C^0_{p\alpha\kappa,p'\alpha'\kappa'}\Delta\tau_{\kappa\alpha p}\Delta\tau_{\kappa'\alpha' p'} \\
&+ \int d\mathbf{r}\,\psi^*(\mathbf{r})\hat{H}_{\mathrm{KS}}[n(\mathbf{r}),\{\boldsymbol{\tau}_{\kappa p}\}]\,\psi(\mathbf{r}) \\
&+ \frac{1}{2}\iint d\mathbf{r}d\mathbf{r}'\,\frac{\delta^2 E_{\mathrm{xc}}}{\delta n^\uparrow \delta n^\uparrow}\Delta n(\mathbf{r})\Delta n(\mathbf{r}') \\
&+ \frac{1}{2}\sum_{\mathbf{T}}\iint d\mathbf{r}d\mathbf{r}'\,\frac{\left[\Delta n(\mathbf{r}) - (N_p\Omega)^{-1}\right]\left[\Delta n(\mathbf{r}') - (N_p\Omega)^{-1}\right]}{|\mathbf{r}-\mathbf{r}'-\mathbf{T}|} \\
&+ E_{\mathrm{B}} + \mathcal{O}(\Delta n^3) + \mathcal{O}(\Delta\boldsymbol{\tau}^3),
\end{aligned}
\tag{5.6}
$$

which can be simplified further [9]. Anticipating that $\psi(\mathbf{r})$ and $\Delta\tau_{\kappa\alpha p}$ must be found through minimizing $E[\psi, \{\psi_{v\mathbf{k}}\}, \{\boldsymbol{\tau}_{\kappa p}\}]$, the constant terms E_B and $E\big[\{\psi^0_{v\mathbf{k}}\}, \{\boldsymbol{\tau}^0_{\kappa p}\}\big]$ can be dropped for further considerations. The two double-integral terms of Eq. (5.6) are DFT artifacts accounting for a self-interaction of the excess charge, which is unwarranted by a more accurate many-body picture. These terms would completely prohibit a localized solution for $\psi(\mathbf{r})$. However, it turns out that these DFT artifacts drop out exactly when employing a self-interaction-corrected DFT functional, as described in Ref. [9, SEC. IV], justifying their removal. Furthermore, the Kohn-Sham Hamiltonian $\hat{H}_\mathrm{KS}[n(\mathbf{r}), \{\boldsymbol{\tau}_{\kappa p}\}]$, describing the former system without the excess electron, can be expressed via Taylor expansion around the nuclei's equilibrium positions $\boldsymbol{\tau}^0_{\kappa p}$, up to first order, being the lowest-order approximation permitting localized solutions for $\psi(\mathbf{r})$ [9]. All these considerations finally lead to the DFT polaron energy functional

$$E_\mathrm{p}[\psi, \{\Delta\tau_{\kappa\alpha p}\}] = \int d\mathbf{r}\, \psi^*(\mathbf{r}) \left[\underbrace{\hat{H}_\mathrm{SCF}\big[n^0(\mathbf{r}), \{\boldsymbol{\tau}^0_{\kappa p}\}\big]}_{\hat{H}^0_\mathrm{SCF}} + \sum_{\kappa\alpha p} \frac{\partial V^0_\mathrm{SCF}(\mathbf{r})}{\partial \tau_{\kappa\alpha p}} \Delta\tau_{\kappa\alpha p} \right] \psi(\mathbf{r}) + \frac{1}{2} \sum_{\substack{\kappa\alpha p \\ \kappa'\alpha' p'}} C^0_{p\alpha\kappa, p'\alpha'\kappa'} \Delta\tau_{\kappa\alpha p} \Delta\tau_{\kappa'\alpha' p'}, \tag{5.7}$$

as derived in Ref. [9].

The polaron wave function $\psi(\mathbf{r})$ together with the corresponding atomic displacements $\Delta\boldsymbol{\tau}_{\kappa p}$ have to be found through minimizing $E_\mathrm{p}[\psi, \{\Delta\tau_{\kappa\alpha p}\}]$. In analogy to the approach employed in the LP model, the normalization condition for the polaron wave function $\psi(\mathbf{r})$ enters as a Lagrange multiplier ε, such that the minimization condition with respect to $\psi(\mathbf{r})$ reads

$$\frac{\delta}{\delta\psi^*} \left[E_\mathrm{p}[\psi, \{\Delta\tau_{\kappa\alpha p}\}] - \varepsilon \left(\int d\mathbf{r}\, |\psi(\mathbf{r})|^2 - 1 \right) \right] = 0, \tag{5.8}$$

and yields the eigenvalue equation

$$\left[\hat{H}^0_\mathrm{SCF} + \sum_{\kappa\alpha p} \frac{\partial V^0_{SCF}(\mathbf{r})}{\partial \tau_{\kappa\alpha p}} \Delta\tau_{\kappa\alpha p} \right] \psi(\mathbf{r}) = \varepsilon\, \psi(\mathbf{r}), \tag{5.9}$$

as shown in [9]. The minimization with respect to the displacements requires

$$\frac{\delta E_\mathrm{p}[\psi, \{\Delta\tau_{\kappa\alpha p}\}]}{\delta \Delta\tau_{\kappa\alpha p}} = 0 \tag{5.10}$$

to hold, and yields

$$\Delta\tau_{\kappa\alpha p} = -\sum_{\kappa'\alpha' p'} (C^0)^{-1}_{\kappa\alpha p, \kappa'\alpha' p'} \int d\mathbf{r}\, \frac{\partial V^0_\mathrm{SCF}(\mathbf{r})}{\partial \tau_{\kappa'\alpha' p'}} |\psi(\mathbf{r})|^2 \tag{5.11}$$

for the displacements associated with the polaron wave function $\psi(\mathbf{r})$. Eqs. (5.9) and (5.11) together form a set of self-consistent equations for the polaron wave function $\psi(\mathbf{r})$ and the associated set of displacements $\Delta\tau_{\kappa\alpha p}$ [9].

The inversion of the force constants matrix $C^0_{\kappa\alpha p,\kappa'\alpha' p'}$ can be efficiently performed in the eigenbasis of each $\mathbf{q}$-dependent dynamical matrix by utilizing $\mathrm{diag}\big[\{\omega^2_{\mathbf{q}\nu}\}\big]^{-1} = \mathrm{diag}\big[\{\omega^{-2}_{\mathbf{q}\nu}\}\big]$. The vibrational normal modes $\mathbf{e}_{\kappa,\nu}(\mathbf{q})$ are used to transform the inverted dynamical matrices from their eigenbasis into Cartesian based matrices $(D^0)^{-1}_{\kappa\alpha,\kappa'\alpha'}(\mathbf{q})$. These are then combined to the inverted force constants matrix:

$$(C^0)^{-1}_{\kappa\alpha p,\kappa'\alpha' p'} = \frac{1}{N_p}\sum_{\mathbf{q}\nu}\frac{e_{\kappa\alpha,\nu}(\mathbf{q})e^*_{\kappa'\alpha',\nu}(\mathbf{q})}{\omega^2_{\mathbf{q}\nu}\sqrt{M_\kappa M_{\kappa'}}}e^{i\mathbf{q}\cdot(\mathbf{R}_p-\mathbf{R}_{p'})}, \tag{5.12}$$

using Fourier transform and removing of the mass weightings [9].

Substituting Eq. (5.11) into Eq. (5.9) leads to the eigenvalue equation

$$\left[\hat{H}^0_{\mathrm{SCF}} - \int d\mathbf{r}'\, K^0(\mathbf{r},\mathbf{r}')\big|\psi(\mathbf{r}')\big|^2\right]\psi(\mathbf{r}) = \varepsilon\,\psi(\mathbf{r}), \tag{5.13}$$

with

$$K^0(\mathbf{r},\mathbf{r}') = \sum_{\substack{\kappa\alpha p\\ \kappa'\alpha' p'}}\frac{\partial V^0_{\mathrm{SCF}}(\mathbf{r})}{\partial\tau_{\kappa\alpha p}}(C^0)^{-1}_{p\alpha\kappa,p'\alpha'\kappa'}\frac{\partial V^0_{\mathrm{SCF}}(\mathbf{r}')}{\partial\tau_{\kappa'\alpha' p'}}, \tag{5.14}$$

revealing a strong similarity to the eigenvalue problem of the LP model in Eq. (2.10). In comparison to Eq. (2.10), Eq. (5.13) features the Kohn-Sham Hamiltonian $\hat{H}^0_{\mathrm{SCF}}$ and the polaron kernel $K^0(\mathbf{r},\mathbf{r}')$ in the role of the kinetic energy and the kernel $|\mathbf{r}-\mathbf{r}'|^{-1}$, respectively [9, 10].

5.1. Polaron Formation Energy

The polaron formation energy is defined as

$$\Delta E_f = \min E_{\mathrm{p}}[\psi,\{\Delta\tau_{\kappa\alpha p}\}] - \min E_{\mathrm{p}}[\psi,\{\Delta\tau_{\kappa\alpha p}=0\}], \tag{5.15}$$

which is the energy difference between two possible scenarios:

1. The excess electron is locally trapped in its self-generated lattice distortion.

2. The excess electron occupies the bottom Kohn-Sham state of the conduction band, without causing any lattice distortion [9].

Substituting Eq. (5.7) into Eq. (5.15) and using Eq. (5.11) for the displacements $\Delta\tau_{\kappa\alpha p}$, along with the definition of the kernel $K^0(\mathbf{r},\mathbf{r}')$ from Eq. (5.11), results in

$$\Delta E_f = \int d\mathbf{r}\, \psi^*(\mathbf{r}) \left[\hat{H}^0_{\mathrm{SCF}} - \varepsilon_{\mathrm{CBM}}\right] \psi(\mathbf{r}) - \frac{1}{2} \iint d\mathbf{r} d\mathbf{r}'\, |\psi(\mathbf{r})|^2 K^0(\mathbf{r},\mathbf{r}') |\psi(\mathbf{r})|^2, \quad (5.16)$$

where $\varepsilon_{\mathrm{CBM}}$ is the Kohn-Sham eigenvalue of the lowest-energy conduction-band state [9]. The eigenvalues ε and $\varepsilon_{\mathrm{CBM}}$ can be expressed by projecting Eq. (5.13) onto $\psi^*(\mathbf{r})$ and subtracting $\varepsilon_{\mathrm{CBM}}$ from ε yields

$$\varepsilon - \varepsilon_{\mathrm{CBM}} = \int d\mathbf{r}\, \psi^*(\mathbf{r}) \left[\hat{H}^0_{\mathrm{SCF}} - \varepsilon_{\mathrm{CBM}}\right] \psi(\mathbf{r}) - \iint d\mathbf{r} d\mathbf{r}'\, |\psi(\mathbf{r})|^2 K^0(\mathbf{r},\mathbf{r}') |\psi(\mathbf{r})|^2. \quad (5.17)$$

The respective first terms of Eqs. (5.16) and (5.17) are equal, so that subtracting them eliminates their first term and finally leads to the compact expression

$$\Delta E_f = \varepsilon - \varepsilon_{\mathrm{CBM}} + \frac{1}{2} \iint d\mathbf{r} d\mathbf{r}'\, |\psi(\mathbf{r})|^2 K^0(\mathbf{r},\mathbf{r}') |\psi(\mathbf{r})|^2. \quad (5.18)$$

With the help of Eq. (5.14), the formation energy from Eq. (5.18) can also be reformulated as

$$\Delta E_f = \underbrace{\varepsilon - \varepsilon_{\mathrm{CBM}}}_{\text{electron part}} + \underbrace{\frac{1}{2} \sum_{\substack{\kappa\alpha p \\ \kappa'\alpha' p'}} C^0_{p\alpha\kappa,p'\alpha'\kappa'} \Delta\tau_{\kappa\alpha p} \Delta\tau_{\kappa'\alpha' p'}}_{\text{phonon part}}. \quad (5.19)$$

In case $\Delta E_f < 0$, a localized polaron wave function $\psi(\mathbf{r})$ and its associated lattice distortion account for a lower energy, compared to $\psi(\mathbf{r})$ being a conduction-band electron with no associated atomic displacements [9].

Eq. (5.19) can also be understood using the Franck-Condon principle: The difference $\varepsilon_{\mathrm{CBM}} - \varepsilon$ is the electron part of the formation energy and represents the energy required to lift the self-trapped electron from its localized polaron state $\psi(\mathbf{r})$ into the lowest conduction-band state, while keeping the lattice distortion intact. In this picture, the third term of Eq. (5.19)—the phonon part—represents the potential energy stored in the lattice distortion, which is then released during that process [9].

5.2. Polaron Equations in the Kohn-Sham Basis

The equilibrium Kohn-Sham orbitals form a complete basis of the Hilbert space. Therefore, it is reasonable to write the polaron wave function as

$$\psi(\mathbf{r}) = \frac{1}{\sqrt{N_p}} \sum_{n\mathbf{k}} A_{n\mathbf{k}} \psi_{n\mathbf{k}}(\mathbf{r}), \quad (5.20)$$

a linear combination of unoccupied conduction-band Kohn-Sham orbitals in Bloch representation. This follows from the assumption of an unmodified valence-band manifold when adding an excess charge on top of it. From the normalization condition for $\psi(\mathbf{r})$ and from the fact that the Kohn-Sham states are an orthonormal system, the condition

$$\frac{1}{N_p}\sum_{n\mathbf{k}} |A_{n\mathbf{k}}|^2 = 1 \tag{5.21}$$

arises for the coefficients $A_{n\mathbf{k}}$ [9].

For writing the polaron eigenvalue problem in the basis of Kohn-Sham states, the *Ansatz* from Eq. (5.20) is substituted into Eq. (5.13) before projecting the resulting equation onto $\psi^*_{n\mathbf{k}}(\mathbf{r})$. Additionally, using the expressions for $K^0(\mathbf{r},\mathbf{r}')$, $(C^0)^{-1}_{\kappa\alpha p,\kappa'\alpha' p'}$, and $g_{mn\nu}(\mathbf{k},\mathbf{q})$ from Eqs. (5.14), (5.12), and (3.65), respectively, one arrives at

$$\frac{2}{N_p}\sum_{\mathbf{q}m\nu} B_{\mathbf{q}\nu}\, g^*_{mn\nu}(\mathbf{k},\mathbf{q}) A_{m\mathbf{k}+\mathbf{q}} = (\varepsilon_{n\mathbf{k}} - \varepsilon) A_{n\mathbf{k}}, \tag{5.22}$$

with

$$B_{\mathbf{q}\nu} = \frac{1}{N_p}\sum_{mn\mathbf{k}} A^*_{m\mathbf{k}+\mathbf{q}} \frac{g_{mn\nu}(\mathbf{k},\mathbf{q})}{\hbar\omega_{\mathbf{q}\nu}} A_{n\mathbf{k}}. \tag{5.23}$$

Eqs. (5.22) and (5.23) constitute a self-consistent eigenvalue problem for the polaron wave function in the Kohn-Sham basis, solely based on quantities obtainable from DFT and DFPT ground-state calculations in a unit cell [9]. Rewriting Eq. (5.22) to

$$\sum_{n'\mathbf{k}'} H_{n\mathbf{k},n'\mathbf{k}'} A_{n'\mathbf{k}'} = \varepsilon A_{n\mathbf{k}}, \tag{5.24}$$

with

$$H_{n\mathbf{k},n'\mathbf{k}'} = \delta_{n\mathbf{k},n'\mathbf{k}'}\varepsilon_{n\mathbf{k}} - \frac{2}{N_p}\sum_{\nu} B^*_{\mathbf{k}-\mathbf{k}'\nu}\, g_{nn'\nu}(\mathbf{k}',\mathbf{k}-\mathbf{k}'), \tag{5.25}$$

adds more clarity to the structure of the self-consistent problem. In practice, Eqs. (5.24), (5.25), and (5.23) can be solved using a parallel steepest descent algorithm with a Gaussian line-shape as the starting point for the polaron vector $A_{n\mathbf{k}}$ [9].

To find an expression for the atomic displacements $\Delta\tau_{\kappa\alpha p}$ in terms of the polaron eigenvector $A_{n\mathbf{k}}$, Eqs. (5.20) and (5.12) are substituted into Eq. (5.11). After some manipulations to recover the expressions for $g_{mn\nu}(\mathbf{k},\mathbf{q})$ and $B_{\mathbf{q}\nu}$, from Eqs. (3.65), and (5.23), respectively, one obtains

$$\Delta\tau_{\kappa\alpha p} = -\frac{2}{N_p}\sum_{\mathbf{q}\nu} B^*_{\mathbf{q}\nu}\left(\frac{\hbar}{2M_\kappa\omega_{\mathbf{q}\nu}}\right)^{\frac{1}{2}} e_{\kappa\alpha,\nu}(\mathbf{q})\, e^{i\mathbf{q}\cdot\mathbf{R}_p}. \tag{5.26}$$

Furthermore, the formation energy can be expressed in terms of the vector $A_{n\mathbf{k}}$ by starting from Eq. (5.16), substituting Eqs. (5.14), (5.20), and (5.12) for $K^0(\mathbf{r}, \mathbf{r}')$, $\psi(\mathbf{r})$, and $(C^0)^{-1}_{\kappa\alpha p,\kappa'\alpha' p'}$, respectively, and using the normalization constraint from Eq. (5.21) [9]. Further rearrangements then allow for identifying the expressions for $g_{mn\nu}(\mathbf{k}, \mathbf{q})$ and $B_{\mathbf{q}\nu}$, defined in Eqs. (3.65) and (5.23), respectively, and arriving at

$$\Delta E_f = \frac{1}{N_p} \sum_{n\mathbf{k}} |A_{n\mathbf{k}}|^2 (\varepsilon_{n\mathbf{k}} - \varepsilon_{\mathrm{CBM}}) - \frac{1}{N_p} \sum_{\mathbf{q}\nu} |B_{\mathbf{q}\nu}|^2 \hbar\omega_{\mathbf{q}\nu}, \tag{5.27}$$

as shown in Ref. [9]. When starting from Eq. (5.18), one obtains the compact expression

$$\Delta E_f = \varepsilon - \varepsilon_{\mathrm{CBM}} + \frac{1}{N_p} \sum_{\mathbf{q}\nu} |B_{\mathbf{q}\nu}|^2 \hbar\omega_{\mathbf{q}\nu}. \tag{5.28}$$

The first part of Eq. (5.27), involving the polaron eigenvector $A_{n\mathbf{k}}$, represents the electronic energy, while the sum over all phonon modes accounts for the vibrational energy contribution. When comparing the vibrational contribution to the phonon energy expression $E_{\mathbf{q}\nu}$ from Eq. (3.57), it becomes evident that $|B_{\mathbf{q}\nu}|^2$ can be interpreted as the occupation number of phonon mode $\mathbf{q}\nu$, contributing to the lattice distortion associated with the polaron [9, 10, 28].

Chapter 6

Stochastic Self-Consistent Harmonic Approximation

The harmonic phonon model derived in Section 3.3 is highly idealized: it ignores the temperature dependence of phonon energies and neglects anharmonic phonon-phonon interactions that lead to finite phonon lifetimes. The SSCHA incorporates both:

1. Temperature, by applying a variational treatment of the free energy, using the Gibbs-Bogoliubov inequality.
2. Anharmonic interactions, since the full BO potential $U(\{\hat{\boldsymbol{\tau}}_I\})$ is used without any truncation or approximation,

as discussed in Refs. [15, 29].

6.1. Gibbs-Bogoliubov Inequality

Considering the Hamiltonian of a system with possible microscopic states $\mu \in \Gamma$,

$$H(\mu) = H_0(\mu) + H_1(\mu), \tag{6.1}$$

for which the partition function Z_0 can be evaluated efficiently. Then the fraction Z/Z_0 can be written as

$$\frac{Z}{Z_0} = \int_\Gamma d\mu \underbrace{\frac{e^{-\beta H_0(\mu)}}{\int_\Gamma e^{-\beta H_0(\mu')} d\mu'}}_{\rho_0(\mu)} e^{-\beta H_1(\mu)} = \left\langle e^{-\beta H_1} \right\rangle_{\rho_0}, \tag{6.2}$$

which is the expectation value of H_1 with respect to the probability distribution $\rho_0(\mu)$, characterizing H_0 [30, pp. 164–168]. The convexity inequality $\langle g(x) \rangle \geq g(\langle x \rangle)$, which

holds for $g'(x) > 0$ and $g''(x) > 0$, and therefore for the exponential function, can be applied to Eq. (6.2) to arrive at

$$\frac{Z}{Z_0} \geq e^{-\beta \langle H_1 \rangle_{\rho_0}}, \tag{6.3}$$

according to [30, pp. 164–168]. Taking the natural logarithm and applying the definition of the Helmholtz free energy, $F = -k_B T \ln Z$, leads to the Gibbs-Bogoliubov inequality

$$F \leq F_0 + \langle H_1 \rangle_{\rho_0} \tag{6.4}$$

with

$$F_0 = \langle H_0 \rangle_{\rho_0} - TS_0 \tag{6.5}$$

and

$$S_0 = -k_B \langle \ln \rho_0 \rangle_{\rho_0}. \tag{6.6}$$

Substituting Eq. (6.5) into Eq. (6.4) leads to the alternative expression

$$F \leq \langle H \rangle_{\rho_0} - TS_0 \tag{6.7}$$

for the Gibbs-Bogoliubov inequality [30, pp. 164–168].

6.1.1. Free Energy Minimization

One strategy to approximate F using Eq. (6.7) is to choose a parametric form of the Hamiltonian $H_0 \equiv H_0(\mu; \boldsymbol{\lambda})$ with a set of parameters $\boldsymbol{\lambda} \equiv \{\lambda_i\}$. Then, H_0 becomes a trial Hamiltonian—with a corresponding probability distribution $\rho_{0,\boldsymbol{\lambda}}$—for the variational expression

$$\mathcal{F}[\boldsymbol{\lambda}] = \langle H \rangle_{\rho_{0,\boldsymbol{\lambda}}} - TS_0[\rho_{0,\boldsymbol{\lambda}}], \tag{6.8}$$

which can be minimized with respect to parameters $\boldsymbol{\lambda}$ [30, pp. 164–168].

6.2. Harmonic Trial Hamiltonian and Density Operator

For a many-body quantum system, the quantity corresponding to the classical probability density is the many-body density operator

$$\hat{\rho} = e^{-\beta \hat{H}}. \tag{6.9}$$

In order to minimize the functional $\mathcal{F}[\hat{\rho}_0]$ efficiently, the SSCHA constrains the trial density operator $\hat{\rho}_0$ to a multivariate Gaussian probability distribution. This circumvents

the computationally intractable variation over the unconstrained space of possible density operators. Thus, the parameterization of $\hat{\rho}_0$ is given by the nuclei's centroid positions $\boldsymbol{\mathcal{R}} \equiv \{\boldsymbol{\mathcal{R}}_I\}$ for each nucleus, and the covariance matrix $\boldsymbol{\Phi}$ [15, 29]. This is indicated by writing the trial density operator as $\hat{\rho}_{\boldsymbol{\mathcal{R}},\boldsymbol{\Phi}} \equiv \hat{\rho}_{0,\{\boldsymbol{\mathcal{R}},\boldsymbol{\Phi}\}}$ and turns the variational free energy expression of Eq. (6.8) into

$$\mathcal{F}[\boldsymbol{\mathcal{R}}, \boldsymbol{\Phi}] = \langle \hat{T} + U(\hat{\boldsymbol{\tau}}) \rangle_{\hat{\rho}_{\boldsymbol{\mathcal{R}},\boldsymbol{\Phi}}} - T S_0\left[\hat{\rho}_{\boldsymbol{\mathcal{R}},\boldsymbol{\Phi}}\right], \tag{6.10}$$

with the set of nuclear position operators $\hat{\boldsymbol{\tau}} \equiv \{\hat{\boldsymbol{\tau}}_I\}$. It has to be noted that the entropy in Eq. (6.10) neglects electronic degrees of freedom [15, 29].

A Gaussian trial density matrix is the equilibrium solution of a harmonic trial Hamiltonian

$$\mathcal{H}_{\boldsymbol{\mathcal{R}},\boldsymbol{\Phi}} = \hat{T} + \frac{1}{2} \sum_{\substack{I\alpha \\ J\beta}} (\hat{\tau}_{I\alpha} - \mathcal{R}_{I\alpha})\, \Phi_{I\alpha,J\beta}\, (\hat{\tau}_{J\beta} - \mathcal{R}_{J\beta}), \tag{6.11}$$

explaining part of the naming of the SSCHA [15, 29]. Due to the form of $\mathcal{H}_{\boldsymbol{\mathcal{R}},\boldsymbol{\Phi}}$, the matrix $\boldsymbol{\Phi}$ is also referred to as the auxiliary force constants matrix. The form of $\mathcal{H}_{\boldsymbol{\mathcal{R}},\boldsymbol{\Phi}}$ is well understood and allows the calculation of $\langle \hat{T} \rangle_{\hat{\rho}_{\boldsymbol{\mathcal{R}},\boldsymbol{\Phi}}}$ and $S_0\left[\hat{\rho}_{\boldsymbol{\mathcal{R}},\boldsymbol{\Phi}}\right]$ from known analytic expressions. Obtaining the expectation value of the BO potential $U(\hat{\boldsymbol{\tau}})$, which appears in Eq. (6.11), or the expectation value of other quantities is more challenging [15, 29].

It has to be stressed that the auxiliary force constants matrix cannot be directly interpreted as the physical force constants matrix with anharmonic contributions. Nevertheless, the anharmonic dispersion can be developed as a perturbative series with $\boldsymbol{\Phi}$ being its leading-order contribution. In order to obtain higher-order contributions, the so-called bubble correction needs to be taken into account [15, 29]. However, for some materials, e.g. many materials containing hydrogen, it was found that the bubble correction can be negligible in comparison to the contribution from $\boldsymbol{\Phi}$, reinstating the physical meaning of $\boldsymbol{\Phi}$ in these cases [15, 31].

6.3. Minimization Methods and Stochastic Sampling

6.3.1. Minimization with Preconditioned Gradient-Descent

In order to approximate the free energy of the system, $\mathcal{F}[\boldsymbol{\mathcal{R}}, \boldsymbol{\Phi}]$ needs to be minimized with respect to the centroids $\boldsymbol{\mathcal{R}}$ and the covariance matrix $\boldsymbol{\Phi}$. This can be efficiently done by using the gradient-descent method with a preconditioning, optimized for a perfect quadratic landscape. The expectation values of the BO potential $U(\hat{\boldsymbol{\tau}})$ and the BO forces $\mathbf{f}_I(\hat{\boldsymbol{\tau}})$ are necessary for evaluating $\mathcal{F}$, as well as its derivatives $\partial\mathcal{F}/\partial\mathcal{R}_{I\alpha}$ and $\partial\mathcal{F}/\partial\Phi_{I\alpha,J\beta}$,

but they are not analytically obtainable. However, since $U(\hat{\boldsymbol{\tau}})$ and $\mathbf{f}_I(\hat{\boldsymbol{\tau}})$ can be directly obtained from a DFT calculation, the expectation values $\langle U(\hat{\boldsymbol{\tau}})\rangle_{\hat{\rho}_{\boldsymbol{\mathcal{R}},\boldsymbol{\Phi}}}$ and $\langle \mathbf{f}_I(\hat{\boldsymbol{\tau}})\rangle_{\hat{\rho}_{\boldsymbol{\mathcal{R}},\boldsymbol{\Phi}}}$ can be approximated by the stochastic sampling method explained in Subsection 6.3.3 [15, 29].

The gradient-descent minimization is started from an initial guess $\boldsymbol{\mathcal{R}}^{(0)}$ and $\boldsymbol{\Phi}^{(0)}$ for the centroids and auxiliary force constants, respectively. The corresponding trial Hamiltonian $\mathcal{H}^{(0)}$ and the trial density matrix $\rho_{\boldsymbol{\mathcal{R}}^{(0)},\boldsymbol{\Phi}^{(0)}}(\hat{\boldsymbol{\tau}}_i)$ are then utilized for calculating the derivatives for the first minimization step. Each gradient-descent step n yields a new set of centroids $\boldsymbol{\mathcal{R}}^{(n)}$ and auxiliary force constants $\boldsymbol{\Phi}^{(n)}$, which parameterize $\mathcal{H}^{(n)}$ and $\rho_{\boldsymbol{\mathcal{R}}^{(n)},\boldsymbol{\Phi}^{(n)}}(\hat{\boldsymbol{\tau}}_i)$, allowing the calculation of the gradient for step $n+1$ [15, 29].

6.3.2. Self-Consistent Minimization of Auxiliary Force Constants

In case the centroids are clamped and only the anharmonic contributions to the force constants are of interest, the SSCHA theory yields the SSCHA self-consistent equations

$$\Phi_{I\alpha,J\beta}(\boldsymbol{\mathcal{R}}) = \left\langle \frac{\partial^2 U(\hat{\boldsymbol{\tau}})}{\partial \tau_{I\alpha}\partial \tau_{J\beta}} \right\rangle_{\hat{\rho}_{\boldsymbol{\mathcal{R}},\boldsymbol{\Phi}}} \tag{6.12}$$

as an alternative for minimizing $\mathcal{F}[\boldsymbol{\mathcal{R}},\boldsymbol{\Phi}]$ with respect to $\boldsymbol{\Phi}$ only [15, 29]. The expectation values of the second derivatives of $U(\hat{\boldsymbol{\tau}})$ can be approximated by the stochastic sampling explained in Subsection 6.3.3. The second derivatives for one specific configuration $\boldsymbol{\tau}$ can for instance be calculated using DFPT.

6.3.3. Stochastic Sampling in the Basis of Real Space Configurations

The expectation value of an observable $\hat{O}$ is generally calculated as $\langle \hat{O}\rangle_{\hat{\rho}} = \mathrm{Tr}\left[\hat{\rho}\,\hat{O}\right]$. In the basis of real space configurations $|\boldsymbol{\tau}\rangle$, the expectation value is calculated as

$$\langle O(\hat{\boldsymbol{\tau}})\rangle_{\hat{\rho}_{\boldsymbol{\mathcal{R}},\boldsymbol{\Phi}}} = \int d\boldsymbol{\tau}\, O(\boldsymbol{\tau})\rho_{\boldsymbol{\mathcal{R}},\boldsymbol{\Phi}}(\boldsymbol{\tau}), \tag{6.13}$$

with trial density matrix $\rho_{\boldsymbol{\mathcal{R}},\boldsymbol{\Phi}}(\boldsymbol{\tau}) = \langle\boldsymbol{\tau}|\,\hat{\rho}_{\boldsymbol{\mathcal{R}},\boldsymbol{\Phi}}\,|\boldsymbol{\tau}\rangle$. The integral can be approximated by Monte Carlo (MC) sampling, drawing N_c configurations $\boldsymbol{\tau}_i$, according to the underlying probability distribution $\rho_{\boldsymbol{\mathcal{R}},\boldsymbol{\Phi}}(\boldsymbol{\tau})$ [15, 29]. The corresponding values for the observable $O(\boldsymbol{\tau_i})$ can be calculated using a suitable, parallelizable *ab initio* method, such that the approximated expectation value is finally calculated as

$$\langle O(\hat{\boldsymbol{\tau}})\rangle_{\hat{\rho}_{\boldsymbol{\mathcal{R}},\boldsymbol{\Phi}}} \approx \frac{1}{N_\mathrm{c}}\sum_{i=1}^{N_\mathrm{c}} O(\boldsymbol{\tau}_i), \tag{6.14}$$

as explained in Refs. [15, 29]. It would be unnecessarily expensive to create a new sample of configurations $\boldsymbol{\tau}_i$ and to calculate the corresponding observables $O(\boldsymbol{\tau_i})$ for each minimization step. Instead, a reweighting method called importance sampling can be used to lower the computational cost: At step n, after drawing the original sample from $\rho_{\boldsymbol{\mathcal{R}}^{(0)},\boldsymbol{\Phi}^{(0)}}(\boldsymbol{\tau})$, each sample is assigned a weight

$$\rho_i^{(n)} = \frac{\rho_{\boldsymbol{\mathcal{R}}^{(n)},\boldsymbol{\Phi}^{(n)}}(\boldsymbol{\tau}_i)}{\rho_{\boldsymbol{\mathcal{R}}^{(0)},\boldsymbol{\Phi}^{(0)}}(\boldsymbol{\tau}_i)} \tag{6.15}$$

and the integral is approximated as

$$\langle O(\hat{\boldsymbol{\tau}})\rangle_{\hat{\rho}_{\boldsymbol{\mathcal{R}}^{(n)},\boldsymbol{\Phi}^{(n)}}} \approx \frac{\sum_i \rho_i^{(n)}\, O(\boldsymbol{\tau}_i)}{\sum_j \rho_j^{(n)}}. \tag{6.16}$$

A given sample can be reused until the ratio between the Kong-Liu effective sample size,

$$N_{\text{eff}} = \frac{\sum_{i=1}^{N_\text{c}} (\rho_i^{(n)})^2}{(\sum_{j=1}^{N_\text{c}} \rho_j^{(n)})^2}, \tag{6.17}$$

and the total number of configurations N_c falls below a certain value η, such that

$$\frac{N_{\text{eff}}}{N_\text{c}} < \eta, \tag{6.18}$$

typically chosen around 1/2 [15, 29]. In that case, a new sample $\boldsymbol{\tau}_i$, representing the probability distribution $\rho_{\boldsymbol{\mathcal{R}}^{(n)},\boldsymbol{\Phi}^{(n)}}(\boldsymbol{\tau}_i)$, has to be drawn and the corresponding observables have to be calculated from appropriate *ab initio* methods. After that, the next cycle of minimization steps can be performed using $\rho_{\boldsymbol{\mathcal{R}}^{(n)},\boldsymbol{\Phi}^{(n)}}(\boldsymbol{\tau}_i) \rightarrow \rho_{\boldsymbol{\mathcal{R}}^{(0)},\boldsymbol{\Phi}^{(0)}}(\boldsymbol{\tau}_i)$, as the new reference distribution [15, 29].

Chapter 7

Computational Methods

7.1. Methods for Solving the Kohn-Sham Equations

One of the various methods for solving the Kohn-Sham equations is the plane wave representation. It employs orbitals of the same form as those used in the derivation of the Bloch theorem in Eq. (3.26). Consequently, the equations to be solved for obtaining the plane wave coefficients are Eqs. (3.27), with the Fourier-transformed Kohn-Sham potential $V_{\mathrm{KS}}(\mathbf{G})$ [17, pp. 246–253, pp. 155–158]. In a practical calculation, the set of $\mathbf{G}$-vectors must be limited by a cutoff energy E_{cut}, corresponding to the kinetic energy of a free particle, such that only wave vectors satisfying

$$|\mathbf{G}+\mathbf{k}| \leq \sqrt{2E_{\mathrm{cut}}} \tag{7.1}$$

are taken into account. For a fixed $\mathbf{k}$-vector from the 1st BZ, Eqs. (3.27) can be written as an eigenvalue problem for the plane wave coefficients $C_{\mathbf{G}+\mathbf{k}}$ and the corresponding eigenvalues $\varepsilon_{\mathbf{k}}$. The number of used $\mathbf{G}$-vectors determines the dimensionality of the eigenvalue problem and therefore the number of solutions, but also the necessary computational effort. The set of $\mathbf{k}$-vectors for which the calculations are performed is usually taken from a regular mesh spanning the 1st BZ, where a finer mesh means more accuracy but also a higher computational effort [17, pp. 246–253, pp. 155–158].

However, the large number of different $\mathbf{G}$-vectors necessary to describe the Bloch functions near the nuclei, where they must have high wave numbers to be orthogonal to the eigenstates of the inner core electrons, makes the pure plane wave method computationally expensive. This problem can be circumvented by creating a new basis set $\left|\psi^b_{n\mathbf{k}}\right\rangle$ by removing the plane waves' overlap with the core electrons' Bloch functions $|\psi^c_{l\mathbf{k}}\rangle$, such that

$$\left|\psi^b_{n\mathbf{k}}\right\rangle = |\mathbf{k}\rangle - \sum_{l<n} |\psi^c_{l\mathbf{k}}\rangle\langle\psi^c_{l\mathbf{k}}|\mathbf{k}\rangle = (1-\hat{P}_{\mathbf{k}})\,|\mathbf{k}\rangle\,, \tag{7.2}$$

with $\langle\mathbf{r}|\mathbf{k}\rangle = e^{i\mathbf{k}\cdot\mathbf{r}}$ [18, pp. 126–136] [17, pp. 258–263].

The core electrons' Bloch functions are constructed from Eq. (3.40), using the core electrons' localized orbitals $\phi_l(\mathbf{r}-\mathbf{R}_p)$ as Wannier functions $w_p(\mathbf{r})$. This method is called the orthogonalized plane wave (OPW) method and reduces the number of necessary $\mathbf{G}$-vectors considerably [17, pp. 246–253, pp. 155–158] [18, pp. 126–136]. The Bloch functions for $\mathbf{k}$-points from the 1st BZ, describing non-core electrons, are then constructed by the linear-combination *Ansatz*

$$|\psi_{n\mathbf{k}}\rangle = \sum_{\mathbf{G}} a_{\mathbf{k}+\mathbf{G}} \left|\psi^b_{n\mathbf{k}+\mathbf{G}}\right\rangle = (1-\hat{P}_{\mathbf{k}}) \sum_{\mathbf{G}} a_{\mathbf{k}+\mathbf{G}} \left|\mathbf{k}+\mathbf{G}\right\rangle . \tag{7.3}$$

Substituting the last expression of Eq. (7.3) into the stationary Schrödinger equation allows for a regrouping of terms such that the projectors $\hat{P}_{\mathbf{k}}$ can be considered an additional part of the potential. The resulting composite potential is called the pseudopotential and allows for an efficient solution using a plane wave basis [17, pp. 246–253, pp. 155–158] [18, pp. 126–136]. The electron-nuclear potential in DFT calculations is therefore constructed as

$$V^{\mathrm{ps}}_{\text{e-n}}(\mathbf{r}) = \sum_{\kappa p} v^{\mathrm{ps}}_{\kappa}(\mathbf{r}-\boldsymbol{\tau}_{\kappa p}), \tag{7.4}$$

with the pseudopotential $v^{\mathrm{ps}}_{\kappa}(\mathbf{r})$ for nucleus κ [19].

The initial guess for the electron density $n(\mathbf{r})$ could, for example, be constructed as the superposition of the electron densities of the atomic orbitals according to the atomic structure of the investigated material [24]. Fig. 7.1 sketches the self-consistent procedure to obtain converged Kohn-Sham orbitals. After reaching convergence, the electronic ground-state density, $n(\mathbf{r})$, is calculated from Eq. (4.7) [18, pp. 211–212].

7.2. Band Structure Calculations

A priori, the Kohn-Sham orbitals and eigenvalues do not convey a direct physical meaning, since DFT is a theory for calculating a system's ground-state energy and electron density $n(\mathbf{r})$. Therefore, $\varphi_i(\mathbf{r})$ and ε_i should be viewed as auxiliary objects for obtaining the expectation values of $\hat{T}_{\mathrm{s}}$ in Eq. (4.6) and recalculating the ground-state density with Eq. (4.7) [18, pp. 211–212] [19]. However, they do have an approximate physical meaning, which can be shown using the methods of quantum field theory. Consequently, they can serve as a good starting point for describing material properties and even materials' band structures. Nevertheless, as a rule of thumb, band gaps calculated from Kohn-Sham eigenvalues are underestimated by about 40% [17, pp. 152–162]. Substituting the converged Kohn-Sham potential $V_{\mathrm{SCF}}(\mathbf{r})$ into Eq. (3.27) will yield the DFT band structure $\varepsilon_{n\mathbf{k}}$, and Kohn-Sham orbitals $\psi_{n\mathbf{k}}(\mathbf{r})$ in Bloch representation. Since $V_{\mathrm{SCF}}(\mathbf{r})$

Input : $V_{\text{e-n}}(\mathbf{r})$, N, initial guess for $n(\mathbf{r})$, convergence threshold ϵ
Output : Converged Kohn-Sham orbitals and eigenvalues $\{(\varphi_i(\mathbf{r}), \varepsilon_i)\}$

repeat
  $\widetilde{n}(\mathbf{r}) \leftarrow n(\mathbf{r})$;
  $V_H(\mathbf{r}) \leftarrow$ `ComputeHartreePotential(`$\widetilde{n}(\mathbf{r})$`)`;
  $V_{\text{xc}}(\mathbf{r}) \leftarrow$ `ComputeExchCorr(`$\widetilde{n}(\mathbf{r})$`)`;
  $\{(\varphi_i(\mathbf{r}), \varepsilon_i)\} \leftarrow$ `SolveKohnSham(`$V_{e\text{-}n}(\mathbf{r})$, $V_H(\mathbf{r})$, $V_{xc}(\mathbf{r})$, N`)`;
  $n(\mathbf{r}) \leftarrow$ `ComputeElectronDensity(`$\{(\varphi_i(\mathbf{r}), \varepsilon_i)\}$`)`;
until `DensityConverged(`$\widetilde{n}(\mathbf{r})$, $n(\mathbf{r})$, ϵ`)`;
return $\{(\varphi_i(\mathbf{r}), \varepsilon_i)\}$

Fig. 7.1.: Self-consistent loop for solving the Kohn-Sham equations [18, pp. 211–212]

remains unchanged during this calculation, this is often referred to as a non-self-consistent calculation [17, pp. 152–162]. The DOS can be further decomposed by projecting the Kohn-Sham orbitals onto orthogonalized atomic wave functions. This procedure yields the projected density of states (PDOS), allowing for a distinction between the contributions of different atomic orbitals to the DOS, according to the calculated overlaps [32].

7.3. Interpolation Methods

Calculations for phenomena involving electron-phonon interactions require a much finer sampling of the 1$^{\text{st}}$ BZ than commonly used for DFT or DFPT phonon calculations, using grids of the order $10 \times 10 \times 10$ [24]. Going beyond that by solely using *ab initio* calculations for obtaining phonon frequencies, or electron-phonon matrix elements, makes these types of calculations intractable, since each of them is as expensive as a DFT total energy minimization. For that reason, interpolation methods for obtaining phonon frequencies, normal modes of vibration, electronic eigenenergies, and electron-phonon matrix elements, have to be employed, which are based on the Fourier interpolation method [24].

7.3.1. Fourier Interpolation of Interatomic Force Constants

Starting from the electronic part of the interatomic force constants, obtained from DFPT calculations on a uniform **q**-grid, one can efficiently obtain the corresponding real-space

force constants as

$$C_{\kappa\alpha,\kappa'\alpha'}(\mathbf{R}_p) = \frac{1}{N_p}\sum_{\mathbf{q}} C_{\kappa\alpha,\kappa'\alpha'}(\mathbf{q})\, e^{i\mathbf{q}\cdot\mathbf{R}_p}, \tag{7.5}$$

via inverse Fourier transform, using fast Fourier transform (FFT) [19, 33]. The granularity of the *ab initio* **q**-grid has to be chosen such that the decay of the matrix elements $C_{\kappa\alpha,\kappa'\alpha'}(\mathbf{R}_p)$ is sufficient to capture the essential contributions within the corresponding Born-von-Kármán supercell. This can be done *a posteriori* by inspecting the decay of the dominant real-space matrix elements:

$$\max D(\mathbf{R}_p) \equiv \max_{\kappa\alpha,\kappa'\alpha'} \left| \frac{C_{\kappa\alpha,\kappa'\alpha'}(\mathbf{R}_p)}{\sqrt{M_\kappa M_{\kappa'}}} \right| \tag{7.6}$$

with respect to $|\mathbf{R}_p|$ [19, 33]. Once a sufficient decay is verified, a Fourier transform can be applied to obtain the reciprocal space force constants as

$$C_{\kappa\alpha,\kappa'\alpha'}(\mathbf{q}) = \sum_{p} C_{\kappa\alpha,\kappa'\alpha'}(\mathbf{R}_p)\, e^{-i\mathbf{q}\cdot\mathbf{R}_p}, \tag{7.7}$$

on a finer **q**-grid than used in the *ab initio* phonon calculation. This method is called Fourier interpolation. The accuracy of the interpolated $C_{\kappa\alpha,\kappa'\alpha'}(\mathbf{q})$ can be verified by performing a full DFPT calculation for a small sample of **q**-points, not included in the *ab initio* **q**-grid [19, 33].

In polar materials, dipole-dipole interactions cause long-range interatomic force constants in real space. For this reason, a Fourier interpolation of $C_{\kappa\alpha,\kappa'\alpha'}(\mathbf{R}_p)$ is not directly applicable, and only the electronic part $C^{\mathrm{el}}_{\kappa\alpha,\kappa'\alpha'}(\mathbf{q})$, which is short-range, will be interpolated as described. For each **q**-point added to the fine grid, the ionic part $C^{\mathrm{ion}}_{\kappa\alpha,\kappa'\alpha'}(\mathbf{q})$ has to be separately calculated, as described in Subsection 4.3.3 [19, 33].

7.3.2. Wannier Interpolation

The Fourier interpolation scheme, as presented above, can be readily applied to isolated bands. The necessary steps are calculating $|w_{np}\rangle$ using Eq. (3.41), transforming them back to $\left|\overline{\psi}_{n\mathbf{k}}\right\rangle$ on a finer **k**-grid, using Eq. (3.40), and calculating the interpolated eigenenergies as

$$\overline{\varepsilon}_{n\mathbf{k}} = \left\langle \overline{\psi}_{n\mathbf{k}} \right| \hat{H}_{\mathrm{SCF}} \left| \overline{\psi}_{n\mathbf{k}} \right\rangle, \tag{7.8}$$

as shown in Ref. [22]. When using MLWFs for a group of J bands, the corresponding unitary gauge transformation $U_{nm\mathbf{k}}$ has to be considered. The Fourier-interpolated Hamiltonian matrix elements

$$\overline{H}^{\mathrm{w}}_{nm\mathbf{k}} = \left\langle \overline{\psi}^{\mathrm{w}}_{n\mathbf{k}} \right| \hat{H}_{SCF} \left| \overline{\psi}^{\mathrm{w}}_{m\mathbf{k}} \right\rangle = \sum_{p} e^{i\mathbf{k}\cdot\mathbf{R}_p} \underbrace{\langle w_{n0}| \hat{H}_{SCF} |w_{mp}\rangle}_{H_{nm}(\mathbf{R}_p)} \tag{7.9}$$

are still in the basis of the MLWF's Wannier gauge and therefore non-diagonal. Consequently, a diagonalization step has to be introduced in order to obtain the interpolated Hamiltonian matrix elements

$$\overline{H}_{nm\mathbf{k}} = \left[\overline{U}^{\dagger}_{\mathbf{k}} \overline{H}^{\mathrm{w}}_{\mathbf{k}} \overline{U}_{\mathbf{k}}\right]_{nm} = \delta_{nm} \overline{\varepsilon}_{n\mathbf{k}} \tag{7.10}$$

in the Hamiltonian's eigengauge, also yielding the interpolated eigenvalues $\overline{\varepsilon}_{n\mathbf{k}}$ [22].

The most involved case deals with a group of J bands that is not separated from other bands. These are referred to as entangled bands, making up a total of $\mathcal{J}$ bands that first need to be projected onto a subspace of J bands in order to continue the procedure of finding MLWFs. The set of $\mathcal{J}$ bands is first projected onto J localized trial orbitals dominating the energy region of the desired band group [22].

To check whether the coarse *ab initio* **k**-grid is fine enough and the MLWFs are sufficiently localized to justify a Wannier interpolation, one must verify the sufficient decay of the dominant real-space Hamiltonian matrix elements:

$$\max H(\mathbf{R}_p) \equiv \max_{nm} |H_{nm}(\mathbf{R}_p)|, \tag{7.11}$$

with respect to $|\mathbf{R}_p|$ [33].

7.3.3. Interpolation of Electron-Phonon Matrix Elements

In the case of electron-phonon matrix elements, the lattice-periodic parts of the Bloch functions $u_{n\mathbf{k}}(\mathbf{r})$ and the phonon derivatives $\Delta_{\mathbf{q}\nu} v_{\mathrm{SCF}}(\mathbf{r})$, occurring in the definition of $g_{mn\nu}(\mathbf{k}, \mathbf{q})$, first have to be expressed in terms of their localized counterparts $w_{mp}(\mathbf{r})$ and $\partial_{\kappa\alpha p} V_{\mathrm{SCF}}(\mathbf{r})$, respectively [24]. From Eq. (3.44) follows the expression

$$u_{n\mathbf{k}}(\mathbf{r}) = \sum_{mp} e^{-i\mathbf{k}\cdot(\mathbf{r}-\mathbf{R}_p)} \, U^{\dagger}_{mn\mathbf{k}} \, w_{mp}(\mathbf{r}), \tag{7.12}$$

for the lattice-periodic part of a Bloch function [24]. The expression for $\Delta_{\mathbf{q}\nu} v_{\mathrm{SCF}}(\mathbf{r})$ in terms of $\partial_{\kappa\alpha p} V_{\mathrm{SCF}}(\mathbf{r})$ is already explicitly given by Eq. (3.66). Substituting those expressions into Eq. (3.65), the definition of $g_{mn\nu}(\mathbf{k}, \mathbf{q})$, yields

$$g_{mn\nu}(\mathbf{k}, \mathbf{q}) = \sum_{p_{\mathbf{k}} \, p_{\mathbf{q}}} \Bigg[e^{i(\mathbf{k}\cdot\mathbf{R}_{p_{\mathbf{k}}} + \mathbf{q}\cdot\mathbf{R}_{p_{\mathbf{q}}})} \times \sum_{m'n'\kappa\alpha} \sqrt{\frac{\hbar}{2M_\kappa \omega_{\mathbf{q}\nu}}} e_{\kappa\alpha,\nu}(\mathbf{q}) \, U_{mm'\mathbf{k}+\mathbf{q}} \, g_{m'n'\kappa\alpha}(\mathbf{R}_{p_{\mathbf{k}}}, \mathbf{R}_{p_{\mathbf{q}}}) \, U^{\dagger}_{n'n\mathbf{k}} \Bigg], \tag{7.13}$$

with the real-space electron-phonon matrix elements

$$g_{mn\kappa\alpha}(\mathbf{R}_{p_\mathbf{k}}, \mathbf{R}_{p_\mathbf{q}}) = \langle w_{m0} | \, \partial_{\kappa\alpha p_\mathbf{q}} V_{\mathrm{SCF}}(\mathbf{r}) \, | w_{np_\mathbf{k}} \rangle \,, \tag{7.14}$$

as stated in [24]. These can in turn be written in terms of reciprocal-space quantities:

$$g_{mn\kappa\alpha}(\mathbf{R}_{p_\mathbf{k}}, \mathbf{R}_{p_\mathbf{q}}) = \frac{1}{N_{p_\mathbf{k}} N_{p_\mathbf{q}}} \sum_{\mathbf{k}\,\mathbf{q}} \Bigg[e^{-i(\mathbf{k}\cdot\mathbf{R}_{p_\mathbf{k}} + \mathbf{q}\cdot\mathbf{R}_{p_\mathbf{q}})} \times \sum_{m'n'\nu} \sqrt{\frac{2M_\kappa \omega_{\mathbf{q}\nu}}{\hbar}} e^*_{\kappa\alpha,\nu}(\mathbf{q}) \, U^\dagger_{mm'\mathbf{k}+\mathbf{q}} \, g_{m'n'\nu}(\mathbf{k}, \mathbf{q}) \, U_{n'n\mathbf{k}} \Bigg], \tag{7.15}$$

as derived in [24]. The *ab initio* **q**-grid can be coarser than, but must be commensurate with the *ab initio* **k**-grid. Consequently, the corresponding Born-von-Kármán supercells are allowed to consist of different numbers of unit cells, $N_{p_\mathbf{k}}$ and $N_{p_\mathbf{q}}$, associated with the **k**- and **q**-grids, respectively. The indices $p_\mathbf{k}$ and $p_\mathbf{q}$ therefore run from 1 to $N_{p_\mathbf{k}}$ and 1 to $N_{p_\mathbf{q}}$, respectively [24].

All quantities in Eq. (7.15) are known on the coarse *ab initio* grids:

1. A DFT calculation on a coarse **k**-grid yields the Kohn-Sham orbitals in Bloch representation, needed for DFPT phonon calculations, Wannierization, and for calculating electron-phonon matrix elements.

2. A DFPT calculation on a coarse **q**-grid leads to Cartesian derivatives $\partial_{\kappa\alpha,\mathbf{q}} v_{\mathrm{SCF}}(\mathbf{r})$ for monochromatic displacements. Phonon frequencies $\omega_{\mathbf{q}\nu}$ and normal modes $e_{\kappa\alpha,\nu}(\mathbf{q})$ are obtained from

   a) DFPT, yielding strictly harmonic phonons, or from

   b) SSCHA minimization, incorporating anharmonic contributions [34, 35].

   With Eq. (3.66), these quantities combine to form the phonon derivatives $\Delta_{\mathbf{q}\nu} v_{\mathrm{SCF}}(\mathbf{r})$, necessary for calculating electron-phonon matrix elements.

3. A Wannierization for obtaining MLWFs through minimizing the Wannier functions' spreads, defined in Eq. (3.45), yields the Wannier gauge transformation $U_{nm\mathbf{k}}$.

Therefore, the real-space electron-phonon matrix elements $g_{mn\kappa\alpha}(\mathbf{R}_{p_\mathbf{k}}, \mathbf{R}_{p_\mathbf{q}})$, corresponding to the coarse *ab initio* **k**- and **q**-grids, can be readily obtained. The interpolation to fine **k**- and **q**-grids then takes place by transforming $g_{mn\kappa\alpha}(\mathbf{R}_{p_\mathbf{k}}, \mathbf{R}_{p_\mathbf{q}})$ back to their reciprocal space counterparts $g_{mn\nu}(\mathbf{k}, \mathbf{q})$, using Eq. (7.13) on the fine grids. To achieve

this, the corresponding fine-grid phonon frequencies, normal modes of vibration, and Wannier gauge transformation matrices have to be obtained using Fourier interpolation and Wannier interpolation, as described in previous Subsections 7.3.1 and 7.3.2, respectively.

An interpolation to $g_{mn\nu}(\mathbf{k}, \mathbf{q})$ primarily relies on sufficiently decaying real-space interatomic force constants and real-space Hamiltonian matrix elements. Furthermore, the quality of interpolated electron-phonon matrix elements depends on a sufficient decay of $g_{mn\kappa\alpha}(\mathbf{R}_{p_\mathbf{k}}, 0)$ and $g_{mn\kappa\alpha}(0, \mathbf{R}_{p_\mathbf{q}})$. In analogy to the previous two subsections, it is therefore necessary to inspect the dominant real-space matrix elements:

$$\max g(\mathbf{R}_{p_\mathbf{k}}) \equiv \max_{mn\kappa\alpha} |g_{mn\kappa\alpha}(\mathbf{R}_{p_\mathbf{k}}, 0)|, \tag{7.16}$$

and

$$\max g(\mathbf{R}_{p_\mathbf{q}}) \equiv \max_{mn\kappa\alpha} \left|g_{mn\kappa\alpha}(0, \mathbf{R}_{p_\mathbf{q}})\right|, \tag{7.17}$$

with respect to $|\mathbf{R}_{p_\mathbf{k}}|$, and $\left|\mathbf{R}_{p_\mathbf{q}}\right|$, respectively. The decay of $\max D(\mathbf{R}_p)$, $\max H(\mathbf{R}_p)$, $\max g(\mathbf{R}_{p_\mathbf{k}})$, and $\max g(\mathbf{R}_{p_\mathbf{q}})$ is generally considered sufficient in case of convergence to a plateau within the supercell [24, 22, 33].

7.4. Makov-Payne Correction

The formation energy and eigenvalue obtained from a polaron calculation in a periodic supercell contain spurious energy contributions due to interactions between the polaron and its periodic images. This issue also occurs in energy calculations for charge defects in a periodic supercell, where the Makov-Payne correction is applied to remove these artifacts. Polarons and charge defects are similar in this regard, making the Makov-Payne correction applicable to polaron formation calculations [9]. The key aspect of the Makov-Payne correction is that the formation energy ΔE_f and the eigenvalue ε scale linearly with the inverse of increasing supercell size, for sufficiently large supercells. This allows for a linear extrapolation to infinite supercell size by performing a linear fit to the data points in the linear regime [9, 36]. The interpolation of the electron-phonon matrix elements and subsequent polaron calculations must therefore be performed for a range of fine $\mathbf{k}$- and $\mathbf{q}$-grids, corresponding to increasing supercell sizes, in order to apply the Makov-Payne correction [28].

Chapter 8

Computational Setup and Workflow

The *ab initio* polaron theory described in Section 5 is implemented in the open-source software package EPW [11, 12], which utilizes Wannier90 [14]. Both EPW and Wannier90 are distributed as part of the DFT-based Quantum ESPRESSO 7.2 code [13]. All DFT calculations employed optimized norm-conserving Vanderbilt pseudopotentials [37] and a Perdew-Burke-Ernzerhof (PBE) exchange-correlation functional [38]. The SSCHA minimization, as described in Chapter 6, was performed using SSCHA 1.2 [15].

A plane-wave basis with a cutoff energy of 100 Ry was used for all QE calculations, unless stated otherwise.

8.1. Preparatory Calculations for Lithium Fluoride

LiF is a salt that crystallizes in the rock-salt structure, forming a face-centered cubic (FCC) lattice with a diatomic basis consisting of Li at $(0,0,0)^T$ and F at $(\frac{a}{2},\frac{a}{2},\frac{a}{2})^T$ [10]. The atomic masses for Li and F are $M_{\mathrm{Li}} = 6.941\,\mathrm{u}$ and $M_{\mathrm{F}} = 18.9984\,\mathrm{u}$, respectively [28].

8.1.1. Relaxation

As an initial preparatory step, a relaxation calculation was performed with respect to the lattice constant a, initialized at $a = 7.57034\,a_0$. The associated DFT calculations were performed on a uniform, $\mathbf{\Gamma}$-centered $\mathbf{k}$-grid of $16 \times 16 \times 16$ and using a cutoff energy of 150 Ry. The convergence thresholds were set to 10^{-12} Ry for the self-consistent calculations and $7.35 \cdot 10^{-6}\,\mathrm{Ry}/a_0$ for any force component acting on the ions.

8.1.2. Band Structure

To gain a general understanding of LiF's electronic structure and to identify relevant bands for the polaron calculations, a band structure calculation was performed. First, a self-consistent DFT calculation was done on a $\mathbf{k}$-grid of $16 \times 16 \times 16$, using the relaxed

lattice constant, a convergence threshold of 10^{-12} Ry, and a cutoff energy of 150 Ry. Then, a non-self-consistent calculation was carried out for 15 bands. The **k**-path, connecting high-symmetry points of the BZ, was chosen as **W-L-Γ-X-W-K**, following Ref. [10]. Additionally, the calculated and plotted band structure helped in identifying degenerate bands, that needed to be disentangled during the Wannierization step, and in validating the band structure obtained from the Wannier interpolation.

8.1.3. Projected Density of States

To identify the atomic orbitals dominating certain bands, energy ranges within bands, or groups of bands, the PDOS was calculated for the conduction band and the top three valence bands. This was essential for selecting appropriate initial projections for Wannierizing bands that are involved in electron and hole polaron formation.

8.1.4. Phonon Dispersion

An initial phonon calculation was performed, which later served to validate the phonon dispersion obtained from Fourier interpolation during Wannierization. The convergence threshold was set to 10^{-14} Ry, and a uniform, **Γ**-centered **q**-grid of $8 \times 8 \times 8$ was used. The phonon dispersion was visualized along the **W-L-Γ-X-W-K** high-symmetry path. It is essential that any **q**-grid used in a DFPT calculation is commensurate with the **k**-grid used in the preceding DFT calculation. This means that Eq. (4.31) must hold for all combinations of **k**- and **q**-points, ensuring that adding any point from the **q**-grid to any point from the **k**-grid in turn results in a point on the **k**-grid, up to a reciprocal lattice vector **G**. The $8 \times 8 \times 8$ **q**-grid satisfies this commensurability condition for the previously used $16 \times 16 \times 16$ **k**-grid.

8.2. Polaron Calculations for Lithium Fluoride

The first three steps necessary for polaron formation calculations are a self-consistent DFT calculation, a DFPT phonon calculation, and a non-self-consistent calculation. These were carried out using QE, yielding the converged Kohn-Sham Hamiltonian $\hat{H}^0_{SCF}$, its solutions $(\psi_{n\mathbf{k}}(\mathbf{r}), \varepsilon_{n\mathbf{k}})$, the phonon dispersion $\omega_{\mathbf{q}\nu}$, the normal modes of vibration $e_{\kappa\alpha,\nu}(\mathbf{q})$, and the converged monochromatic derivatives $\partial_{\kappa\alpha,\mathbf{q}} v_{\mathrm{SCF}}(\mathbf{r})$ of the self-consistent-field potential. The calculations followed the setup described in Section 8.1, except that the **k**- and **q**-grids were both chosen as uniform, **Γ**-centered $12 \times 12 \times 12$ grids. The calculations for electron and hole polaron were identical, up to this point.

8.2.1. Electron Polaron

The electron polaron arises from an electron added on top of the Fermi sea. Since LiF is an insulator, its valence bands are fully occupied and assumed to remain unchanged. Only the unoccupied states near the conduction-band bottom contribute to the electron polaron formation. Thus, the five valence bands of LiF were excluded from the calculation of the electron-phonon matrix elements.

Wannierization

The Wannierization and the calculation of electron-phonon matrix elements in Wannier representation were carried out using EPW, which internally utilizes Wannier90 for obtaining MLWFs. As shown in Fig. 9.3, the preparatory band calculation revealed a degeneracy near the **W** high-symmetry point between the conduction band and the next higher band. Therefore, disentangling these bands was necessary to properly represent the conduction band using a MLWF:

1. The first step was to identify an initial projection in the form of an atomic orbital that dominates in the energy region of interest. This was done by selecting the atomic orbitals that significantly overlap with the Bloch functions in this energy region, as indicated by the PDOS [39]. For the electron polaron, the PDOS at the conduction-band bottom was considered to select suitable atomic orbitals. Hence, the *s*-orbitals of Li and F, which dominate in this regime, were considered as candidates for the initial projections.

2. In the second step, a disentanglement energy window was set to fully contain the target band and the main weight of the projector. This window, ranging from 9.0 eV to 15.62 eV, was chosen based on the calculated band structure and the PDOS [39].

3. Finally, a frozen energy window that does not contain any contributions outside the domain in which the initial projection dominate was defined. During Wannierization, the Bloch states inside this window do not rotate with other states outside of it [39]. The frozen energy window limits were chosen as 9.0 eV and 15.4 eV, fully excluding the 2^{nd} conduction band.

The disentanglement and frozen energy windows used for Wannierization are both indicated in Fig. 9.4. The number of iterations for obtaining the MLWF was set to 500. Eventually, the MLWF obtained using the *s*-orbital of fluorine as the initial projection was used for further calculations, as it led to a smaller spread of the resulting MLWF. After

obtaining the MLWF using Wannier90, EPW directly calculated the electron-phonon matrix elements $g_{mn\kappa\alpha}(\mathbf{R}_{p_k}, \mathbf{R}_{p_q})$ in the Wannier representation [28].

Electron-Phonon Matrix Interpolation and Polaron Calculations

EPW was used to interpolate the electron-phonon matrix elements to finer **k**- and **q**-grids, as explained in Section 7.3, and to solve the polaron equations derived in Section 5:

1. EPW was configured to read the previously obtained electron-phonon matrix elements in Wannier representation and the derivatives of the self-consistent-field potential to interpolate the matrix elements to the specified fine **k**- and **q**-grids.

2. The polaron equations were solved iteratively with a maximum of 500 iterations, starting from a Gaussian wave function with $\sigma = 10\, a_0$, which is approximately the lattice constant. The convergence thresholds were set to $10^{-4}\, a_0$ for the maximum displacement difference $\Delta\tau_{\kappa\alpha p}$ between iterations, and to 10^{-6} Ry for the eigenvalues of the effective polaron Hamiltonian from Eq. (5.24).

Electron polaron calculations were carried out for supercells of size $3\times3\times3$ to $28\times28\times28$ unit cells, with increments varying from 1 to 2 unit cell lengths. The data points for supercell sizes of $20 \times 20 \times 20$ to $28 \times 28 \times 28$ unit cells were considered to be in the linear regime. These were used for extrapolation to infinite supercell size via a linear least-squares fit in order to apply a Makov-Payne correction [9, 36, 28].

8.2.2. Hole Polaron

Wannierization

For the hole polaron, which arises from removing an electron from the top of the highest valence band, only the top valence bands of LiF were assumed to contribute. Therefore, only bands 3 to 5, which form a composite group, were considered [28]. The initial projection for Wannierization was chosen as fluorine's p-orbital, based on the PDOS of the top three valence bands, shown in Fig. 9.12. Since the top three valence bands form a composite group, no disentanglement or frozen energy windows were applied. All other parameters were chosen identical to those in the Wannierization of the conduction band.

Electron-Phonon Matrix Interpolation and Polaron Calculations

Apart from the polaron type, the EPW calculations were parameterized identically as for the electron polaron [28]. They were performed for supercell sizes ranging from $3 \times 3 \times 3$ to $24 \times 24 \times 24$ unit cells.

8.2.3. Hole Polaron with Anharmonic v.s. Harmonic Phonons

The objective of the following set of calculations was to investigate the influence of anharmonic phonons, calculated from SSCHA, on hole polaron formation. The DFT calculations for the numerous ionic configurations required in a SSCHA minimization, combined with the high computational cost of a supercell calculation, demanded a reduction of the supercell size to $6 \times 6 \times 6$. For a consistent baseline to compare anharmonic results with harmonic ones, the hole polaron calculation was repeated for harmonic phonons on a $6 \times 6 \times 6$ **q**-grid. For both cases harmonic and anharmonic, all further calculations were parameterized identically to those in Subsection 8.2.2, except for the calculation and interpolation of electron-phonon matrix elements for anharmonic phonons, which was based on the auxiliary interatomic force constants obtained from the SSCHA minimization.

SSCHA Minimization

Neglecting quantum and thermal fluctuations in the crystalline structure of LiF, the centroids $\boldsymbol{\mathcal{R}}$ were clamped at the equilibrium positions $\boldsymbol{\tau}^0_{\kappa p}$, so that the minimization was performed with respect to the auxiliary force constants $\boldsymbol{\Phi}$ only. The SSCHA minimization workflow for obtaining anharmonic contributions to the dynamical matrix involved the following steps:

1. The SSCHA workflow was initialized from the dynamical matrix obtained from a self-consistent DFT calculation on a $12 \times 12 \times 12$ **k**-grid, with a cutoff of 100 Ry and a convergence threshold of 10^{-16} Ry, followed by a DFPT phonon calculation on a $6 \times 6 \times 6$ **q**-grid with a convergence threshold of 10^{-14} Ry.

2. The sampling of the initial ensemble was performed by drawing 200 configurations of $6 \times 6 \times 6$ supercells at zero temperature. For each configuration, a self-consistent DFT calculation was performed to obtain the BO energies and forces. For efficiency, these self-consistent calculations were carried out with a cutoff energy of 60 Ry, a convergence threshold of 10^{-6} Ry for the total energy, and a single **k**-point, the $\boldsymbol{\Gamma}$-point.

3. Based on the BO energies and forces from these configurations, a SSCHA minimization was performed using preconditioned gradient descent with a minimum step of 0.05, a convergence threshold of 10^{-5}, and a minimum Kong-Liu ratio of 0.5. After 8 steps, the number of effective samples degraded significantly, with the

Kong-Liu ratio falling below 0.5, terminating the minimization for the first set of configurations.

4. To continue the minimization, the updated ensemble, represented by the updated auxiliary interatomic force constants, was sampled. At this point, the free energy showed signs of convergence, as visualized in Fig. 9.21, prompting an increase in the sample size to 800 for obtaining more precise final results. The self-consistent DFT calculations for the new set of configurations were performed with the same parameters as for the first sample.

5. A second SSCHA minimization was started from the BO energies and forces of the new sample. The minimization fully converged, yielding the final interatomic force constants, including anharmonic contributions.

The bubble correction for converting the auxiliary force constants into fully physically meaningful force constants was omitted, as the auxiliary force constants should already provide a good approximation for LiF, a material composed of relatively light elements [31].

Electron-Phonon Matrix Interpolation and Polaron Calculations

The interatomic force constants obtained from the SSCHA minimization, specifically the corresponding phonon frequencies and normal modes of vibration, entered the polaron calculation workflow in the calculation and interpolation of electron-phonon matrix elements. The monochromatic derivatives $\partial_{\kappa\alpha,\mathbf{q}} v_{\mathrm{SCF}}(\mathbf{r})$ were reused from the DFPT phonon calculation, which was already done for the hole polaron base line calculation using harmonic phonons on a $6 \times 6 \times 6$ $\mathbf{q}$-grid. The polaron calculations were performed for supercell sizes ranging from $20 \times 20 \times 20$ to $24 \times 24 \times 24$, well within the linear regime for the hole polaron. Again, the Makov-Payne correction was applied to extrapolate to infinite supercell size.

Chapter 9

Results and Discussion

This chapter presents the results of electron and hole polaron calculations for LiF using both harmonic and anharmonic phonons. It begins with a discussion of preparatory calculations in Section 9.1, followed by the results of electron and hole polaron calculations based on harmonic phonons in Sections 9.2 and 9.3, respectively. In Section 9.4, the anharmonic phonon dispersion, obtained through SSCHA minimization, is presented along with the results of subsequent hole polaron calculations based on SSCHA phonons. Finally, the results for hole polaron formation based on both anharmonic and harmonic phonons, are compared and discussed in Subsection 9.4.3.

9.1. Preparatory Calculations

A relaxation calculation for LiF yields a lattice constant of $a = 7.674\,a_0$, closely matching the experimental value of $a = 7.597\,a_0$, as reported in Ref. [40]. Fig. 9.1 presents the DFT band structure of LiF, revealing a band gap of $\Delta E = 8.899\,\text{eV}$, consistent with LiF's classification as an insulator. The calculated band gap shows good agreement with the known DFT band gap, $\Delta E = 8.94\,\text{eV}$, but, as expected, significantly underestimates the experimental value of $\Delta E = 14.20\,\text{eV}$ [41]. The top three valence bands occupy a common energy region and exhibit degeneracy. They form a composite band group as a gap of $\Delta E' = 16.287\,\text{eV}$ separates them from the lower valence bands.

The DFPT-calculated phonon dispersion for LiF consists of three acoustic and three optical branches, as shown in Fig. 9.2, along with experimental data at the high-symmetry points **L**, **Γ**, and **X** from Ref. [42]. All experimental data points exhibit slightly higher energies compared to the DFPT-calculated dispersion.

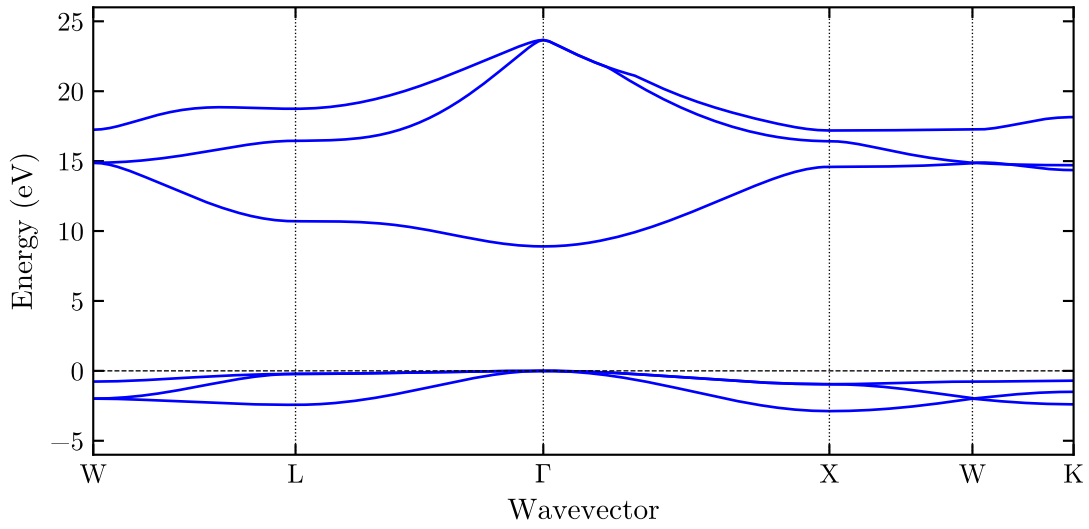

Fig. 9.1.: DFT band structure of LiF showing degeneracies in the top three valence bands, a DFT band gap of $\Delta E = 8.899\,\text{eV}$, and a crossing of the conduction band with the next higher band near the **W** high-symmetry point.

9.2. Electron Polaron

9.2.1. Analysis and Wannierization of the Conduction Band

Fig. 9.3 shows the conduction band of LiF and its PDOS in the left and right panels, respectively. It reveals that the atomic orbitals that contribute to the very bottom of the conduction band, relevant for electron polaron formation, are the Li s-orbital and the F s-orbital. The spread of MLWFs for the conduction band, determined using these two different orbitals as the initial projection, are $\sigma_{\text{Li-}s} = 17.7917\,a_0$ and $\sigma_{\text{F-}s} = 6.5116\,a_0$, respectively. For further calculations, only the MLWF originating from the F-centered s-orbital is used, as it exhibits the smaller spread. This choice is further supported by the visualization in Fig. 9.5, which shows isosurface plots of both MLWFs. Fig. 9.4 shows the Wannier interpolation for the conduction band, which is congruent to the DFT band structure in most regions. However, near the degeneracy with the next higher band around the **W** high-symmetry point, the Wannier interpolation deviates from the DFT band structure. This is acceptable, as the conduction-band states in this higher energy region are insignificant to electron polaron formation. The results visualized in Fig. 9.7 *a posteriori* justify this assessment.

The congruence of the DFPT and Fourier-interpolated phonon dispersions, confirmed in

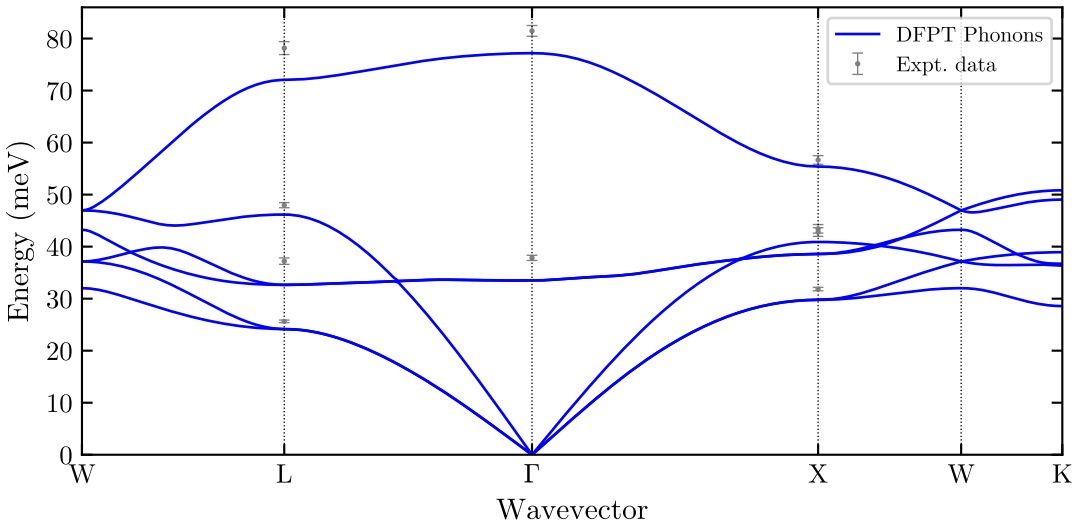

Fig. 9.2.: DFPT phonon dispersion of LiF showing degeneracies in the transverse acoustic (TA) and transverse optical (TO) branches near the **Γ** high-symmetry point. Experimental data from Ref. [42] is shown at the **L**, **Γ** and **X** high-symmetry points.

Fig. A.1 in Appendix A, is crucial for the validity of the interpolated phonon frequencies, polarization vectors, and electron-phonon matrix elements. Fig. A.4 illustrates the decay of the Hamiltonian, the dynamical matrix, and the electron-phonon matrix elements in Wannier representation, demonstrating convergence within the $12 \times 12 \times 12$ supercell and verifying the fidelity of the Wannierization step.

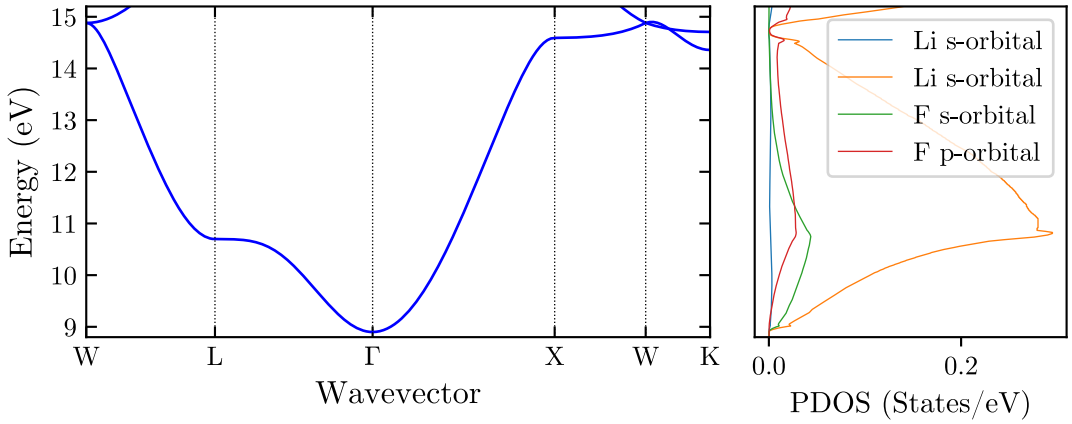

Fig. 9.3.: Band structure and PDOS of the conduction band of LiF. The left panel shows the conduction-band structure along the high-symmetry path in the BZ, while the right panel represents the corresponding PDOS, indicating the contributions from *s*- and *p*-orbitals of Li and F.

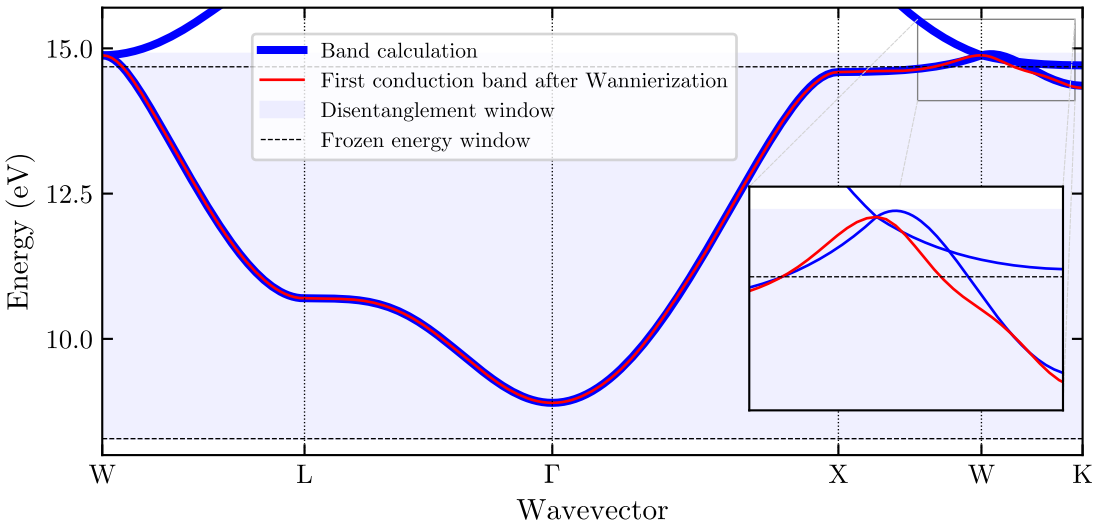

Fig. 9.4.: Wannier interpolation of the conduction band, shown in red, overlaid on the DFT band structure in blue. The disentanglement window is represented by the light-purple shaded area, and the frozen energy window borders are marked by dashed lines. The inset magnifies the region near the **W** high-symmetry point, featuring the band crossings where the interpolated band structure shows deviations from the DFT band structure.

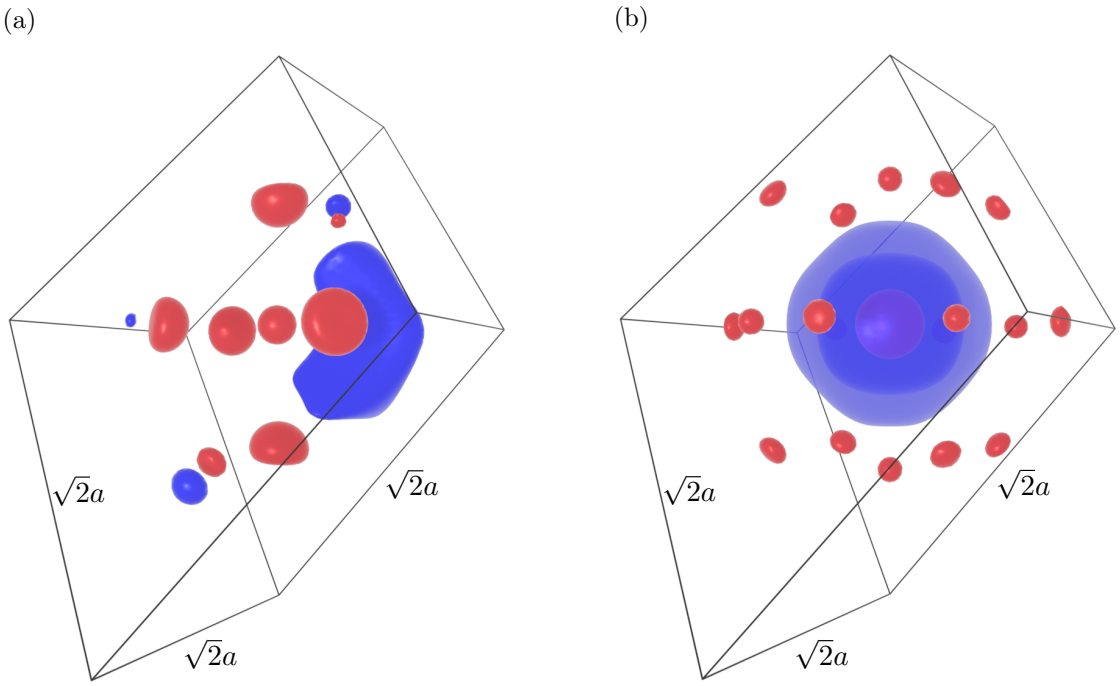

Fig. 9.5.: Isosurface plots of MLWFs of the conduction band of LiF, depicted within a $2 \times 2 \times 2$ FCC supercell and generated using different initial projections. Positive isosurfaces are depicted in red, while negative ones are shown in blue. (a) Initial projection onto the Li-centered s-orbital. (b) Initial projection onto the F-centered s-orbital.

9.2.2. Electron Polaron Formation

Fig. 9.6 shows the formation energies and eigenvalues obtained from electron polaron calculations in the upper and lower panels, respectively. It shows data for various supercell sizes, ranging from $3 \times 3 \times 3$ to $28 \times 28 \times 28$. Formation energies are positive for smaller supercells, indicating an unfavorable energy balance compared to a conduction band electron. In contrast, the formation energies calculated for larger supercells, starting from $13 \times 13 \times 13$ in the available data, are negative, making polaron formation energetically favorable. Furthermore, the data points from supercell sizes $20 \times 20 \times 20$ to $28 \times 28 \times 28$, which lie well within the linear regime, are linearly extrapolated to an infinite supercell size. As shown in Fig. 9.6, the extrapolated formation energy is $\Delta E_f = -0.267\,\text{eV}$ with a corresponding eigenvalue of $\varepsilon = -0.935\,\text{eV}$. These results differ by approximately 16% from $\Delta E_f = -0.23\,\text{eV}$ and $\varepsilon = -0.80\,\text{eV}$, reported in Ref. [10], but show excellent agreement with $\Delta E_f = -0.268\,\text{eV}$, reported in Ref. [43]. Since the presented results and those from Refs. [10] and [43] are based on the same $\mathbf{q}$- and $\mathbf{k}$-grids of $12 \times 12 \times 12$, any difference is most likely related to the Wannierization of the conduction band. However, the Wannierization parameters used in Refs. [10] and [43] are unknown, making it difficult to pinpoint the cause of the deviation.

Figs. 9.7 and 9.8 provide a visualization of the contributions from Kohn-Sham orbitals and phonon modes to the formation of the polaron wave function and the corresponding lattice distortion, respectively. The significant contributions to the electron polaron wave function are found in a limited region of $\mathbf{k}$-space around the conduction-band minimum, resulting in a large polaron wave function in real space. The same rationale applies to the phonon contributions, which are narrowly distributed around the $\mathbf{\Gamma}$ high-symmetry point and therefore correspond to a lattice displacement spread across several unit cells in real space. Fig. 9.9 shows an isosurface plot of the electron polaron wave function, viewed along [100], while Fig. 9.11 aligns the electron polaron's probability density $|\psi|^2$, shown in the upper panel, with its corresponding ionic displacements in the lower panel, taken from a line through the polaron center in the [001] direction. These graphical representations closely resemble the corresponding depictions in Ref. [9].

The lattice distortion generated by the polaron is summarized in Fig. 9.10. It shows the averaged displacements, binned by radial distance from the polaron center. The radial binning is justified by the approximate spherical symmetry of the polaron and the high degree of radial alignment of the displacement vectors, verified by projecting them onto radial vectors connecting the polaron center and the respective ionic positions. Fig. 9.10 thus reveals that the ionic displacements, associated with the electron polaron, are generally outward-pointing for both atomic species in LiF.

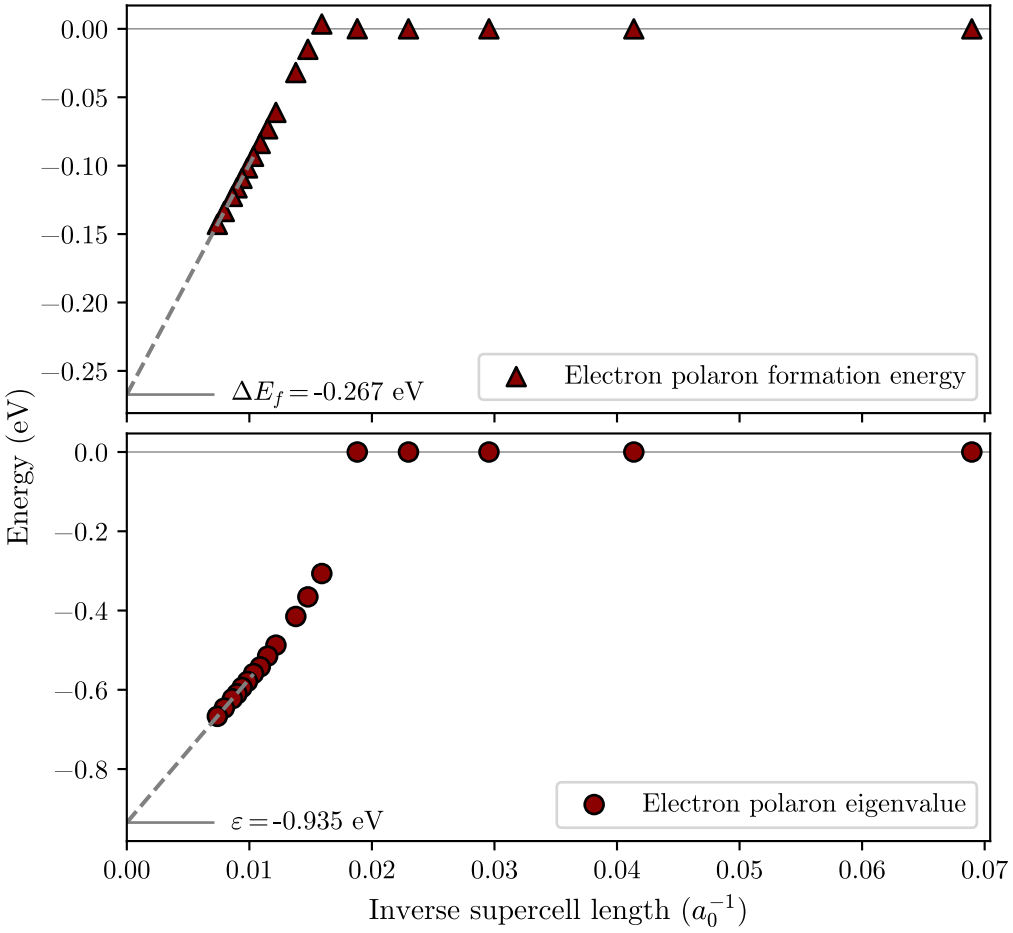

Fig. 9.6.: Electron polaron formation energies and eigenvalues for different inverse supercell sizes are shown in the top and bottom panels as dark-red triangles and discs, respectively. The calculations were performed for supercells ranging from $3 \times 3 \times 3$ to $28 \times 28 \times 28$ unit cells in size. The gray dashed lines in both panels show the Makov-Payne extrapolations to infinite supercell size, which are based on data points ranging from $20 \times 20 \times 20$ to $28 \times 28 \times 28$ unit cells, and fitted using the least-squares method. The extrapolated values are $\Delta E_f = -0.267\,\text{eV}$ for the formation energy and $\varepsilon = -0.935\,\text{eV}$ for the eigenvalue.

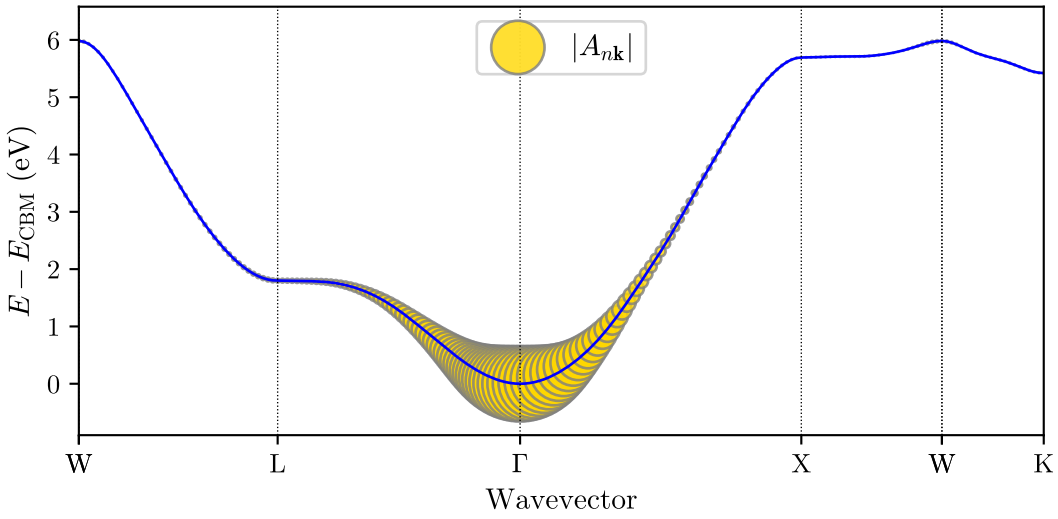

Fig. 9.7.: Visualization of coefficients $A_{n\mathbf{k}}$ from an electron polaron calculation in a $24 \times 24 \times 24$ supercell. The magnitudes of the coefficients are represented by the radii of the yellow discs, overlaid on the DFT conduction-band structure of LiF. They illustrate the contributions of conduction-band Kohn-Sham orbitals to the polaron wave function.

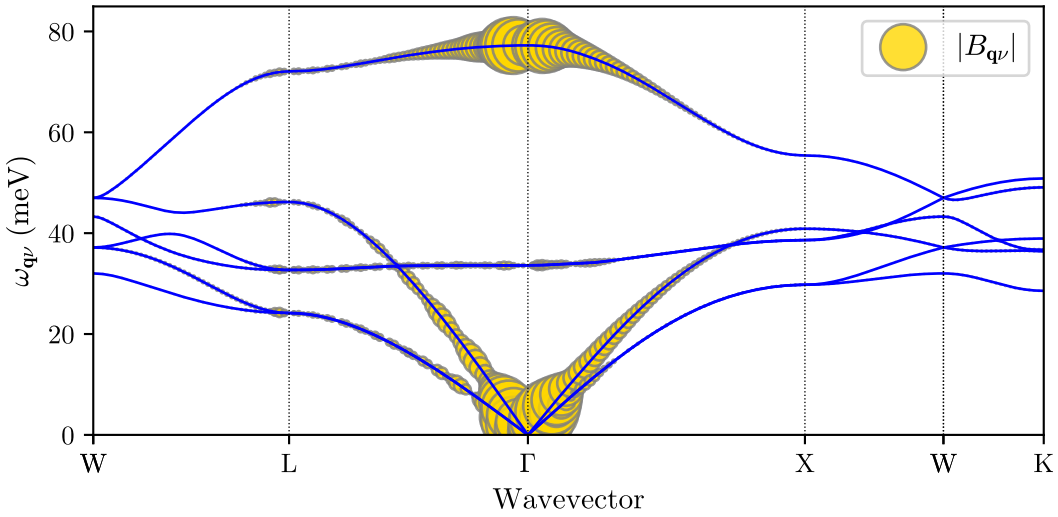

Fig. 9.8.: Visualization of coefficients $B_{\mathbf{q}\nu}$ from an electron polaron calculation in a $24 \times 24 \times 24$ supercell. The magnitudes of the coefficients are represented by the radii of the yellow discs, overlaid on the DFPT phonon dispersion. They illustrate the contributions of phonon modes to the lattice displacements associated with the polaron.

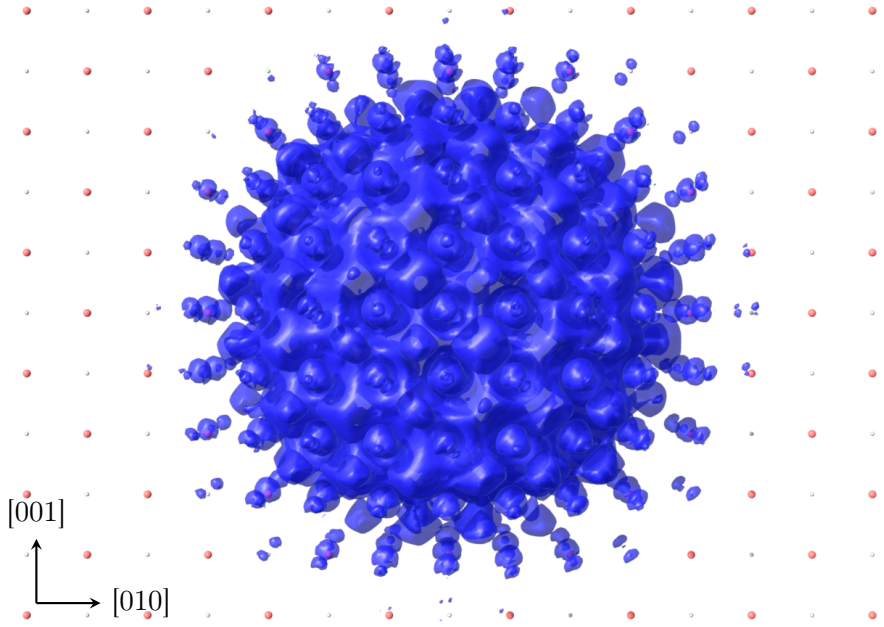

Fig. 9.9.: Isosurface plot of the electron polaron wave function from a polaron calculation in a $24 \times 24 \times 24$ supercell, along [100], shown in blue. The red and gray beads represent F and Li ions, respectively, illustrating a layer of LiF intersecting the polaron center.

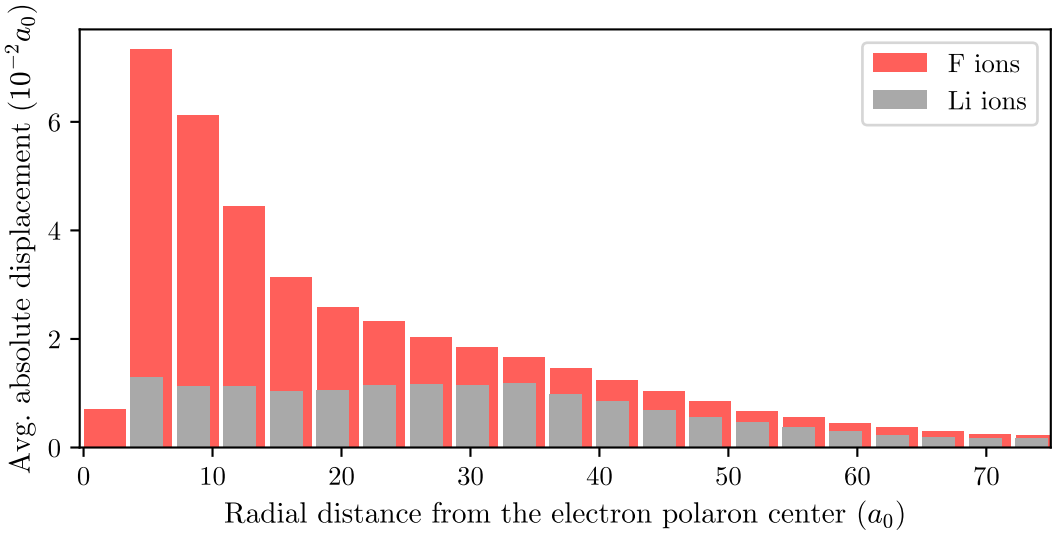

Fig. 9.10.: Average displacements associated with the electron polaron from a polaron calculation in a $24 \times 24 \times 24$ supercell, binned by radial distance from the polaron center. The red and gray bars represent the average radial displacements of the F and Li ions, respectively.

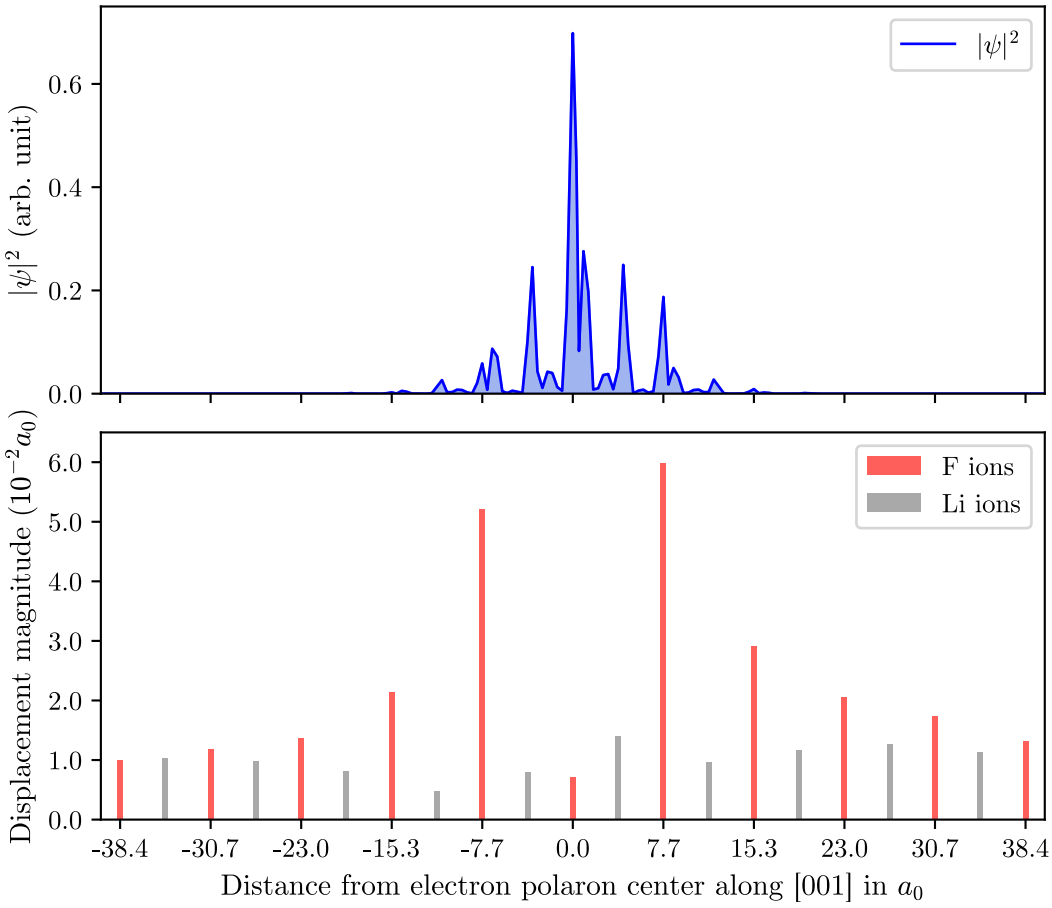

Fig. 9.11.: Probability density of the electron polaron wave function and corresponding ionic displacement magnitudes from a polaron calculation in a $24 \times 24 \times 24$ supercell. The top panel shows $|\psi|^2$ along the [001] direction, intersecting the polaron center. The bottom panel visualizes the ionic displacements associated with the hole polaron along the same path. Red and gray bars represent the displacements of F and Li ions, respectively.

9.3. Hole Polaron

9.3.1. Analysis and Wannierization of the Top Three Valence Bands

Fig. 9.12 shows the top three valence bands of LiF and the corresponding PDOS in the left and right panels, respectively. The p-orbital of the F-atom clearly dominates the energy range of this composite group. MLWFs from F-centered p-orbitals as initial projectors are collectively visualized in Fig. 9.13 and exhibit spreads of $\sigma_{\text{F-}p_x} = \sigma_{\text{F-}p_y} = \sigma_{\text{F-}p_z} = 0.3127\, a_0$. Fig. 9.14 shows the Wannier interpolation of the top valence bands based on the F-centered MLWFs. It is overlaid on the DFT band structure, showing perfect congruence, thereby indicating a high quality of the MLWFs for the valence bands and their corresponding Wannier gauge. Consequently, the decay of the Hamiltonian, dynamical matrix, and electron-phonon matrix elements, visualized in Fig. A.5 in Appendix A, shows strong convergence within the $12 \times 12 \times 12$ supercell.

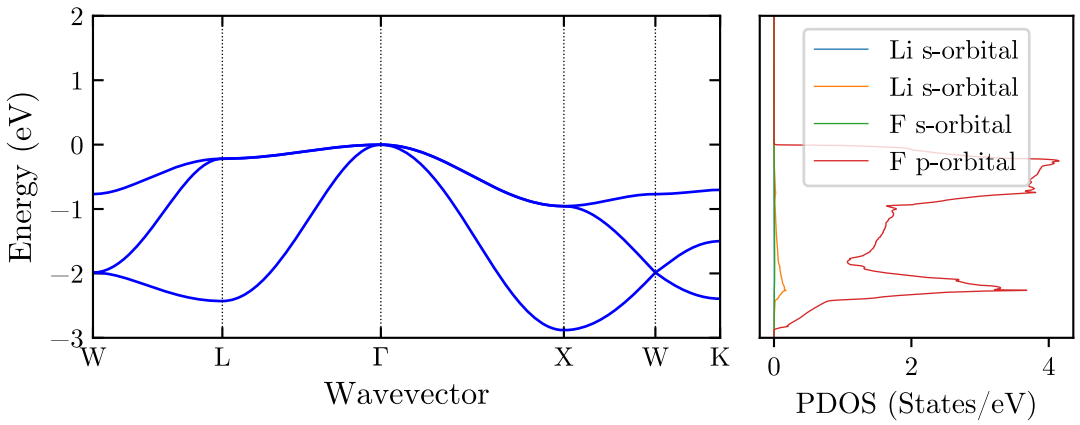

Fig. 9.12.: Band structure and PDOS of the top three valence bands of LiF. The left panel shows the composite band group's structure along the high-symmetry path in the BZ, while the right panel represents the corresponding PDOS, indicating the contributions from s- and p-orbitals of Li and F.

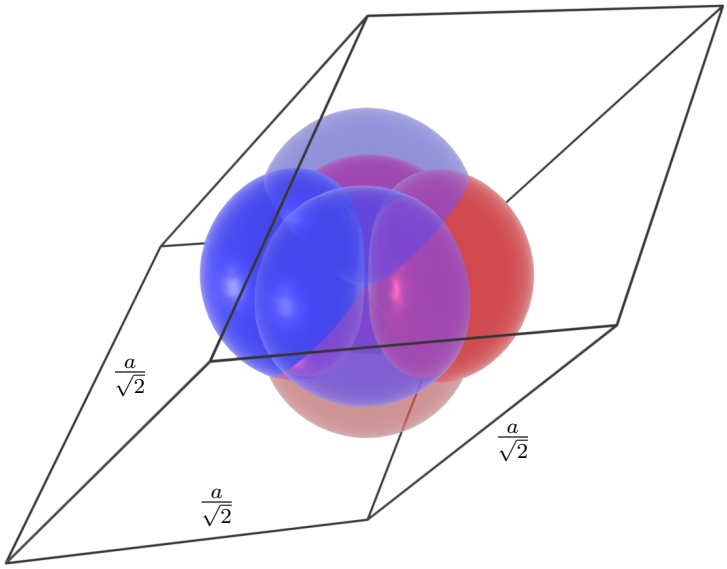

Fig. 9.13.: Isosurfaces of the F-centered MLWFs of the top three valence bands of LiF inside the primitive FCC unit cell. Positive isosurfaces are depicted in red, while negative ones are shown in blue. The isosurfaces of the three MLWFs, each with p-orbital character and different orientation, are overlaid in the plot.

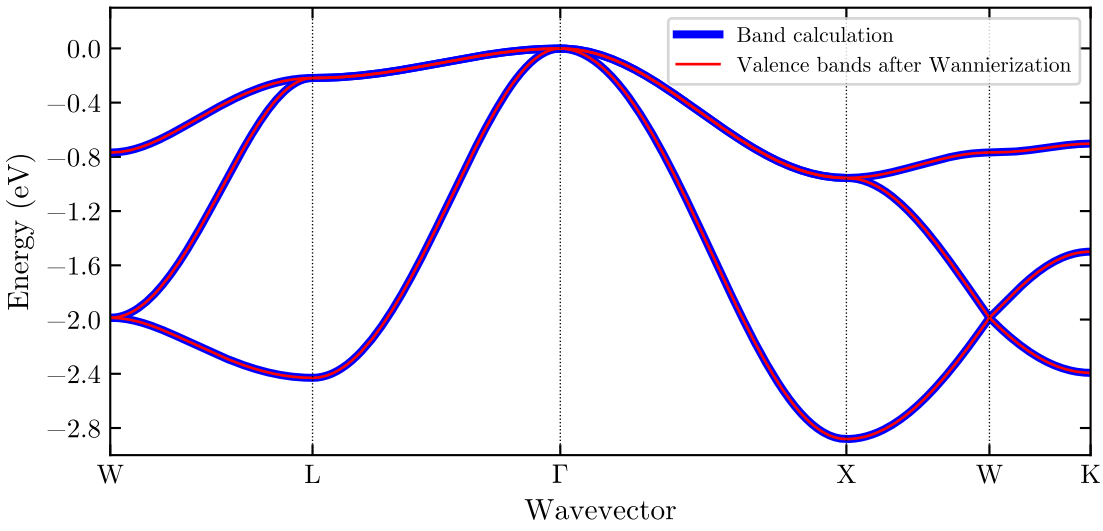

Fig. 9.14.: Wannier interpolation of the top three valence bands, shown in red, overlaid on the DFT band structure in blue.

9.3.2. Hole Polaron Formation

Hole polaron formation energies and eigenvalues for various supercell sizes, ranging from $3 \times 3 \times 3$ to $24 \times 24 \times 24$, are visualized in Fig. 9.15 in the upper and lower panels, respectively. The extrapolated formation energy and eigenvalue for a hole polaron in an infinite supercell, fitting the data points from supercell sizes $11 \times 11 \times 11$ to $24 \times 24 \times 24$, are $\Delta E_f = -1.976\,\text{eV}$ and $\varepsilon = 4.750\,\text{eV}$, respectively. These results exhibit a deviation of less than 1% from those reported in Refs. [9] and [43].

The contributions of Kohn-Sham orbitals and phonon modes to the formation of the polaron wave function and the associated lattice distortion are visualized in Figs. 9.16 and 9.17, respectively. The evenly distributed contributions of Kohn-Sham orbitals across a wide range of wave vectors correspond to a highly localized polaron wave function. This reasoning also applies to the evenly distributed phonon contributions in the LO branch along the high-symmetry path, which correspond to a very localized lattice distortion, characterizing the hole polaron in LiF as a small polaron.

Fig. 9.18 shows an isosurface plot of the hole polaron wave function, while Fig. 9.20 aligns the probability density $|\psi|^2$, shown in the top panel, with the associated ionic displacements in the lower panel, taken from a line through the polaron center in the [001] direction. Both graphical representations closely resemble the corresponding depictions in Ref. [10].

The lattice distortion associated with the hole polaron is summarized in Fig. 9.19, which shows the averaged displacements binned by radial distance from the polaron center. Although the hole polaron lacks spherical symmetry, binning by radial distance is justified due to its small size. This assumption is further supported by the strict radial alignment of the ionic displacements, which is even more pronounced than in the electron polaron case. While the electron polaron induces outward displacements in both atomic species, the hole polaron distinctly polarizes the material: Li^+ ions are repelled by the positively charged electron hole, whereas F^- ions are attracted toward the polaron center. This behavior can be understood by considering the small size of the hole polaron wave function, approximately acting as point charge, even in its immediate vicinity.

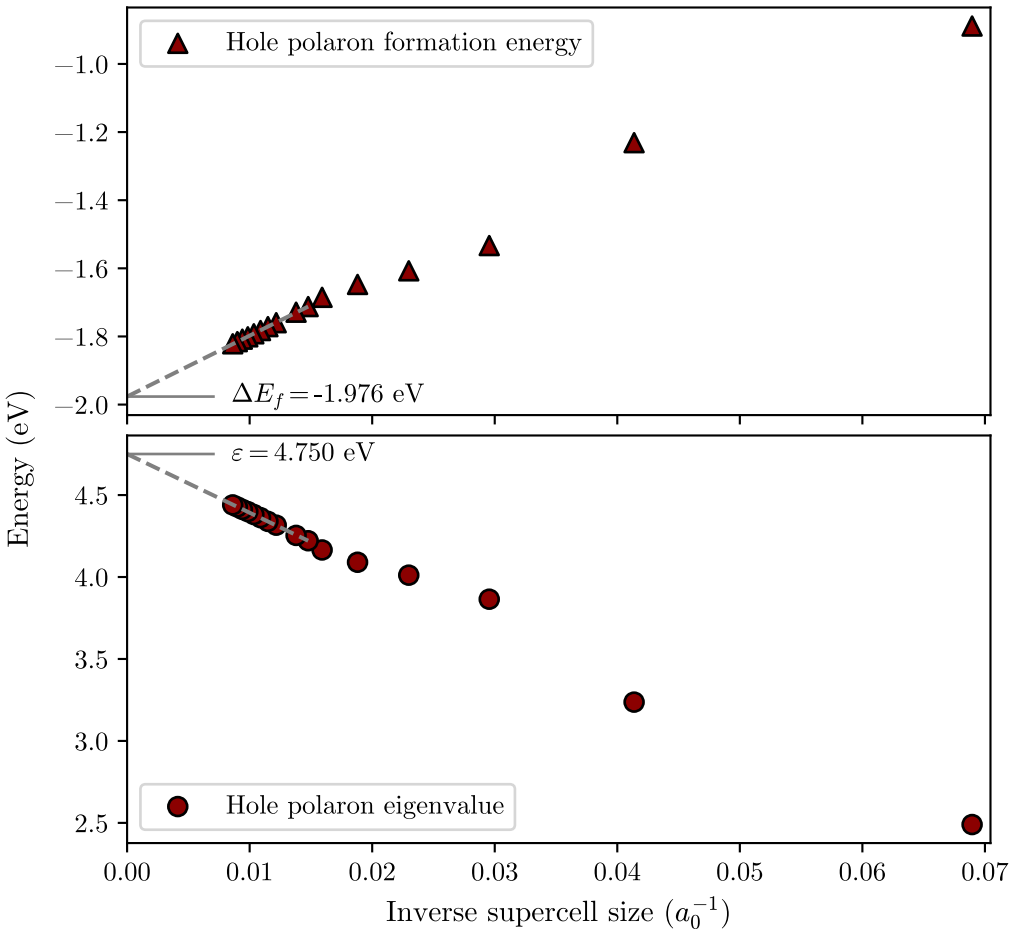

Fig. 9.15.: Hole polaron formation energies and eigenvalues for different inverse supercell sizes are shown in the top and bottom panels as dark-red triangles and discs, respectively. The calculations were performed for supercells ranging from $3 \times 3 \times 3$ to $24 \times 24 \times 24$ unit cells in size. The gray dashed lines in both panels show the Makov-Payne extrapolations to infinite supercell size, which are based on data points ranging from $11 \times 11 \times 11$ to $24 \times 24 \times 24$ unit cells, and fitted using the least-squares method. The extrapolated values are $\Delta E_f = -1.976\,\text{eV}$ for the formation energy and $\varepsilon = 4.750\,\text{eV}$ for the eigenvalue.

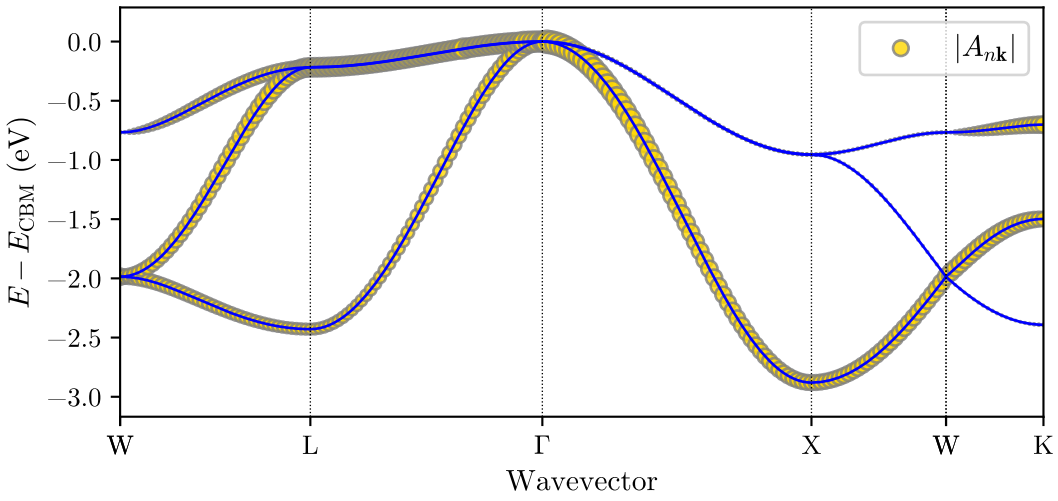

Fig. 9.16.: Visualization of coefficients $A_{n\mathbf{k}}$ from a hole polaron calculation in a $17 \times 17 \times 17$ supercell. The magnitudes of the coefficients are represented by the radii of the yellow discs, overlaid on the DFT band structure of the top three valence-bands of LiF. They illustrate the contributions of valence-band Kohn-Sham orbitals to the polaron wave function.

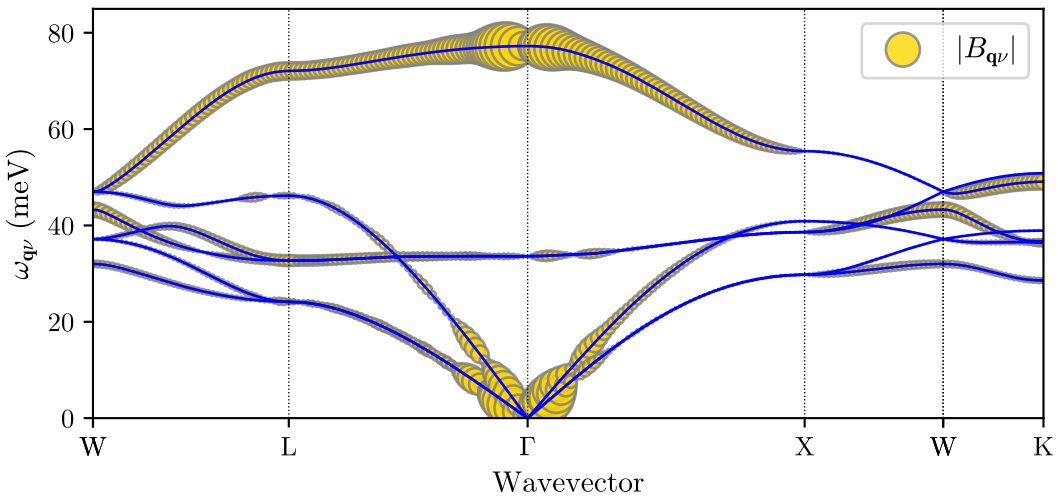

Fig. 9.17.: Visualization of coefficients $B_{\mathbf{q}\nu}$ from a hole polaron calculation in a $17 \times 17 \times 17$ supercell. The magnitudes of the coefficients are represented by the radii of the yellow discs, overlaid on the DFPT phonon dispersion. They illustrate the contributions of phonon modes to the lattice displacements associated with the polaron.

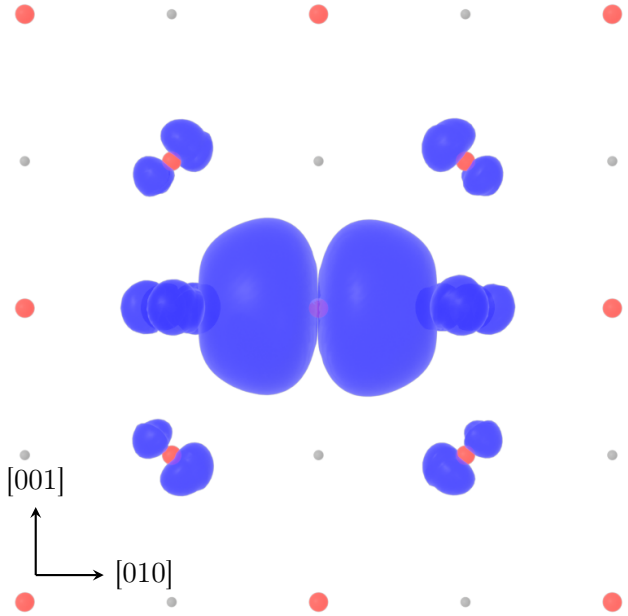

Fig. 9.18.: Isosurface plot of the hole polaron wave function from a polaron calculation in a $17 \times 17 \times 17$ supercell, along [100], shown in blue. The red and gray beads represent F and Li ions, respectively, illustrating a layer of LiF intersecting the polaron center.

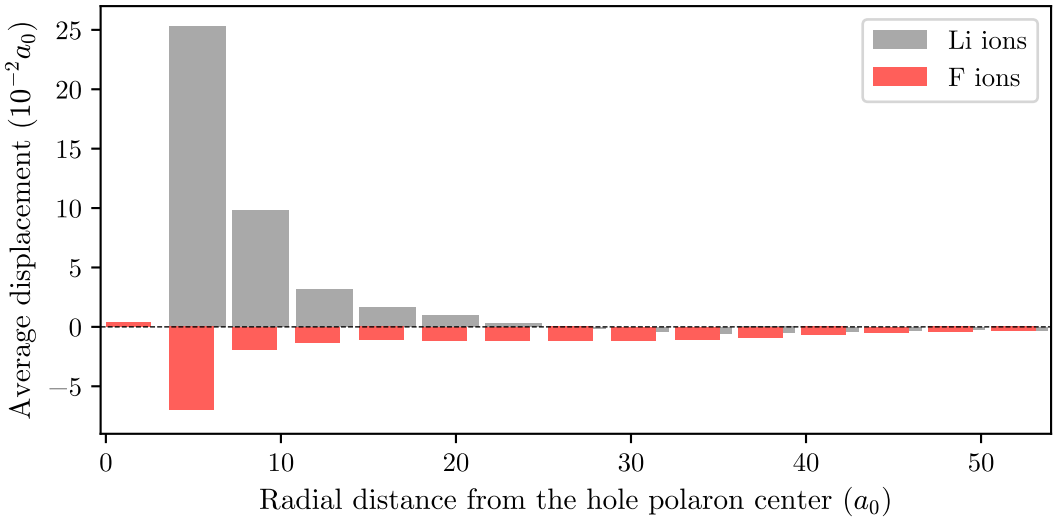

Fig. 9.19.: Average displacements associated with the hole polaron from a polaron calculation in a $17 \times 17 \times 17$ supercell, binned by radial distance from the polaron center. The red and gray bars represent the average radial displacements of the F and Li ions, respectively.

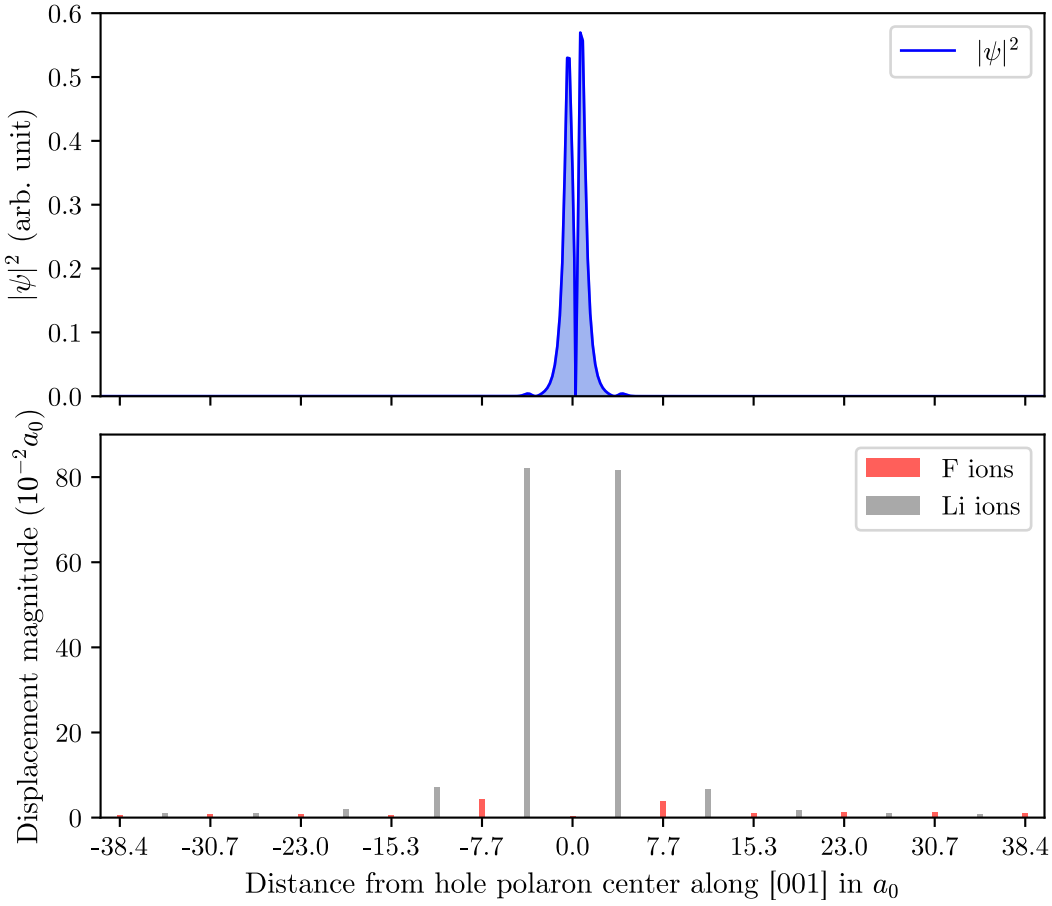

Fig. 9.20.: Probability density of the hole polaron wave function and corresponding ionic displacement magnitudes from a polaron calculation in a $24 \times 24 \times 24$ supercell. The top panel shows $|\psi|^2$ along the [001] direction, intersecting the polaron center. The bottom panel visualizes the ionic displacements associated with the hole polaron along the same path. Red and gray bars represent displacements of F and Li ions, respectively.

Tab. 9.1 summarizes the eigenvalues and formation energies for electron and hole polarons, as presented in Subsections 9.2.2 and 9.3.2, respectively.

Tab. 9.1.: Summary of eigenvalues, as well as formation energies with their electronic and phonon contributions, for electron and hole polarons. The listed quantities were obtained through Makov-Payne extrapolation to an infinite supercell size.

Quantity	Electron Polaron	Hole Polaron
Eigenvalue (eV)	−0.935	4.750
Formation Energy (eV)	−0.267	−1.976
Phonon part (eV)	−0.668	−2.773
Electron part (eV)	0.401	0.797

9.4. Hole Polaron with Harmonic vs. Anharmonic Phonons

This section begins by presenting the anharmonic phonon dispersion for LiF, obtained using SSCHA, which is subsequently utilized for a hole polaron calculation. The results are then compared to those from a hole polaron calculation using harmonic phonons, with a BZ sampling corresponding to the supercell employed in the SSCHA minimization. Finally, the differences between the anharmonic and harmonic calculations are analyzed and further broken down by individual phonon branches of LiF.

9.4.1. SSCHA Minimization

The SSCHA minimization took 18 minimization steps until convergence, while the ensemble needed to be sampled two times in order for the Kong-Liu ratio to stay above 1/2. Fig. 9.21 shows the free energy, the effective sample size, and the gradients with respect to the auxiliary force constants and centroid positions at each minimization step in separate panels. Fig. 9.22 shows the evolution of the phonon frequencies during the SSCHA minimization, starting from the harmonic phonon frequencies obtained from a $6 \times 6 \times 6$ **q**-grid. The resulting anharmonic phonon dispersion is shown in Fig. 9.23, together with the previously obtained harmonic phonon dispersion for comparison.

9.4.2. Convergence Tests after Wannierization

The MLWFs and the associated Wannier gauge for calculating $g_{mn\kappa\alpha}(\mathbf{R}_{p_\mathbf{k}}, \mathbf{R}_{p_\mathbf{q}})$ and $H_{nm}(\mathbf{R}_{p_\mathbf{k}})$, are identical to the ones used in Section 9.3. However, the harmonic dynamical matrix is taken from a DFPT calculation on a $6 \times 6 \times 6$ **q**-grid, while the anharmonic interatomic force constants are taken from the SSCHA minimization in a $6 \times 6 \times 6$ supercell. Figs. A.2 and A.3 in Appendix A show the interpolated phonon dispersions for harmonic phonons and anharmonic phonons, respectively. The interpolations are overlaid on the corresponding *ab initio*-calculated dispersions, demonstrating perfect congruence with them. The decay of the Hamiltonian, dynamical matrix, and the electron-phonon matrix elements in Wannier representation, for both types of phonon dispersions, are shown in Figs. A.6 and A.7 in Appendix A.

9.4.3. Hole Polaron Formation with Harmonic vs. Anharmonic Phonons

The extrapolated formation energies for the harmonic and anharmonic calculations, as shown in the upper panel of Fig. 9.24, are $\Delta E_f^{(h)} = -2.113\,\text{eV}$ and $\Delta E_f^{(a)} = -1.943\,\text{eV}$, respectively, with a difference of $\Delta E_f^{(a)} - \Delta E_f^{(h)} = 170\,\text{meV}$. It shows that hole polaron

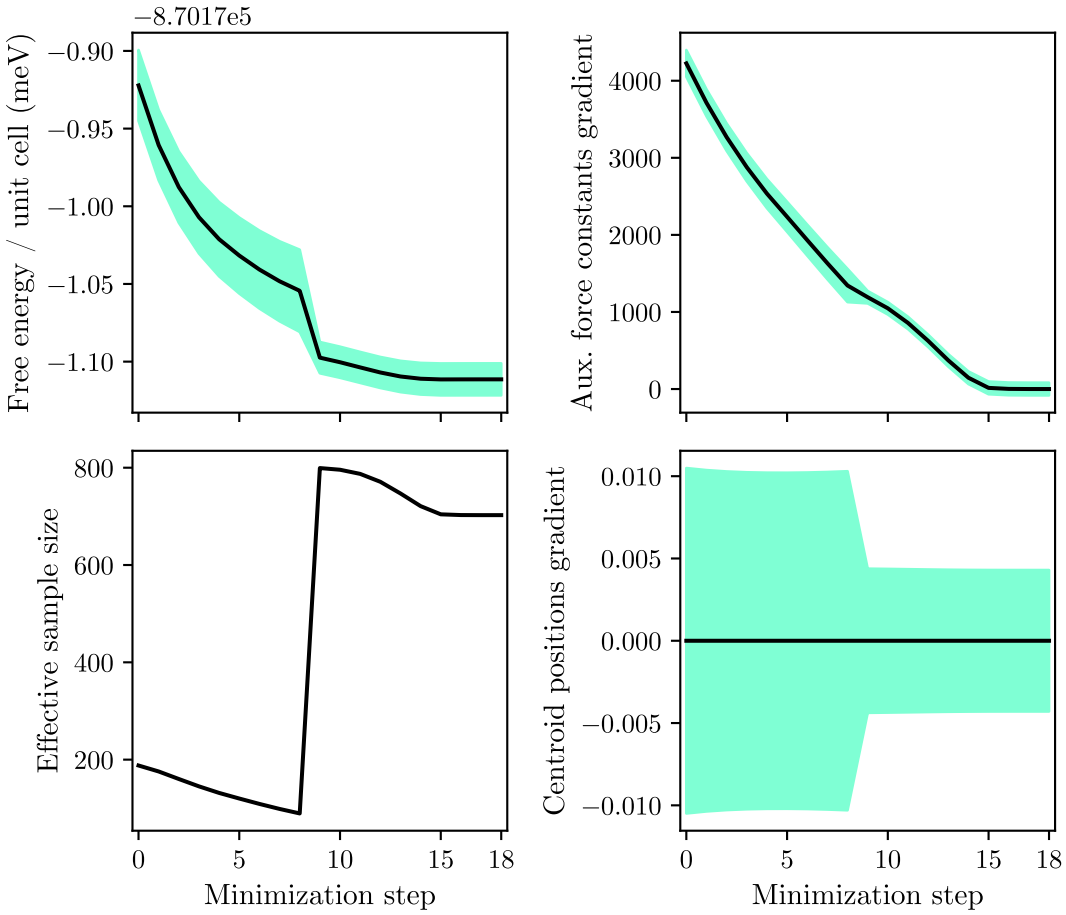

Fig. 9.21.: SSCHA free energy minimization for LiF using clamped centroids in a $6 \times 6 \times 6$ supercell. The top left panel shows the free energy of the system at each step in the minimization process, while the effective sample size is shown in the bottom left panel. Right-hand side panels display the gradients' evolution. The force constants' gradient is plotted at the top panel and the centroids' gradient, which is clamped to zero, is visualized at the bottom. Turquoise regions indicate the statistical uncertainties in all panels.

formation in LiF becomes less favorable when anharmonicity is included in the phonon dispersion, which constitutes the main result of this thesis. Furthermore, Fig. 9.24 shows the extrapolated eigenvalues in the lower panel. These are $\varepsilon^{(h)} = 5.029\,\text{eV}$ and $\varepsilon^{(a)} = 4.064\,\text{eV}$. The contributions of Kohn-Sham orbitals and phonon modes to polaron formation, as well as isosurface plots of the polaron wave functions, are shown in Figs. B.1, B.2, B.3, B.4, and B.5 in Appendix B.

Compared to Section 9.3, the coarse $6 \times 6 \times 6$ sampling of the BZ lowers the hole polaron formation energy by 173 meV for the harmonic calculation. Additionally, the convergence of matrix elements within the supercell is less pronounced for the coarse sampling. Nonetheless, the hypothesis that anharmonic effects in the phonon dispersion make polaron formation energetically less favorable remains reasonable.

As shown in Tab. 9.2, the higher polaron formation energy in the anharmonic case is mainly due to the energy difference in the phonon part. Breaking this down into contributions from individual phonon branches, as done in Tab. 9.3, reveals that the energy differences between anharmonic and harmonic contributions are all positive, with the LO branch accounting for over 78% of the differences. This is a consequence of the higher or equal phonon frequencies in the anharmonic phonon dispersion across the BZ, as indicated in Figs. 9.22 and 9.23, making ionic displacements energetically more expensive. This effect is particularly pronounced for the LO branch, which dominates the phonon contribution to hole polaron formation. Fig. 9.25 visualizes the energy differences between anharmonic and harmonic phonon contributions in the LO branch across a $\mathbf{q}$-mesh spanning the BZ. It shows that the exclusively positive differences become slightly more significant towards the $\mathbf{\Gamma}$ high-symmetry point but overall remain evenly distributed throughout the whole BZ, summing up to a total difference of $\Delta E_{\mathrm{LO}} = 0.142\,\mathrm{eV}$. As shown in Fig. 9.17, the hole polaron formation is also influenced by phonon contributions in the linear regime of the TA branches near the $\mathbf{\Gamma}$ point. However, since the harmonic and anharmonic dispersions are effectively congruent in this region, as shown in Fig. 9.23, the energy differences arising from the TA branches are negligible. Less pronounced energy differences in the TO, longitudinal acoustic (LA), and TA branches are depicted in the supplementary Figs. B.6, B.7, and B.8 in Appendix B. The combined energy difference from all branches results in a less significant negative phonon contribution in Eq. (5.27), thereby raising the polaron formation energy in the anharmonic case and making polaron formation less favorable compared to the harmonic case.

Future work could verify the presented results by using a more accurate anharmonic phonon dispersion, calculated with larger supercells or using alternative methods to SSCHA. The goal would be to compare results from such calculations with the converged hole polaron results presented in Section 9.3.

Tab. 9.2.: Comparison of energy and eigenvalue results for hole polaron calculations performed in a $24 \times 24 \times 24$ supercell with harmonic and anharmonic phonons.

Quantity	Anharmonic Phonons	Harmonic Phonons	Difference
Eigenvalue (eV)	3.680	4.736	−1.056
Formation Energy (eV)	−1.827	−1.968	0.141
Phonon part (eV)	−2.588	−2.768	0.181
Electron part (eV)	0.760	0.801	−0.040

Tab. 9.3.: Phonon energy contributions to hole polaron formation in a $24 \times 24 \times 24$ supercell, comparing values from calculations with anharmonic and harmonic phonons for each individual phonon branch. The contributions across all branches sum up to the respective phonon parts of the formation energies, as reported in Tab. 9.2. The most significant difference is observed in the LO branch, being one order of magnitude higher than the differences in the other branches.

Phonon Branch	Anharmonic Phonons	Harmonic Phonons	Difference
E_{LO} (eV)	−2.253	−2.396	0.142
E_{TO_2} (eV)	−0.048	−0.061	0.012
E_{TO_1} (eV)	−0.043	−0.053	0.010
E_{LA} (eV)	−0.138	−0.149	0.011
E_{TA_2} (eV)	−0.061	−0.066	0.004
E_{TA_1} (eV)	−0.044	−0.045	0.001
Phonon part (eV)	−2.588	−2.768	0.181

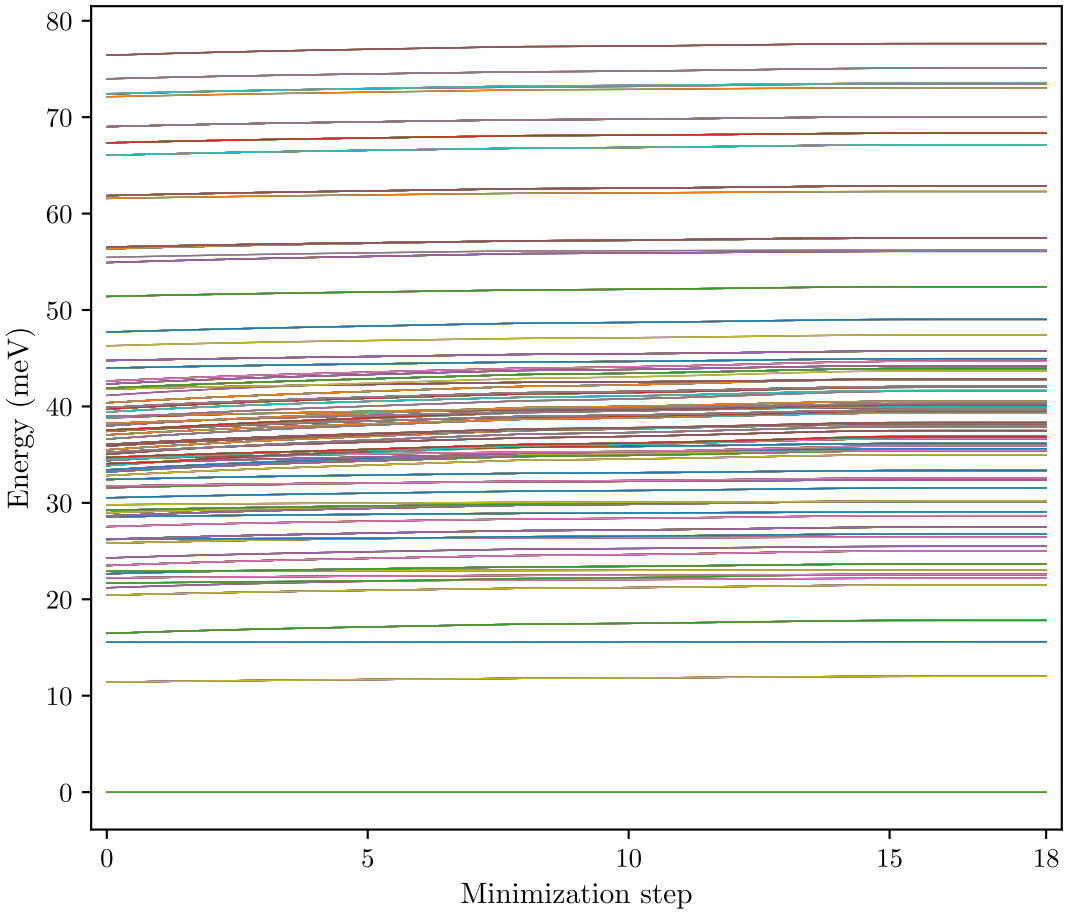

Fig. 9.22.: Evolution of phonon frequencies during SSCHA minimization using a $6 \times 6 \times 6$ supercell. Each curve shows the progression of an individual phonon mode's frequency, starting from the harmonic value obtained from a DFPT calculation on a $6 \times 6 \times 6$ **q**-grid, to the converged SSCHA result.

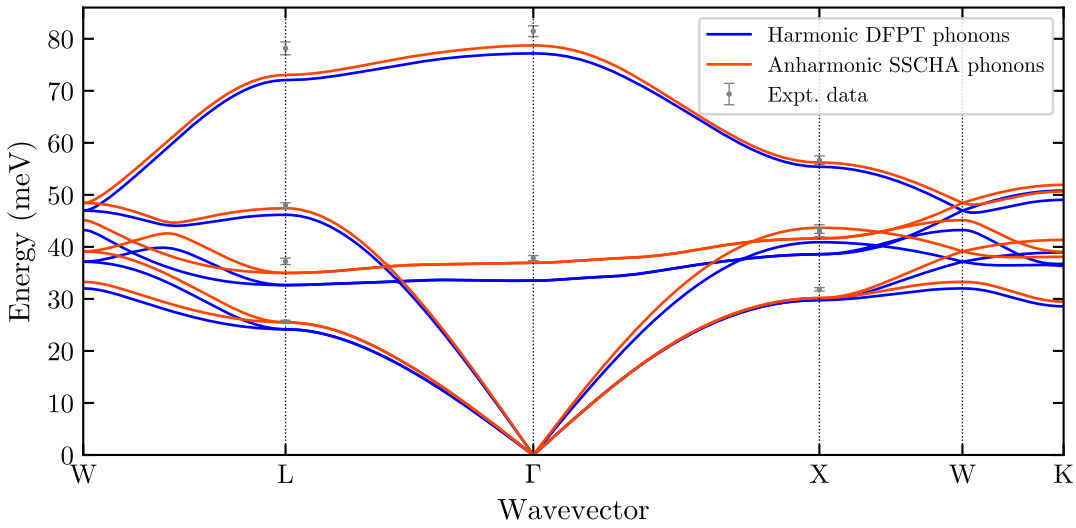

Fig. 9.23.: Comparison of DFPT and SSCHA phonon dispersions. The harmonic phonon dispersion from a DFPT calculation on a $6 \times 6 \times 6$ **q**-grid is shown in blue, while the anharmonic dispersion obtained from SSCHA minimization in a $6 \times 6 \times 6$ supercell is plotted in red. Experimental data from Ref. [42] is shown at the **L**, **Γ** and **X** high-symmetry points.

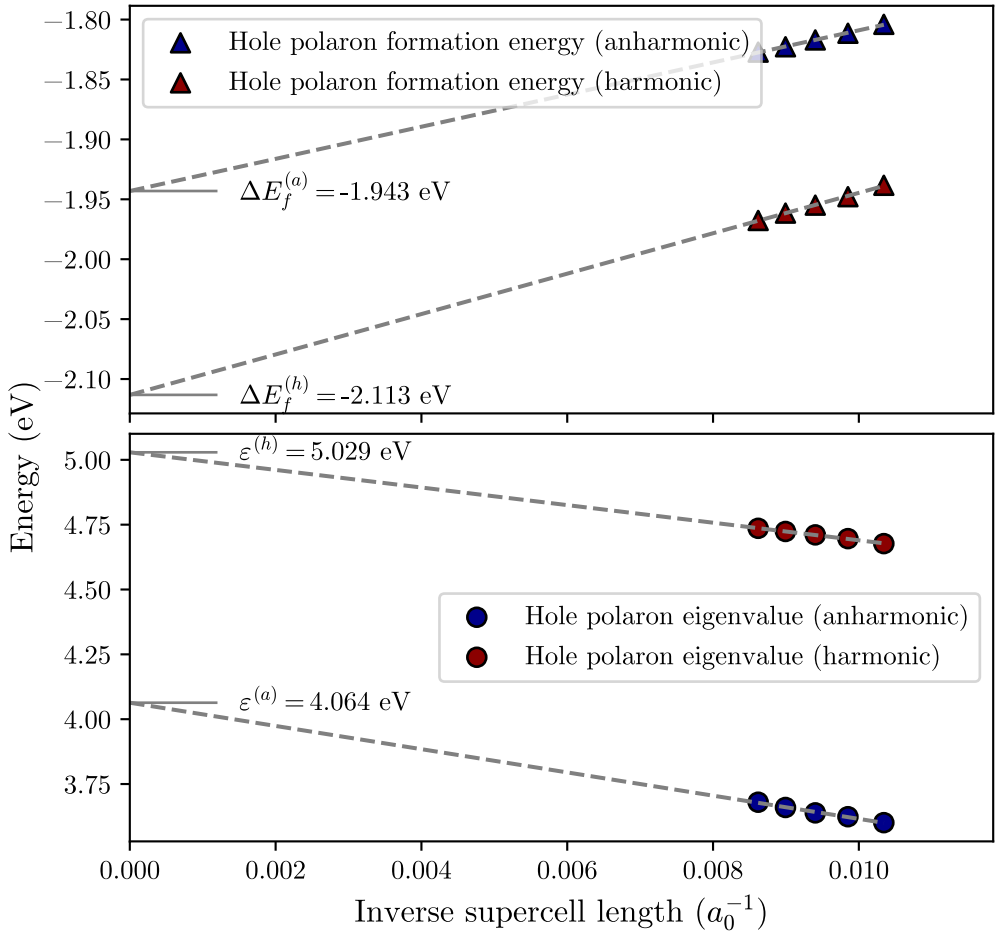

Fig. 9.24.: Hole polaron formation energies and eigenvalues for different inverse supercell sizes are shown in the top and bottom panels as triangles and discs, respectively. Results from calculations using harmonic and anharmonic phonons are represented by dark-red and dark-blue colors, respectively, for various supercell sizes ranging from $20 \times 20 \times 20$ to $24 \times 24 \times 24$. The gray dashed lines in both panels show the Makov-Payne extrapolations to infinite supercell size, which are fitted using the least-squares method. The extrapolated values are $\Delta E_f^{(h)} = -2.113\,\text{eV}$ and $\Delta E_f^{(a)} = -1.943\,\text{eV}$ for the formation energies, and $\varepsilon^{(h)} = 5.029\,\text{eV}$ and $\varepsilon^{(a)} = 4.064\,\text{eV}$ for the eigenvalues.

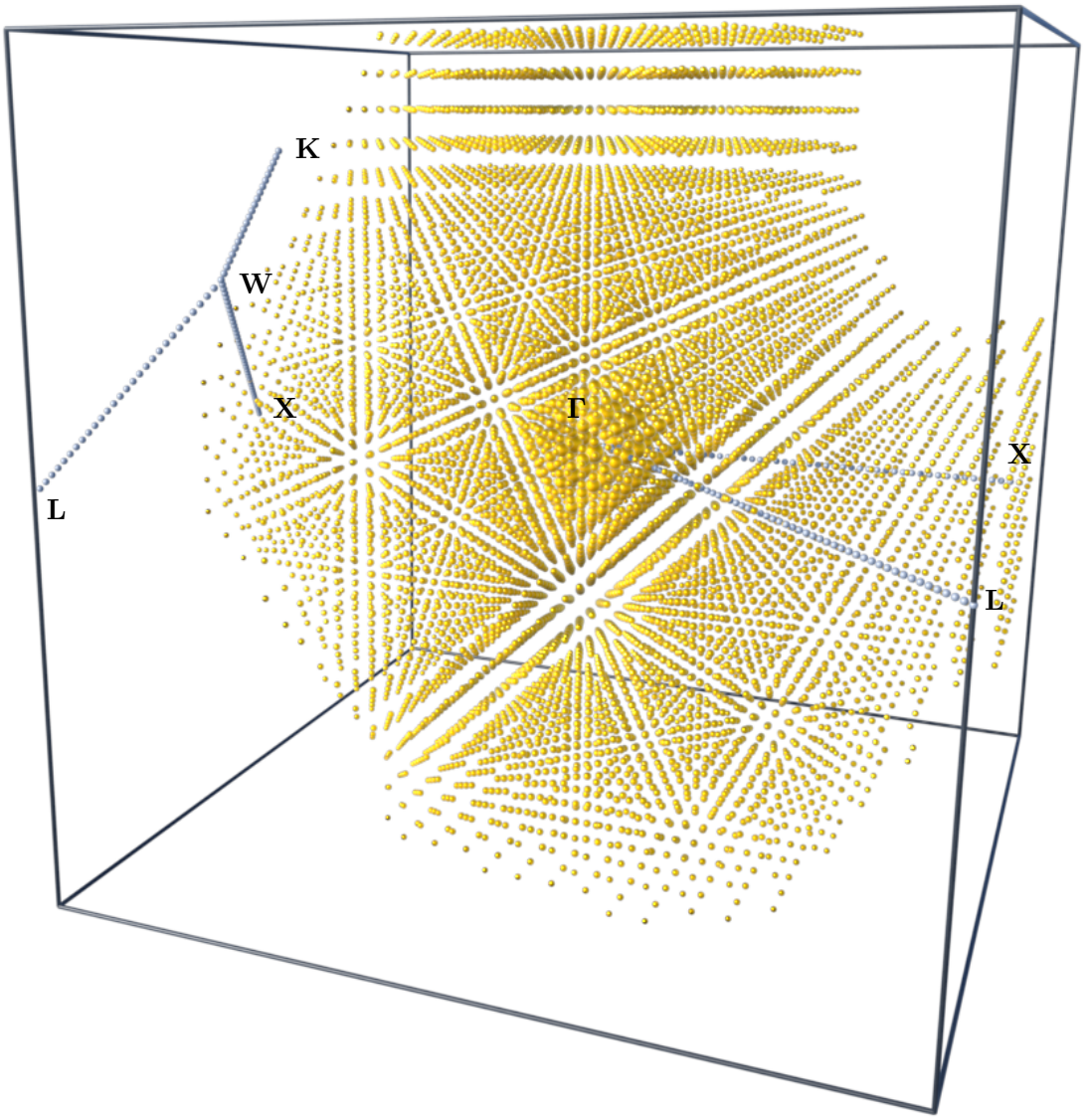

Fig. 9.25.: Phonon energy differences $\Delta E^{\mathrm{LO}}_{\mathbf{q}} = -\left|B^{(a)}_{\mathbf{q}\nu}\right|^2 \frac{\hbar\omega^{(a)}_{\mathbf{q}\nu}}{N_p} + \left|B^{(h)}_{\mathbf{q}\nu}\right|^2 \frac{\hbar\omega^{(h)}_{\mathbf{q}\nu}}{N_p}\Big|_{\nu=\mathrm{LO}}$ with $\left|\Delta E^{\mathrm{LO}}_{\mathbf{q}}\right| \geq 0.0072\,\mathrm{meV}$, for the LO branch on a $24 \times 24 \times 24$ $\mathbf{q}$-grid spanning the 1$^{\mathrm{st}}$ BZ. Golden blobs represent positive, and red blobs represent negative differences. The shown blobs account for more than 90% of the energy differences in the LO branch, depicted by their volumes. The dotted gray path indicates the high-symmetry path connecting the labeled high-symmetry points in the $\mathbf{q}$-mesh.

Chapter 10

Summary and Outlook

This work presented essential theoretical concepts and approximation methods in solid-state physics, along with recently developed methodologies for polaron formation calculations by Sio et al. [9] and for obtaining phonon dispersions incorporating anharmonicity using the SSCHA method [15]. These methodologies were applied to electron and hole polaron formation in LiF, successfully reproducing the results reported in Refs. [9, 10, 40]. Hole polaron calculations were further extended by incorporating anharmonicity in the phonon dispersion to explore its impact on the formation energy.

The anharmonic phonon dispersion used in hole polaron calculations was obtained from a SSCHA minimization, which involved batches of DFT energy minimizations for various supercell configurations, sampling the nuclear density operator in a MC fashion. To ensure computational feasibility, the supercell size for calculating the phonon dispersion was chosen significantly smaller than the corresponding BZ sampling used in the initial polaron calculations. Consequently, establishing a proper baseline for comparison required an additional hole polaron calculation using a harmonic phonon dispersion on the coarser $\mathbf{q}$-grid, which resulted in a lower formation energy compared to the energy calculated on the finer grid and the values reported in Refs. [9, 10, 40]. Including anharmonicity in the phonon dispersion led to a higher formation energy than that of the baseline calculation. A detailed comparison revealed that the most significant energy difference arises from the phonon contribution, particularly within the LO branch. The higher phonon frequencies in the anharmonic dispersion increase the energetic cost of lattice distortion, thereby raising the polaron formation energy and making hole polaron formation less favorable.

Future work could extend the polaron formation calculations to other materials with a rock-salt structure composed of alkali metals and halogens, testing the hypothesis that both electron and hole polarons form in this material class and may exhibit similar properties in terms of ionic displacements and polaron wave functions. The next step in incorporating anharmonic effects into phonon dispersions, and subsequently into polaron formation calculations, would be to further verify the observed differences between

anharmonic and harmonic cases by improving the accuracy of the anharmonic phonon dispersion. This could be achieved through the use of larger supercells in the SSCHA minimization procedure or alternative approaches, such as involving machine learning techniques. Calculations using refined anharmonic phonons could then be compared to the converged hole polaron calculations. A more accurate anharmonic phonon dispersion could also be applied to electron polaron calculations. Finally, the investigation of the influence of anharmonicity in the phonon dispersion on polaron formation can be extended to other materials to test whether the trend of higher formation energies, observed for hole polarons in LiF, holds more generally.

Bibliography

[1] Richard D. Mattuck. *A guide to Feynman diagrams in the many-body problem.* McGraw-Hill, New York, 2nd edition, 1976.

[2] Cesare Franchini, Michele Reticcioli, Martin Setvin, and Ulrike Diebold. Polarons in materials. *Nature reviews. Materials*, 6(7):560–586, 2021.

[3] Lev D. Landau. Über die Bewegung der Elektronen im Kristallgitter. *Phys. Z. Sowjetunion*, 3:644–645, 1933.

[4] Solomon I. Pekar. Local quantum states of electrons in an ideal ion crystal. *Zh. Eksp. Teor. Fiz.*, 16:341–348, 1946.

[5] Herbert Fröhlich, Hans Pelzer, and Sigurd Zienau. Properties of slow electrons in polar materials. *Philos. Mag. J. Sci.*, 41:221–242, 1950.

[6] Herbert Frölich. Electrons in lattice fields. *Adv. Phys.*, 3:325–361, 1954.

[7] Theodore Holstein. Studies of polaron motion: Part I. The molecular-crystal model. *Ann. Phys.*, 8:325–342, 1959.

[8] Theodore Holstein. Studies of polaron motion: Part II. The "small" polaron. *Ann. Phys.*, 8:343–389, 1959.

[9] Weng Hong Sio, Carla Verdi, Samuel Poncé, and Feliciano Giustino. Ab initio theory of polarons: Formalism and applications. *Phys. Rev. B*, 99, Jun 2019.

[10] Weng Hong Sio, Carla Verdi, Samuel Poncé, and Feliciano Giustino. Polarons from first principles, without supercells. *Phys. Rev. Lett.*, 122, Jun 2019.

[11] Jesse Noffsinger, Feliciano Giustino, Brad D. Malone, Cheol-Hwan Park, Steven G. Louie, and Marvin L. Cohen. EPW: A program for calculating the electron–phonon coupling using maximally localized Wannier functions. *Computer Physics Communications*, 181(12):2140–2148, 2010.

[12] Samuel Poncé, Roxana Margine, Carla Verdi, and Feliciano Giustino. EPW: Electron–phonon coupling, transport and superconducting properties using maximally localized Wannier functions. *Computer Physics Communications*, 209:116–133, 2016.

[13] P Giannozzi, O Andreussi, T Brumme, O Bunau, M Buongiorno Nardelli, M Calandra, R Car, C Cavazzoni, D Ceresoli, M Cococcioni, N Colonna, I Carnimeo, A Dal Corso, S de Gironcoli, P Delugas, R A DiStasio Jr, A Ferretti, A Floris, G Fratesi, G Fugallo, R Gebauer, U Gerstmann, F Giustino, T Gorni, J Jia, M Kawamura, H-Y Ko, A Kokalj, E Küçükbenli, M Lazzeri, M Marsili, N Marzari, F Mauri, N L Nguyen, H-V Nguyen, A Otero de-la Roza, L Paulatto, S Poncé, D Rocca, R Sabatini, B Santra, M Schlipf, A P Seitsonen, A Smogunov, I Timrov, T Thonhauser, P Umari, N Vast, X Wu, and S Baroni. Advanced capabilities for materials modelling with QUANTUM ESPRESSO. *Journal of Physics: Condensed Matter*, 29(46):465901, 2017.

[14] Giovanni Pizzi, Valerio Vitale, Ryotaro Arita, Stefan Blügel, Frank Freimuth, Guillaume Géranton, Marco Gibertini, Dominik Gresch, Charles Johnson, Takashi Koretsune, Julen Ibañez-Azpiroz, Hyungjun Lee, Jae-Mo Lihm, Daniel Marchand, Antimo Marrazzo, Yuriy Mokrousov, Jamal I Mustafa, Yoshiro Nohara, Yusuke Nomura, Lorenzo Paulatto, Samuel Poncé, Thomas Ponweiser, Junfeng Qiao, Florian Thöle, Stepan S Tsirkin, Małgorzata Wierzbowska, Nicola Marzari, David Vanderbilt, Ivo Souza, Arash A Mostofi, and Jonathan R Yates. Wannier90 as a community code: new features and applications. *Journal of Physics: Condensed Matter*, 32(16):165902, Jan 2020.

[15] Lorenzo Monacelli, Raffaello Bianco, Marco Cherubini, Matteo Calandra, Ion Errea, and Francesco Mauri. The stochastic self-consistent harmonic approximation: calculating vibrational properties of materials with full quantum and anharmonic effects. *Journal of Physics: Condensed Matter*, 33(36):363001, Jul 2021.

[16] Alexandre S. Alexandrov and Jozef T. Devreese. *Advances in Polaron Physics*. Springer, Berlin, Heidelberg, 2009.

[17] Feliciano Giustino. *Materials modelling using density functional theory : properties and predictions*. Oxford University Press, Oxford, 2014.

[18] Gerd Czycholl. *Theoretische Festkörperphysik Band 1*. Springer, Berlin, Heidelberg, 2015.

[19] Stefano Baroni, Stefano de Gironcoli, Andrea Dal Corso, and Paolo Giannozzi. Phonons and related crystal properties from density-functional perturbation theory. *Reviews of Modern Physics*, 73(2):515–562, July 2001.

[20] Rudolf Gross and Achim Marx. *Festkörperphysik*. De Gruyter Studium. De Gruyter, Berlin, Boston, 3rd edition, 2018.

[21] Felix Bloch. Über die Quantenmechanik der Elektronen in Kristallgittern. *Zeitschrift für Physik*, 52:555–600, Aug 1929.

[22] Nicola Marzari, Arash A. Mostofi, Jonathan R. Yates, Ivo Souza, and David Vanderbilt. Maximally localized Wannier functions: Theory and applications. *Reviews of modern physics*, 84(4):1419–1475, 2012.

[23] Nicola Marzari and David Vanderbilt. Maximally localized generalized Wannier functions for composite energy bands. *Physical review. B, Condensed matter*, 56(20):12847–12865, 1997.

[24] Feliciano Giustino. Electron-phonon interactions from first principles. *Reviews of Modern Physics*, 89(1), February 2017.

[25] Pierre Hohenberg and Walter Kohn. Inhomogeneous electron gas. *Phys. Rev.*, 136:B864–B871, Nov 1964.

[26] Walter Kohn and Lu Jeu Sham. Self-consistent equations including exchange and correlation effects. *Phys. Rev.*, 140:A1133–A1138, Nov 1965.

[27] Paolo Gianozzi. Density-functional perturbation theory, Jun 2022. Presentation at: 2022 School on Electron-Phonon Physics from First Principles, Austin, TX.

[28] Jon Lafuente Bartolome and Chao Lian. Self-trapped polarons with EPW, Jun 2023. Hands-on session (Wed.3) at: 2023 Virtual School on Many-Body Calculations using EPW and BerkeleyGW, Virtual.

[29] Ion Errea. Lecture 2: Non-perturbative anharmonicity and the SSCHA, Jun 2023. Presentation at: SSCHA School 2023, Donostia/San Sebastián, Spain.

[30] James J. Binney, N.J. Dowrick, Andrew J. Fisher, and Mark E.J. Newman. *The theory of critical phenomena : an introduction to the renormalization group*. Oxford science publications. Clarendon Press, Oxford, reprint. edition, 1995.

[31] Lorenzo Monacelli, Ion Errea, Matteo Calandra, and Francesco Mauri. Pressure and stress tensor of complex anharmonic crystals within the stochastic self-consistent harmonic approximation. *Physical Review B 97, 214101*, 2018.

[32] P Giannozzi, O Andreussi, T Brumme, O Bunau, M Buongiorno Nardelli, M Calandra, R Car, C Cavazzoni, D Ceresoli, M Cococcioni, N Colonna, I Carnimeo, A Dal Corso, S de Gironcoli, P Delugas, R A DiStasio Jr, A Ferretti, A Floris, G Fratesi, G Fugallo, R Gebauer, U Gerstmann, F Giustino, T Gorni, J Jia, M Kawamura, H-Y Ko, A Kokalj, E Küçükbenli, M Lazzeri, M Marsili, N Marzari, F Mauri, N L Nguyen, H-V Nguyen, A Otero de-la Roza, L Paulatto, S Poncé, D Rocca, R Sabatini, B Santra, M Schlipf, A P Seitsonen, A Smogunov, I Timrov, T Thonhauser, P Umari, N Vast, X Wu, and S Baroni. Input file description for projwfc.x of QUANTUM ESPRESSO.

[33] Samuel Poncé. Electron-phonon matrix elements and coupling strength, Jun 2023. Hands-on session (Mon.3) at: 2023 Virtual School on Many-Body Calculations using EPW and BerkeleyGW, Virtual.

[34] Carla Verdi, Luigi Ranalli, Cesare Franchini, and Georg Kresse. Quantum paraelectricity and structural phase transitions in strontium titanate beyond density functional theory. *Physical review materials*, 7(3), 2023.

[35] Luigi Ranalli, Carla Verdi, Lorenzo Monacelli, Georg Kresse, Matteo Calandra, and Cesare Franchini. Temperature-dependent anharmonic phonons in quantum paraelectric KTaO3 by first principles and machine-learned force fields. *Advanced quantum technologies (Online)*, 6(4):n/a, 2023.

[36] G. Makov and M. C. Payne. Periodic boundary conditions in ab initio calculations. *Physical review. B, Condensed matter*, 51(7):4014–4022, 1995.

[37] D. R. Hamann. Optimized norm-conserving Vanderbilt pseudopotentials. *Phys. Rev. B*, 88:085117, Aug 2013.

[38] JP Perdew, K Burke, and M Ernzerhof. Generalized gradient approximation made simple (vol 77, pg 3865, 1996). *Physical review letters*, 78(7):1396–1396, 1997.

[39] QuanSheng Wu. How to construct high-quality Wannier functions, Oct 2019.

[40] L. Dressler, U. Griebner, and R. Kittner. Precision measurement of lattice parameters in LiF monocrystals. *Crystal research and technology (1979)*, 22(11):1431–1435, 1987.

[41] Fabien Tran and Peter Blaha. Accurate band gaps of semiconductors and insulators with a semilocal exchange-correlation potential. *Physical review letters*, 102(22):226401–226401, 2009.

[42] G. Dolling, H. G. Smith, R. M. Nicklow, P. R. Vijayaraghavan, and M. K. Wilkinson. Lattice dynamics of lithium fluoride. *Physical review*, 168(3):970–979, 1968.

[43] Tristan L. Britt, Fabio Caruso, and Bradley J. Siwick. A momentum-resolved view of polaron formation in materials. *npj computational materials*, 10(1):178–9, 2024.

Acronyms

ARPES Angle-Resolved Photoemission Spectroscopy. 1, 95

BO Born-Oppenheimer. 3, 11, 19, 22, 23, 30, 32, 35, 37, 43, 45, 61, 62, 95

BZ Brillouin Zone. 15, 18, 22, 34, 49–51, 58, 66, 73, 81, 83, 88, 89, 95, 110–112

DFPT Density Functional Perturbation Theory. 3, 32, 34, 41, 46, 51, 52, 54, 58, 61–65, 70, 77, 81, 85, 86, 95, 99, 100, 106, 109

DFT Density Functional Theory. 2, 3, 27–29, 35, 38, 41, 46, 50, 51, 54, 57, 58, 61–64, 66, 70, 73, 74, 77, 89, 95, 105, 107

DOS Density Of States. 16, 51, 95

EPW Electron-Phonon Wannier. 2, 57, 59, 60, 95

FCC Face-Centered Cubic. 57, 67, 74, 95

FFT Fast Fourier Transform. 52, 95

GGA Generalized Gradient Approximation. 95

LA Longitudinal Acoustic. 83, 95, 111

LDA Local Density Approximation. 28, 95

LO Longitudinal Optical. 2, 34, 75, 83, 84, 88, 89, 95

LP model Landau-Pekar Model. 1–3, 5–8, 38, 39, 95

MC Monte Carlo. 46, 89, 95

MLWF Maximally Localized Wannier Functions. 19, 52–54, 59, 60, 64, 67, 73, 74, 81, 95, 101–104

Acronyms

OPW Orthogonalized Plane Wave. 50, 95

PBE Perdew-Burke-Ernzerhof. 57, 95

PDOS Projected Density Of States. 51, 58–60, 64, 66, 73, 95

QE Quantum ESPRESSO. 2, 57, 95

SSCHA Self-Consistent Harmonic Approximation. 2–4, 43–46, 54, 57, 61–63, 81–83, 85, 86, 89, 95, 100, 104, 107–109

STM Scanning Tunneling Microscopy. 1, 95

STS Scanning Tunneling Spectroscopy. 1, 95

TA Transverse Acoustic. 65, 83, 95, 112

TO Transverse Optical. 65, 83, 95, 110

UEDS Ultrafast Electron Diffuse Scattering. 95

Appendix A

Supplementary Figures

A.1. Phonon Dispersions after Fourier Interpolation

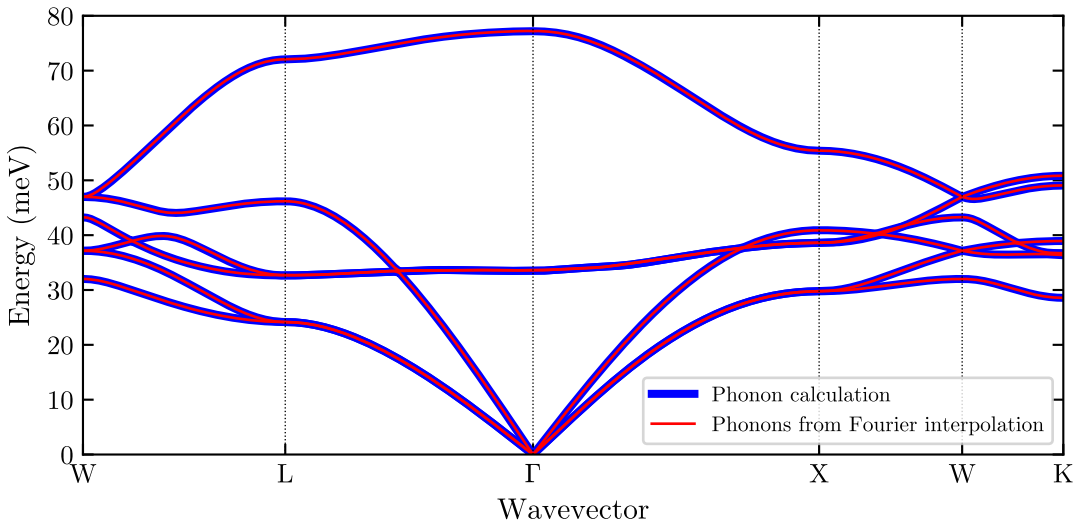

Fig. A.1.: Phonon dispersion after Fourier interpolation, shown in red, overlaid on the initial dispersion in blue, which was obtained from a DFPT calculation on a $12 \times 12 \times 12$ **q**-grid.

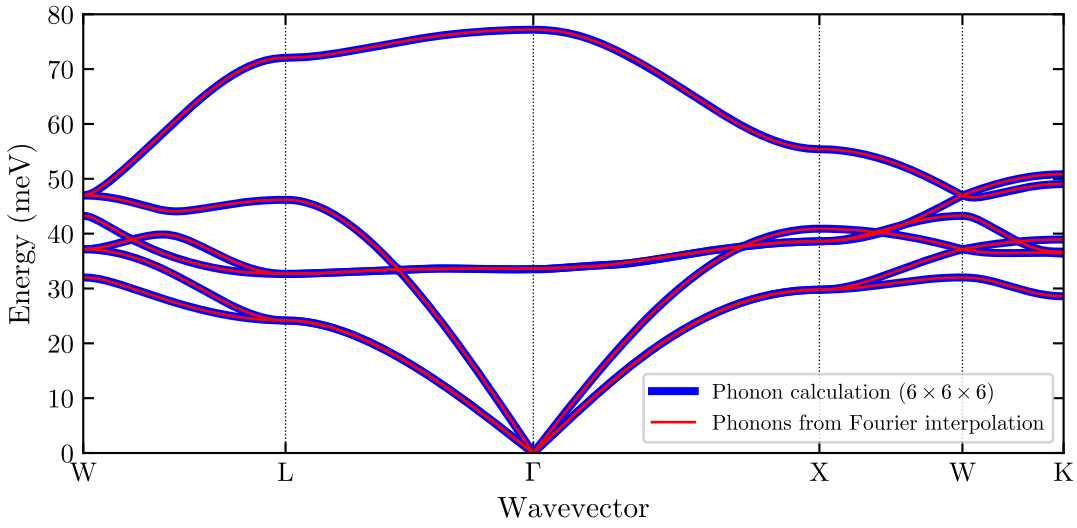

Fig. A.2.: Phonon dispersion after Fourier interpolation, shown in red, overlaid on the initial dispersion in blue, which was obtained from a DFPT calculation on a $6 \times 6 \times 6$ **q**-grid.

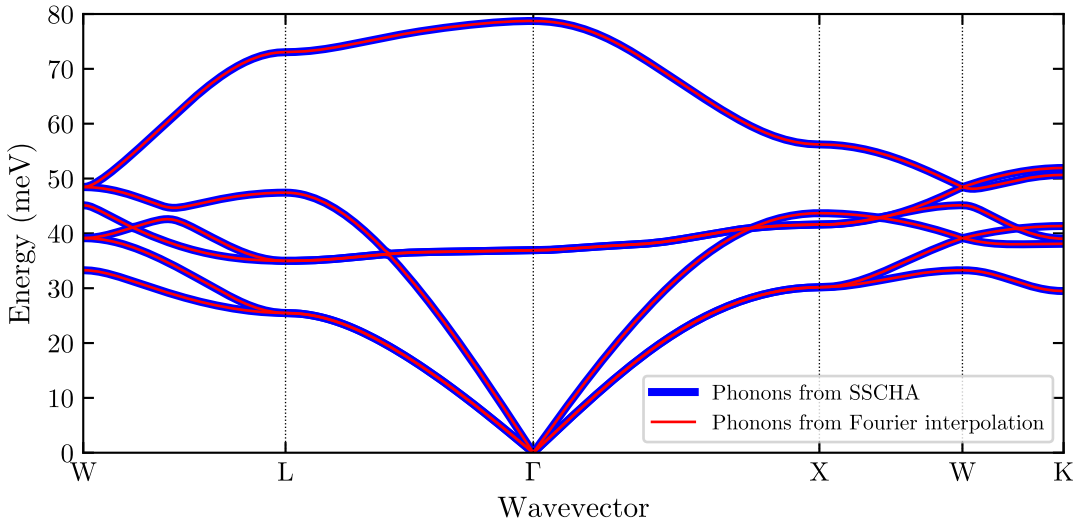

Fig. A.3.: Phonon dispersion after Fourier interpolation, shown in red, overlaid on the initial dispersion in blue, which was calculated from a SSCHA minimization in a $6 \times 6 \times 6$ supercell.

A.2. Decay of Matrix Elements in Wannier Representation

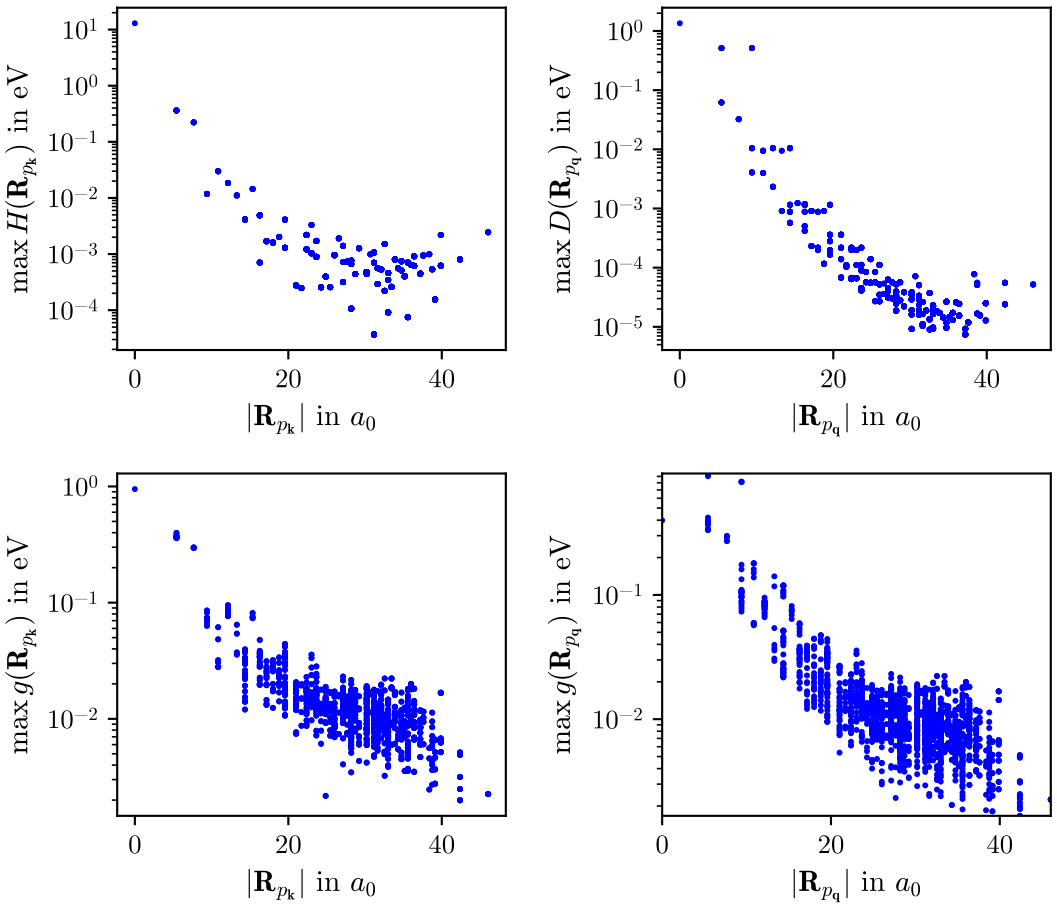

Fig. A.4.: Decay of the maximal matrix elements of $H_{nm}(\mathbf{R}_{p_\mathbf{k}})$, $D_{\kappa\alpha,\kappa'\alpha'}(\mathbf{R}_{p_\mathbf{q}})$, $g_{mn\kappa\alpha}(\mathbf{R}_{p_\mathbf{k}}, 0)$, and $g_{mn\kappa\alpha}(0, \mathbf{R}_{p_\mathbf{q}})$, within the $12 \times 12 \times 12$ supercell, shown in the top left, top right, bottom left, and bottom right panels, respectively. These quantities were used in electron polaron calculations and were therefore obtained using the conduction band's MLWF.

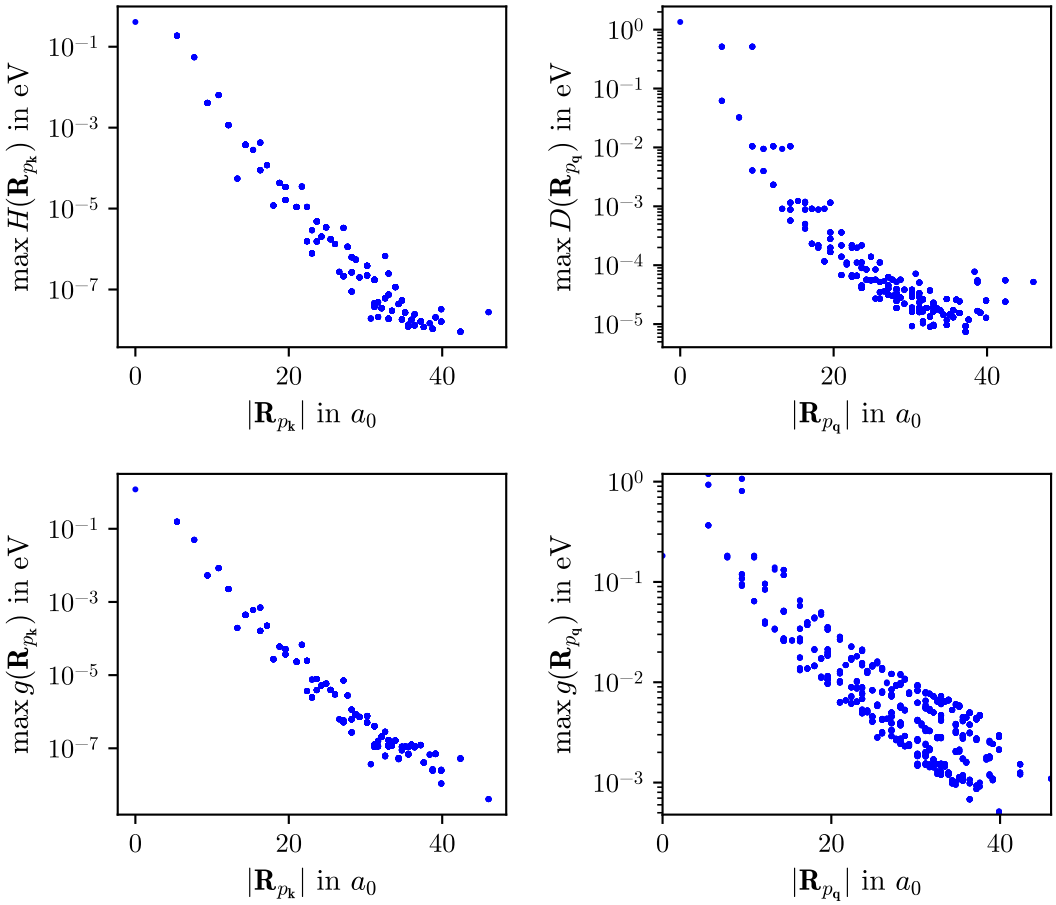

Fig. A.5.: Decay of the maximal matrix elements of $H_{nm}(\mathbf{R}_{p_\mathbf{k}})$, $D_{\kappa\alpha,\kappa'\alpha'}(\mathbf{R}_{p_\mathbf{q}})$, $g_{mn\kappa\alpha}(\mathbf{R}_{p_\mathbf{k}}, 0)$, and $g_{mn\kappa\alpha}(0, \mathbf{R}_{p_\mathbf{q}})$, within the $12 \times 12 \times 12$ supercell, shown in the top left, top right, bottom left, and bottom right panels, respectively. These quantities were used in hole polaron calculations and were therefore obtained using the top three valence bands' MLWFs.

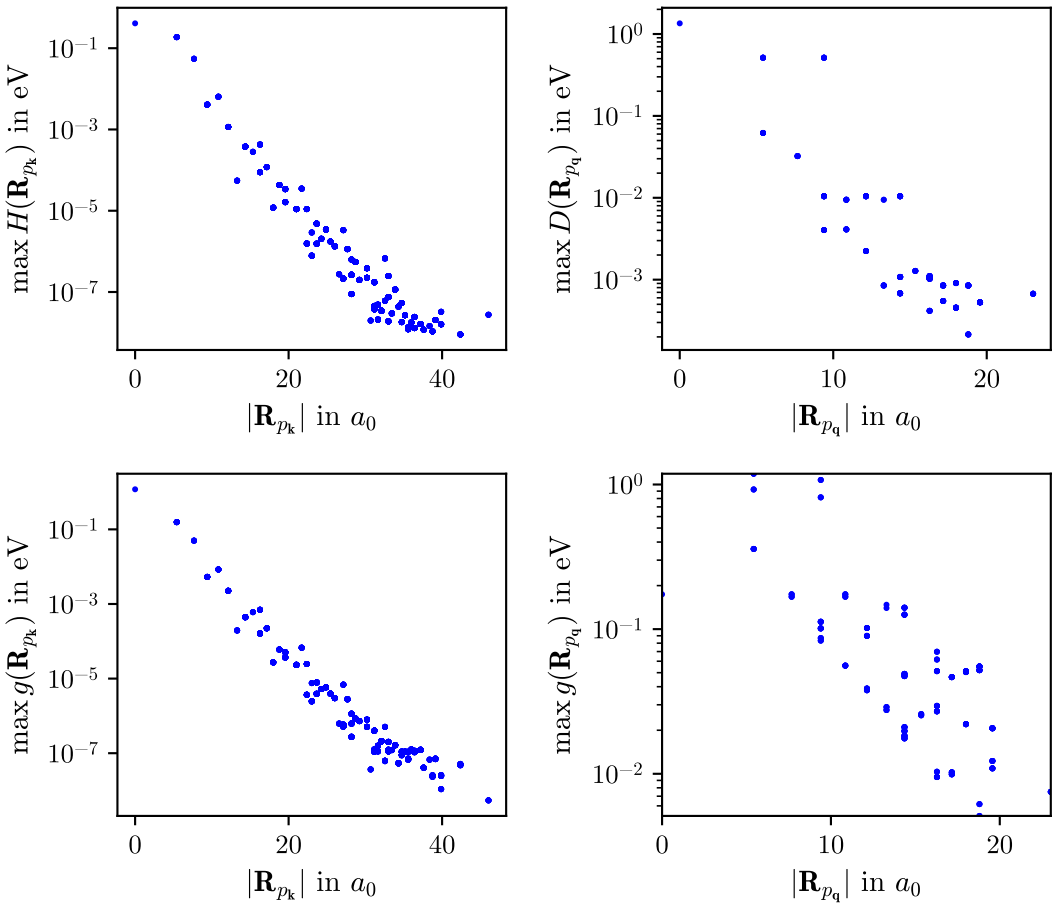

Fig. A.6.: Decay of the maximal matrix elements of $H_{nm}(\mathbf{R}_{p_\mathbf{k}})$, $D_{\kappa\alpha,\kappa'\alpha'}(\mathbf{R}_{p_\mathbf{q}})$, $g_{mn\kappa\alpha}(\mathbf{R}_{p_\mathbf{k}}, 0)$, and $g_{mn\kappa\alpha}(0, \mathbf{R}_{p_\mathbf{q}})$, shown in the top left, top right, bottom left, and bottom right panels, respectively. Depending on the parameterization—either $\mathbf{R}_{p_\mathbf{k}}$ or $\mathbf{R}_{p_\mathbf{q}}$—the decay is shown within the $12 \times 12 \times 12$ or $6 \times 6 \times 6$ supercell, respectively. The quantities mentioned were used in hole polaron calculations and were therefore obtained using the top three valence bands' MLWFs.

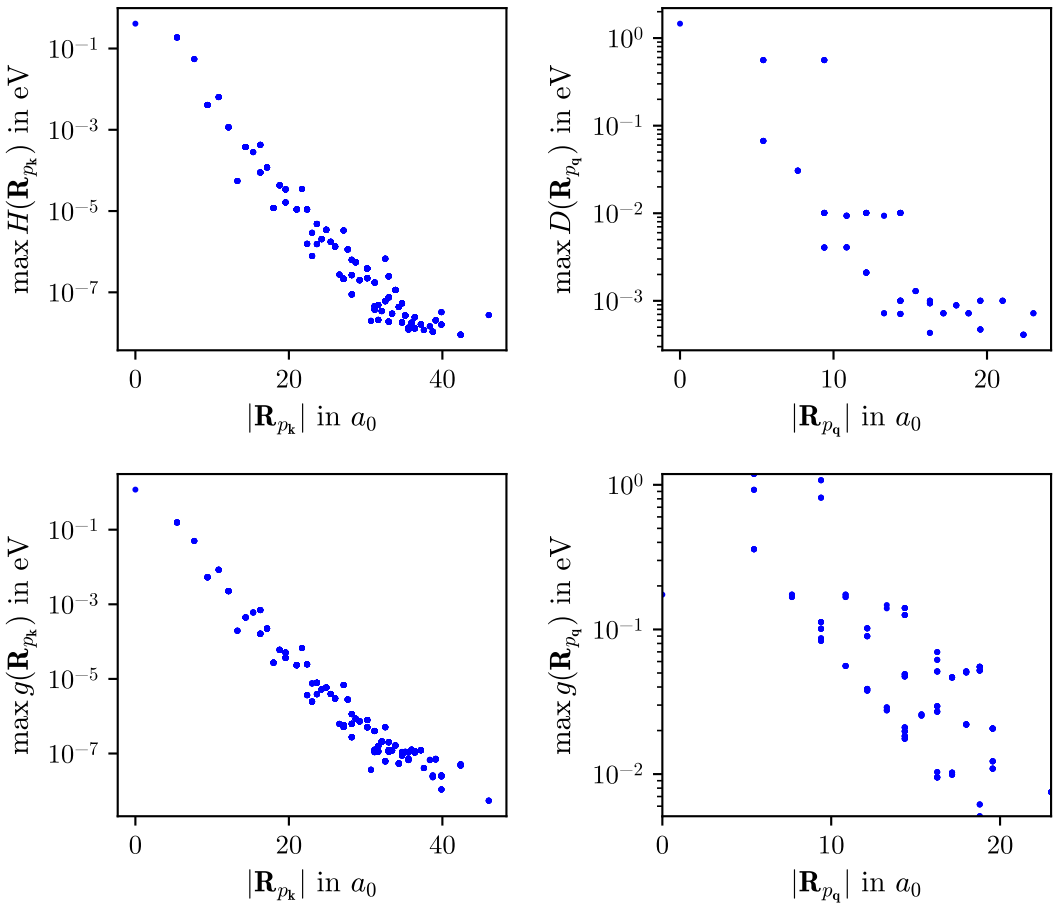

Fig. A.7.: Decay of the maximal matrix elements of $H_{nm}(\mathbf{R}_{p_\mathbf{k}})$, $D_{\kappa\alpha,\kappa'\alpha'}(\mathbf{R}_{p_\mathbf{q}})$, $g_{mn\kappa\alpha}(\mathbf{R}_{p_\mathbf{k}}, 0)$, and $g_{mn\kappa\alpha}(0, \mathbf{R}_{p_\mathbf{q}})$, shown in the top left, top right, bottom left, and bottom right panels, respectively. Depending on the parameterization—either $\mathbf{R}_{p_\mathbf{k}}$ or $\mathbf{R}_{p_\mathbf{q}}$—the decay is shown within the $12 \times 12 \times 12$ or $6 \times 6 \times 6$ supercell, respectively. The quantities mentioned were used in hole polaron calculations incorporating anharmonic phonons and were therefore calculated using phonons from SSCHA minimization along with the top three valence bands' MLWFs.

Appendix B

Harmonic vs. Anharmonic Phonons

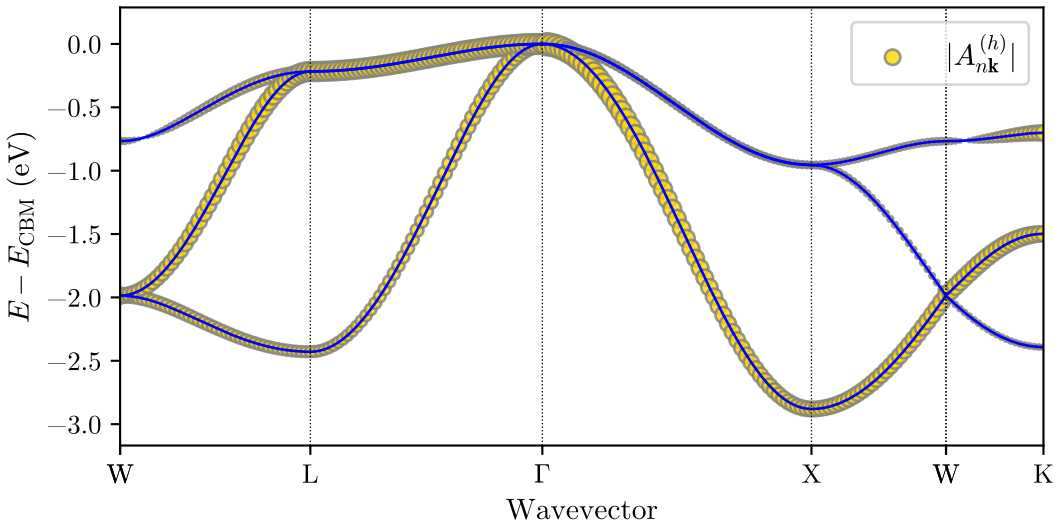

Fig. B.1.: Visualization of coefficients $A^{(h)}_{n\mathbf{k}}$ from a polaron calculation in a $24 \times 24 \times 24$ supercell, based on harmonic phonons calculated on a $6 \times 6 \times 6$ $\mathbf{q}$-grid. The magnitudes of the coefficients are represented by the radii of the yellow discs, overlaid on the DFT band structure of the top three valence bands of LiF. They illustrate the contributions of valence-band Kohn-Sham orbitals to the polaron wave function.

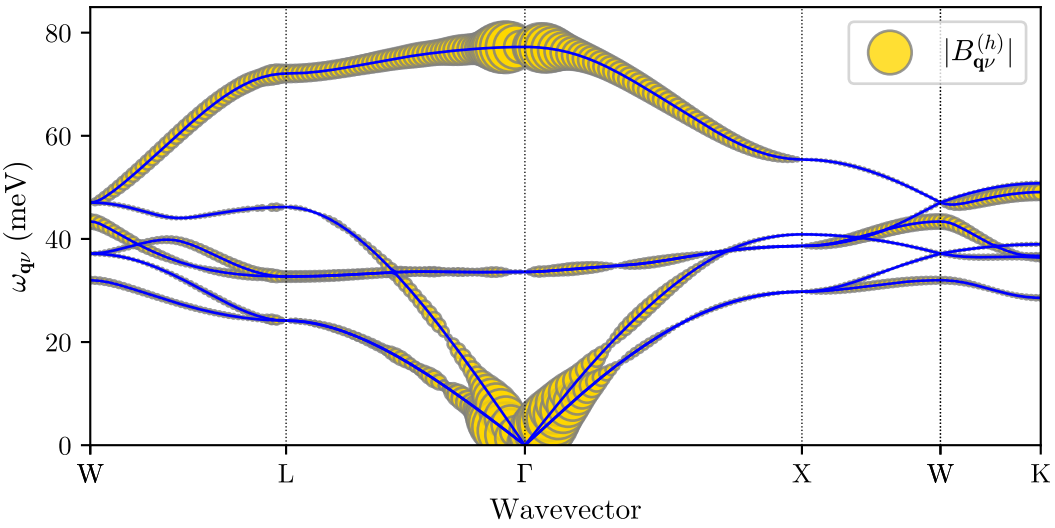

Fig. B.2.: Visualization of coefficients $B^{(h)}_{\mathbf{q}\nu}$ from a hole polaron calculation in a $24\times24\times24$ supercell, based on harmonic phonons calculated on a $6\times6\times6$ $\mathbf{q}$-grid. The magnitudes of the coefficients are represented by the radii of the yellow discs, overlaid on the DFPT phonon dispersion. They illustrate the contributions of phonons to the lattice displacements associated with the polaron.

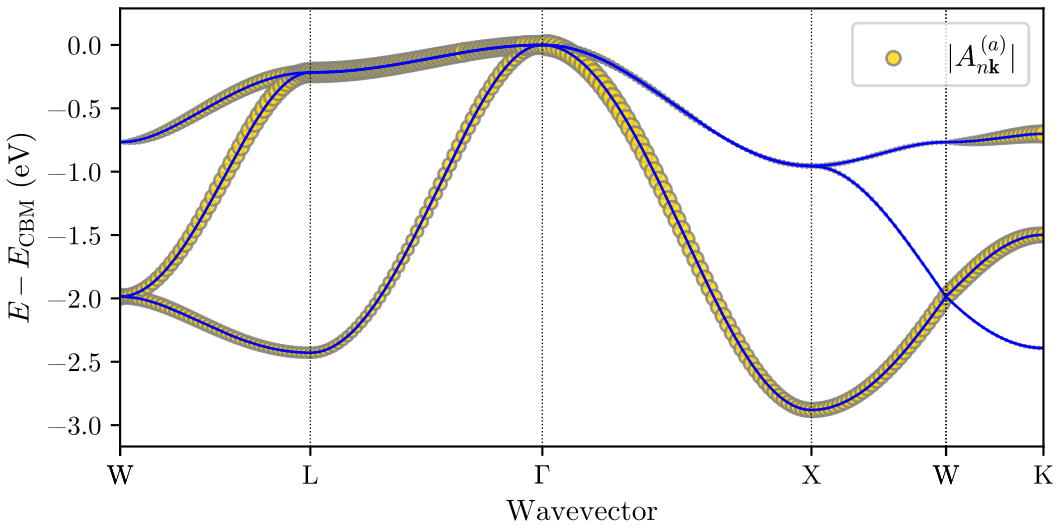

Fig. B.3.: Visualization of coefficients $A^{(a)}_{n\mathbf{k}}$ from a hole polaron calculation in a $24 \times 24 \times 24$ supercell, based on anharmonic phonons obtained from SSCHA minimization in a $6 \times 6 \times 6$ supercell. The magnitudes of the coefficients are represented by the radii of the yellow discs, overlaid on the DFT band structure of the top three valence bands of LiF. They illustrate the contributions of valence-band Kohn-Sham orbitals to the polaron wave function.

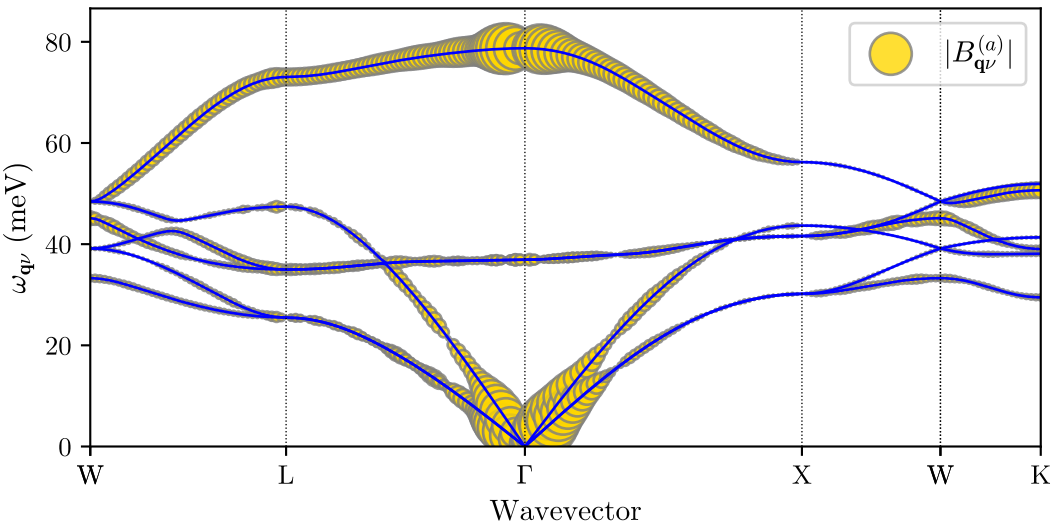

Fig. B.4.: Visualization of coefficients $B^{(a)}_{\mathbf{q}\nu}$ from a hole polaron calculation in a $24 \times 24 \times 24$ supercell, based on anharmonic phonons obtained from SSCHA minimization in a $6 \times 6 \times 6$ supercell. The magnitudes of the coefficients are represented by the radii of the yellow discs, overlaid on the phonon dispersion obtained from SSCHA minimization. They illustrate the contributions of phonon modes to the lattice displacements associated with the polaron.

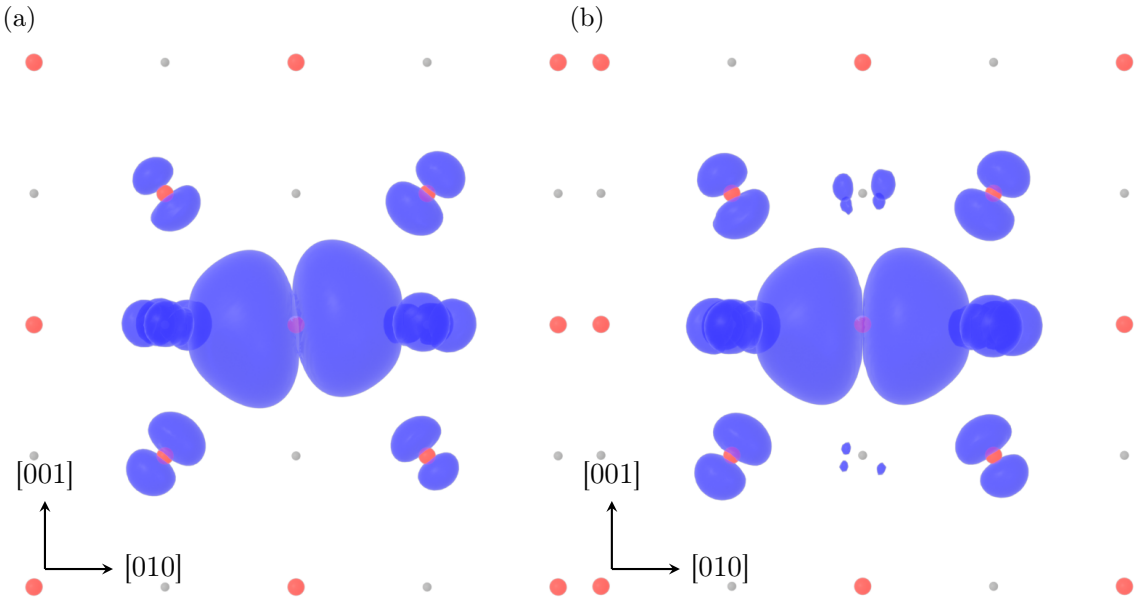

Fig. B.5.: Isosurface plots of hole polaron wave functions along [100]. The wave functions are taken from polaron calculations in a $24 \times 24 \times 24$ supercell using phonons from (a) a DFPT phonon calculation on a $6 \times 6 \times 6$ $\mathbf{q}$-grid, and (b) a SSCHA minimization in a $6 \times 6 \times 6$ supercell. The red and gray beads represent F and Li ions, respectively, illustrating a layer of LiF intersecting the polaron center.

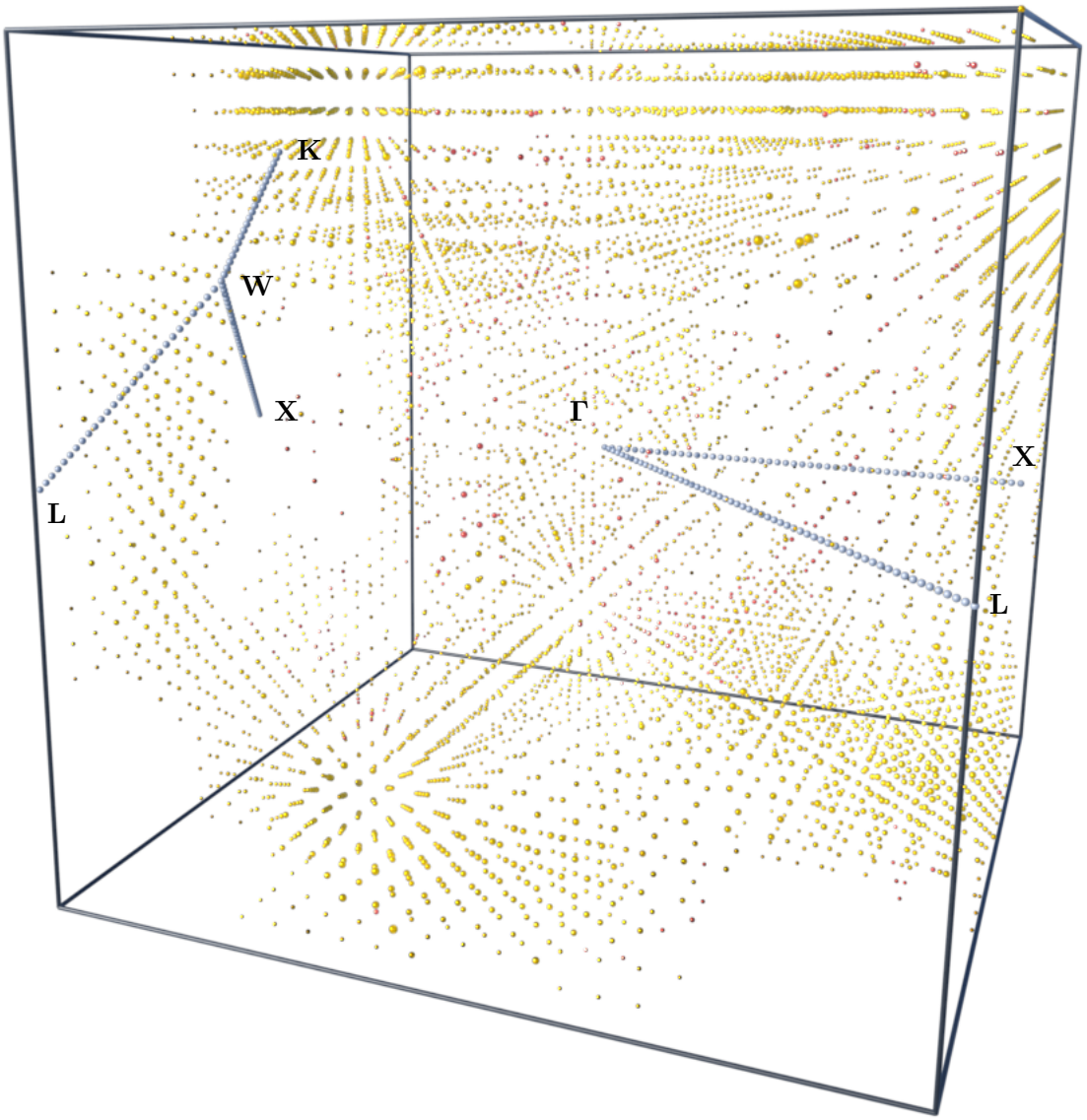

Fig. B.6.: Phonon energy differences $\Delta E^{\mathrm{TO}}_{\mathbf{q}} = \sum_{\nu\in\{\mathrm{TO}_1,\,\mathrm{TO}_2\}} -\left|B^{(a)}_{\mathbf{q}\nu}\right|^2 \frac{\hbar\omega^{(a)}_{\mathbf{q}\nu}}{N_p} + \left|B^{(h)}_{\mathbf{q}\nu}\right|^2 \frac{\hbar\omega^{(h)}_{\mathbf{q}\nu}}{N_p}$ with $\left|\Delta E^{\mathrm{TO}}_{\mathbf{q}}\right| \geq 0.0014\,\mathrm{meV}$, summed over the TO_1 and TO_2 branches on a $24 \times 24 \times 24$ $\mathbf{q}$-grid spanning the 1$^{\mathrm{st}}$ BZ. Golden blobs represent positive, and red blobs represent negative differences. The shown blobs account for more than 85% of the energy differences in the TO branches, depicted by their volumes. The dotted gray path indicates the high-symmetry path connecting the labeled high-symmetry points in the $\mathbf{q}$-mesh.

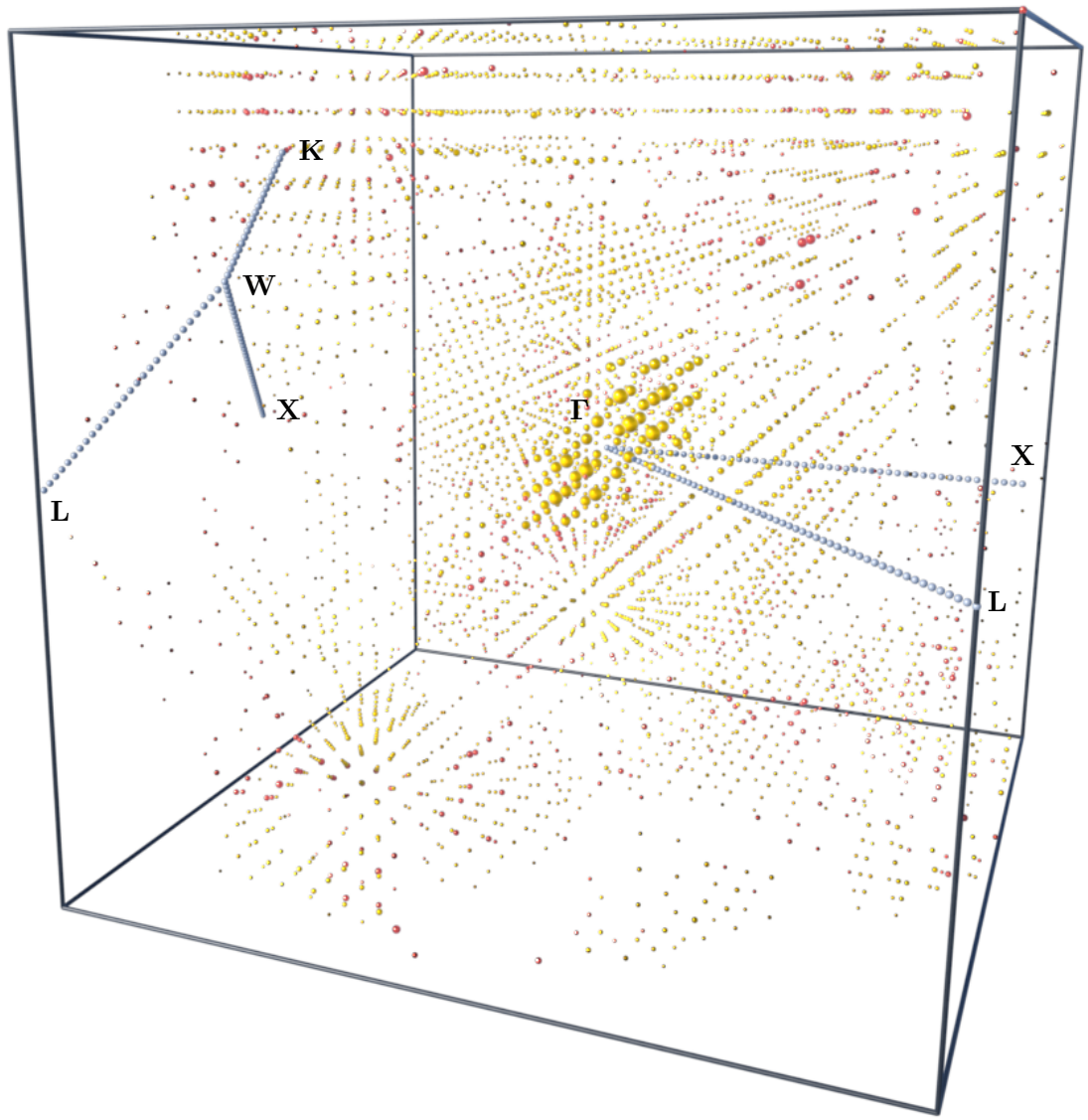

Fig. B.7.: Phonon energy differences $\Delta E^{\mathrm{LA}}_{\mathbf{q}} = -\left|B^{(a)}_{\mathbf{q}\nu}\right|^2 \frac{\hbar\omega^{(a)}_{\mathbf{q}\nu}}{N_p} + \left|B^{(h)}_{\mathbf{q}\nu}\right|^2 \frac{\hbar\omega^{(h)}_{\mathbf{q}\nu}}{N_p}\Big|_{\nu=\mathrm{LA}}$ with $\left|\Delta E^{\mathrm{LA}}_{\mathbf{q}}\right| \geq 0.0011\,\mathrm{meV}$, for the LA branch on a $24 \times 24 \times 24$ $\mathbf{q}$-grid spanning the 1$^{\mathrm{st}}$ BZ. Golden blobs represent positive, and red blobs represent negative differences. The shown blobs account for more than 89% of the energy differences in the LA branch, depicted by their volumes. The dotted gray path indicates the high-symmetry path connecting the labeled high-symmetry points in the $\mathbf{q}$-mesh.

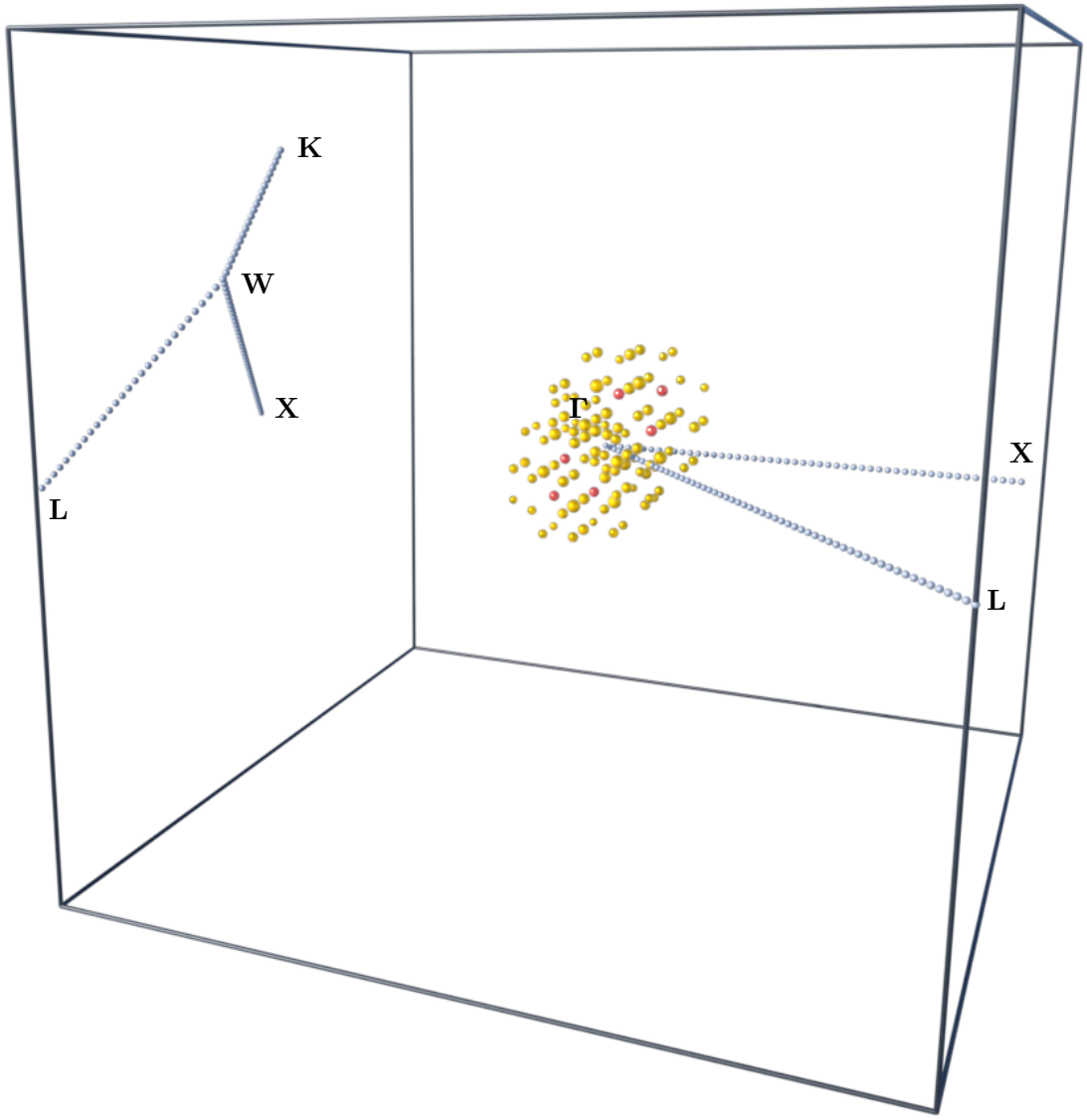

Fig. B.8.: Phonon energy differences $\Delta E^{\mathrm{TA}}_{\mathbf{q}} = \sum_{\nu\in\{\mathrm{TA}_1,\,\mathrm{TA}_2\}} -\left|B^{(a)}_{\mathbf{q}\nu}\right|^2 \frac{\hbar\omega^{(a)}_{\mathbf{q}\nu}}{N_p} + \left|B^{(h)}_{\mathbf{q}\nu}\right|^2 \frac{\hbar\omega^{(h)}_{\mathbf{q}\nu}}{N_p}$ with $\left|\Delta E^{\mathrm{TA}}_{\mathbf{q}}\right| \geq 0.029\,\mathrm{meV}$, summed over the TA_1 and TA_2 branches on a $24 \times 24 \times 24$ $\mathbf{q}$-grid spanning the 1st BZ. Golden blobs represent positive, and red blobs represent negative differences. The shown blobs account for more than 99% of the energy differences in the TA branches, depicted by their volumes. The dotted gray path indicates the high-symmetry path connecting the labeled high-symmetry points in the $\mathbf{q}$-mesh.